FLEXIBLE MICROFLUIDIC SYSTEMS FOR CELLULAR ANALYSIS USING LOW COST FABRICATION TECHNOLOGIES

A Thesis
Presented to
The Academic Faculty

by

Eileen Devra Moss

In Partial Fulfillment
of the Requirements for the Degree
Doctor of Philosophy

School of Electrical and Computer Engineering
Georgia Institute of Technology
August 2006

FLEXIBLE MICROFLUIDIC SYSTEMS FOR CELLULAR ANALYSIS USING LOW COST FABRICATION TECHNOLOGIES

Approved by:

Dr. A. Bruno Frazier, Advisor
School of Electrical and Computer Engineering
Georgia Institute of Technology

Dr. Mark G. Allen
School of Electrical and Computer Engineering
Georgia Institute of Technology

Dr. Oliver Brand
School of Electrical and Computer Engineering
Georgia Institute of Technology

Dr. Georgia Chen
Winship Cancer Institute
Emory University

Dr. Arthur Koblasz
School of Electrical and Computer Engineering
Georgia Institute of Technology

Date Approved: June 23, 2006

To my family,

whose love and support made this possible.

ACKNOWLEDGEMENTS

Graduate school has presented me with numerous opportunities and obstacles, and I could not have succeeded without a tremendous amount of support. First, I would like to thank my advisor, Dr. Bruno Frazier, for his guidance and support over the past five years. I also need to recognize the members of the Microinstrumentation Research Lab, past and present. They have helped me in so many ways, and I will always be grateful. I am also thankful to the Microsensor and Microactuator group here at Georgia Tech, especially Richard Shafer, and to the staff of the Microelectronics Research Center.

I have received a great amount of technical and financial support as well. Thank you to Dr. Georgia Chen from Emory University for her help with the biological side of my project and to DuPont for their generous samples of Kapton®. I would also like to acknowledge the National Science Foundation for their support of my research through an NSF fellowship and Georgia Tech and Steve Chaddick for additional financial support.

Most importantly, I am eternally grateful for the love and support of my friends and family. I am lucky to have been able to form such great friendships from Dayton to Cincinnati to here in Atlanta, and I thank them for being there for me throughout this experience. There is little I can say to express how fortunate I feel about my family. They are the biggest and best support group and cheering section I can imagine. This would have been impossible without them - thank you.

TABLE OF CONTENTS

LIST OF TABLES

LIST OF FIGURES

SUMMARY

This dissertation presents the design, fabrication, and testing of a microfluidic system to be used for whole-cell analysis. The study of cellular function and structure is essential for disease diagnosis and treatment. Microsystems developed to perform these bioanalyses add benefits such as requiring smaller samples and reagents, testing multiple samples in parallel, and supporting point-of-care testing, all of which increases throughput and reduces cost-per-analysis. Traditional methods for designing a microsystem use standard materials and techniques such as silicon, glass, photolithography, and wet and dry etching. This research is focused on utilizing materials and techniques that require less infrastructure, allow for a faster design-to-prototype cycle, and can integrate electrical and fluidic functionality to address a variety of possible applications.

The microfluidic system presented here is comprised of multiple layers of Kapton®, a polyimide available from DuPont. Kapton® provides a biocompatible substrate that is flexible while maintaining structural stability and can be used in high temperature and other harsh environments. Microchannels with widths of 400 μm and thru-hole fluidic vias less than 5 μm in diameter are laser ablated through the flexible polyimide sheets using excimer and CO_2 lasers. Electrical traces and contact pads are defined on the substrate by vapor deposition through reusable microstencils rather than with photolithography. The patterned layers are bonded using heat staking and then packaged with the addition of wires and a fluidic interface.

The structural stability of the developed microfluidic system was tested to determine if the layers of Kapton® would delaminate during normal operation. The results from this analysis showed that the bond between the Kapton® layers is sufficient. The microfluidic system was used to collect impedance spectroscopy data over a frequency range of 40 Hz to 10 MHz on dissociated cells and tissue samples. Analysis of the data showed different

impedance signatures between the various analytes, which demonstrates the ability of the system to use impedance spectroscopy as a means for characterization and differentiation. The microfluidic system was also tested to verify if it could be used for patch-clamping, which is a specific type of whole-cell analysis. The analysis requires the ability to control the position of a single cell and subsequent measurement of small amounts of current. While the results showed that the microsystem can be used to control the movement and placement of a single cell, other attributes of the device itself limit its ability to measure the necessary electrical signals. As a whole, this research demonstrates the realization of a microfluidic system for whole-cell analysis based on non-standard fabrication materials and techniques.

CHAPTER I

INTRODUCTION: MOTIVATION AND OBJECTIVE

whole-cell analysis is fundamental to the diagnosis of diseases, the development of treatments, and the monitoring of a patient's response to therapy. However, these analytical protocols can be highly labor intensive, time-consuming, and expensive. Consequently, there exists a need for performing high-throughput cell analysis in a faster and more cost efficient manner. One possible approach to meeting this need is to use microelectromechanical systems (MEMS), also known as microsystems. Microsystems require smaller biological samples and reagents than traditional techniques, can be used to test multiple samples in parallel, and easily support point-of-care testing, all of which contribute to ease of use and reduced cost per analysis. While microsystems are currently being developed at multiple research facilities for the purpose of cell analysis, their designs are based on standard MEMS fabrication materials and techniques. The objective of the project described herein is to design, fabricate, and test a flexible, multi-layer microfluidic system using non-standard materials and techniques with the goal of demonstrating a less expensive - to both build and use - cell analysis system. Two types of whole-cell analysis, impedance spectroscopy and patch-clamping, where chosen as the applications with which to test the viability of the developed microsystem.

The microfluidic system developed in this thesis is constructed with a polyimide material (Kapton® film made by DuPont) and physical vapor deposited thin-film metal traces for electrical functionality. By combining the techniques of laser ablation, microstenciling, and heat staking to fabricate the microsystem, multiple features are incorporated into a single device. These features include microchannels, thru and embedded fluidic vias, and metallic electrodes and contact pads.

The first chapter of this thesis provides background on the analysis of whole cells in general and then more specifically for impedance spectroscopy and patch-clamping analyses.

Information on microsystems used for biomedical applications is also given. Chapter Two explains the layout, theoretical operation, and fabrication steps for the microfluidic system as well as the mechanical and electrical models of the system. Details of the fabrication procedure and experimental methods for structural testing and cellular analysis are given in Chapters Three and Four. Chapter Five contains the results and discussions from the fabrication, structural testing, and cellular analyses. Chapter Six summarizes the conclusions and provides an outlook towards possible future work stemming from this research.

1.1 General Whole-cell Analysis

Understanding how cells function and characterizing them are important for disease diagnosis and drug discovery [3, 4, 114]. Common techniques employed today for performing whole-cell analysis utilize optical methods, which include various types of microscopy and flow cytometry, some of which have been around for over a century. Microscopy entails viewing a culture of cells under a microscope to observe their shape when adhered to a substrate or while in suspension. A more involved technique involves staining the biological sample with a dye that will be taken up by specific molecules, which aids in differentiating parts of a cell from one another when viewed using light microscopy [24, 92]. For example, different dyes are known to stain only the nucleus of a cell or just the cell cytoplasm [24]. Phase contrast microscopy allows for imaging of live cells and tissues without staining [92]. Fluorescence microscopy has become one of the most popular methods for analyzing cells and tissues. Among the many reasons for this are that fluorescence provides a high degree of sensitivity and specificity [64, 115]. By selecting an appropriate fluorescent dye or probe, a small amount of the molecule of interest will be highly distinguishable from other molecules in its environment. Flow cytometry is a technique that measures various qualities of individual cells in suspension as they flow past optical detectors. Current technology enables the analysis of over 100,000 cells per second [37]. The cells can be tagged with fluorescence probes to increase the type of information gathered during this process. This technique can also be combined with additional equipment such that cell sorting can be performed based on the optical information previously obtained [37].

Although optical methods of analysis are well established and commonly used, the electrophysiology of cells and tissue samples can also be exploited for whole-cell analysis. As shown in Figure 1, the interior of an animal cell contains components such as the nucleus, the mitochondria, and the rough and smooth endoplasmic reticulum, which are all suspended in the cell cytoplasm. All of these components are contained within the cell membrane, which provides structure, protects the cell, and controls the flow of ions into and out of the cell through ion channels. Figure 2 is a drawing of the cross-section of the cell membrane. The membrane is comprised of a lipid bi-layer, i. e. a double layer of phospholipids. The phospholipids have hydrophilic heads that line up along the intracellular and extracellular sides of the membrane while the hydrophobic tails come together at the center of the membrane. Ion channels, located throughout the cell membrane, are made of protein macromolecules and are selective towards specific ions. As part of normal cell growth and function, ions, such as sodium (Na), potassium (K), and calcium (Ca), are constantly transported through these channels. Based on cell signaling mechanisms including electrical and concentration gradients due to the ions on either side of the cell membrane, the channels will open or close allowing certain ions to flow into and out of the cell [4, 114].

Figure 1: The contents of an animal cell include the nucleus, mitochondria, and rough and smooth endoplasmic reticulum all suspended in the cell cytoplasm [68]. The cell membrane provides structure and protection for the cell as well as control over the flow of ions into and out of the cell through ion channels.

The cell membrane together with the flow of ions allows the cell to be analyzed as an electrical circuit, which consists of a membrane capacitance and resistance, intracellular

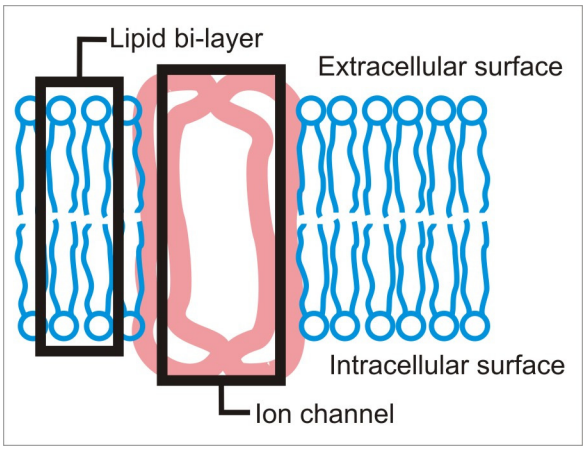

Figure 2: The cell membrane is comprised of a double layer of phospholipids. Ion channels, which control the flow of ions into and out of the cell, are located throughout the cell membrane.

resistance, and a current due to the flow of charged particles. Since the cell membrane consists of a lipid bi-layer with a gap between the layers, it has an associated capacitance, C_m (Equation 1).

$$C_m = \frac{\epsilon_r \epsilon_o}{d} \tag{1}$$

The variable ϵ_r is the relative dielectric constant of the material between the two walls of the capacitor and has no units. For the cell membrane, ϵ_r is usually assigned a value similar to that of oil, approximately 3. The typical distance between the hydrophobic tails, d, is 30 $\dot{A}$, and the permittivity of free space, ϵ_o, is $\frac{10^{-9}}{36\pi}$ $\frac{F}{m}$. This results in an average membrane capacitance, C_m, of 0.9 $\frac{\mu F}{cm^2}$ [114]. The membrane resistance, R_m, is typically listed as 10^9 Ωcm^2. However, when considering the ion channels in the membrane, R_m drops to approximately 10^3 Ωcm^2 [114]. The intracellular resistance, or that due to the cytoplasm, R_c, is listed as approximately 100 Ωcm in the literature [32, 148].

The properties of the cell membrane change based on whether the cell is alive or dead or if the cell is not functioning properly [4, 50]. Normally, the cell membrane has a high resistance and only allows particles to pass into and out of the cell at certain locations based on specific cell signaling. When a cell has died, the membrane breaks down, and molecules flow freely into and out of the cell. In addition, if a cell is diseased, some ions and molecules may be more or less likely to flow into and out of the cell. By monitoring the overall

impedance of the cell or the flow of ions, different types of analyses can be performed. In impedance spectroscopy analysis, measuring the impedance of a whole-cell, a collection of cells, or a section of tissue is used to characterize and identify healthy, diseased, chemically altered, or dead cells or tissues [121, 144, 145]. Patch-clamping analysis looks more closely at the cell membrane and the ion channels and is used to monitor how a cell responds to electrical or chemical stimuli [4, 114].

1.1.1 Impedance Spectroscopy

Impedance spectroscopy analysis allows for materials to be characterized based on their electrical properties. In biology, since tissues and cells are comprised of charged particles, impedance spectroscopy can be used to identify and sort them [121, 144, 145]. Common uses of impedance spectroscopy in biology include analyzing the electrical conductivity of whole biological systems, such as the respiratory and cardiovascular systems, tissue samples from various organs, and collections of cells. This data can be used to monitor biological functions, characterize and identify various types of tissue, and differentiate between normal and cancerous tissue [121, 144, 145].

1.1.1.1 Impedance Spectroscopy Theory

The components of biological materials, such as tissue or cells, include ions, water molecules, and protein and lipid structures, all of which have a net electric charge and / or a dipolar electrical moment. Due to the electric charge on these components, the biological material can be influenced by an applied electric current, the response of which corresponds to the conductivity and permittivity of the sample [121,144,145]. Therefore, by applying a current to a biological sample a characteristic response based on its impedance can be measured that relates to its specific makeup of individual components. Since the individual components vary from one type of cell or tissue to another, measuring the impedance of a biological sample over a range of frequencies can possibly be used to discriminate different cell and tissue types and to differentiate between healthy and cancerous cells and tissue of the same type.

Several circuit configurations can be used to measure the impedance of a biological

sample [47, 120]. All of the methods use the same basic technique of applying an AC current or voltage and measuring the other. The impedance is then determined from these two values using Ohm's law, where voltage is the product of current and impedance [65]. One method of analyzing the collected impedance data is by displaying the results in a Bode plot that presents the magnitude and phase of the measured complex impedance over the frequency range under investigation. According to Rigaud et al., when using impedance spectroscopy for characterization of either normal or cancerous tissue, it is important to look at both the magnitude and phase data along a spectrum of at least 100 Hz to 10 MHz [120]. Differences in the impedance data between two or more samples may only appear over a certain range of frequencies for the magnitude while other differences may be apparent over a separate range of frequencies for the phase data. The frequency range can be adjusted depending on the sample being tested and what information is being solicited. For individual cells, at a low frequency (below a few mega-hertz) the resistive characteristic of the cell membrane is dominant over the capacitive parameter, and at a high frequency (above a few mega-hertz) the capacitance of the cell membrane is dominant over the resistive parameter [9, 96, 129]. Therefore, investigating changes in the measured impedance in both the low and high frequency ranges will produce valuable information representing different characteristics of an individual cell. This information could also relate to the health of the tissue or cell sample. In previous studies, cancerous cells and tissue have been shown to have different impedance spectroscopy signatures then the normal cells and tissue of the same type [121, 144, 145].

1.1.1.2 Impedance Spectroscopy Applications

Studying the impedance of various biological materials has been an active area of research since the late nineteenth century [121, 130, 144, 145]. Impedance spectroscopy is used to investigate whole biological systems such as the respiratory system, the cardiovascular system, the brain, or even total body impedance [7, 23, 57, 87, 89, 103, 109, 112, 145, 147, 150]. For example, Baker et al. describes how impedance measurements are used in monitoring respiratory activity, especially for detecting apnea in neonates, and Penney uses impedance

spectroscopy to monitor cardiac performance [7, 112].

On a smaller scale, impedance spectroscopy is also used to characterize the tissue of various organs [11, 42, 51, 63, 106, 113, 119, 131, 133, 136, 137, 140, 156] as well as to differentiate between normal and cancerous tissue [14, 19, 67, 72, 110, 122, 125, 134, 139]. Rigaud et al. showed that tissue samples from the muscle, liver, lung, spleen, and intestine each have unique impedance spectra [119]. This information can be used to identify what tissues might be contained within a large segment over which the measurement is performed. Being able to measure a difference between the impedance of normal and abnormal tissue is beneficial for disease diagnosis. Suselbeck et al. used impedance spectroscopy in vivo to detect the different stages of atherosclerosis in an animal rabbit model [140]. Chaudhary et al., Jossinet et al., and Surowiec et al. have all performed impedance studies on breast cancer tissue, and all have found a common trend that the magnitude of the impedance for cancerous tissue is lower than that for normal breast tissue [19, 72, 139].

Collections of cells have also been studied with impedance spectroscopy [9, 30, 33, 48, 49, 78, 155]. Zhao showed that the effects of storing red blood cells can be detected through impedance measurements [155]. Impedance measurements were used by Gheorghiu et al. to study the cell proliferation cycle through budding yeasts and by Giaever et al. to monitor the morphology and motion of human fibroblastic cells while in culture [48, 49]. Bonincontro et al. used impedance spectroscopy to measure the effects of hyperthermia, pH, and culturing conditions on Chinese hamster fibroblasts [9].

Using impedance spectroscopy without the aid of micromachining technology to study individual cells is not commonly found as a current biological analysis technique due to the difficulty of interfacing with single cells on the order of 10 to 100 microns in diameter [3]. An exception to this is the Coulter Counter, which was patented in 1953 [27, 130]. This apparatus uses impedance measurements to count the number of particles in a sample as they are passed between two electrodes. Currently, a large amount of research is being performed that deals with creating microsystems that enable the use of impedance spectroscopy in the analysis of individual cells. These devices are described later in Section 1.2.

1.1.2 Patch-clamping

Patch-clamping analysis is used to perform a localized analysis of the cell membrane to investigate how the ion channels respond to electrical and chemical stimuli [4]. By measuring the current flowing through a small patch of the cell membrane while applying a stimulus, it can be determined if a cell has damaged ion channels or if a certain chemical will force a specific response in the ion channels. Patch-clamping measures the current flowing through a cell's ion channels and can be used to study diseases and chemicals that have a direct effect on ion channel functionality [2, 4, 73, 114].

1.1.2.1 Patch-clamping Theory

The patch-clamp technique is a process by which a small area of the cell membrane is isolated such that electrical measurements corresponding to the ion channel activity in that patch of membrane can be recorded. The isolation is accomplished by placing a hollow, glass micropipette with a fire-polished tip 1 to 2 microns in diameter against the surface of a cell. An electrode is located within the micropipette. The electrical signal of interest is a current that corresponds to the flow of ions through the ion channels within the isolated patch of membrane, typically 1 to 2 pA [4, 114]. Detection of such a small amount of current is complicated when current fluctuations due to noise, Johnson noise current, are considered [2, 50, 114].

The mathematical representation of the Johnson noise current is given in Equation 2.

$$\sigma = \sqrt{\frac{4\kappa T \Delta f}{R}} = 0.018\ pA \tag{2}$$

In Equation 2, κ is Boltzmann's constant ($1.38 \times 10^{-23}\ \frac{J}{K}$), T is temperature (293 K), Δf is the bandwidth of the measurement (1 kHz), and R is the resistance of the ion channel (50 GΩ) [50, 114]. This corresponds to a signal to noise ratio (SNR) of 56 (1 pA of signal to 0.018 pA of noise), which is sufficient to measure channel current. However, when applying a microelectrode to the surface of the cell, a small (with respect to channel resistance, R) amount of leakage resistance, R_{leak}, develops (approximately 10 MΩ). These two resistances

are in parallel with each other and result in a resistance of approximately 10 MΩ. This value now replaces the original 50 GΩ in the Johnson noise current equation. The new current due to noise is 1.3 pA, and the new SNR is 0.8. At this SNR the small amount of channel current would be indiscernible from the noise. To achieve a noise current on the order of 0.1 pA, the parallel combination of channel resistance and leakage resistance would have to be at least 1.6 GΩ, which means the leakage resistance would have to be approximately 1.6 GΩ [2, 50, 114]. The achievement of a high leakage resistance was finally solved in the 1970's by Erwin Neher and Bert Sakmann [2].

To measure the single channel currents, Neher and Sakmann developed a technique in which a small area of membrane was isolated using hollow, glass micropipettes that were a few microns in diameter at the tip. A wire was fixed in place inside the pipette to make the recordings, an electrolytic solution filled the pipette, and the tip of the micropipette was placed against the surface of the cell. This is the earliest technique used to perform patch-clamping, but unfortunately there was still a great deal of noise [2, 50, 114].

By the late-1970's, Neher and Sakmann had almost given up on trying to reduce the noise and obtain better signals from single ion channels. Fortunately, they were eventually able to obtain a seal between the micropipette and the cell membrane (i.e. leakage resistance) two orders of magnitude greater than they had ever done before. The increase in seal resistance was due to a small amount of suction applied to the micropipette. This seal is known as the 'gigaseal' due to the fact that it results in seal resistances well into the gigaohm range. This technique along with future improvements that the two scientists made resulted in the Nobel Prize in Physiology or Medicine awarded to both Neher and Sakmann in 1991 [2,50].

The conventional patch-clamp technique used today follows the original procedure Neher and Sakmann used, including using suction to create the gigaseal between the micropipette and the cell. The electrode inside the micropipette is connected to amplifier and filter circuits that amplify the signal and aid in noise reduction. To complete the electrical circuit and make patch-clamp recordings, a second electrode is located in the extracellular solution in close proximity to the cell under investigation. A diagram of the cell and electrode setup is shown in Figure 3.

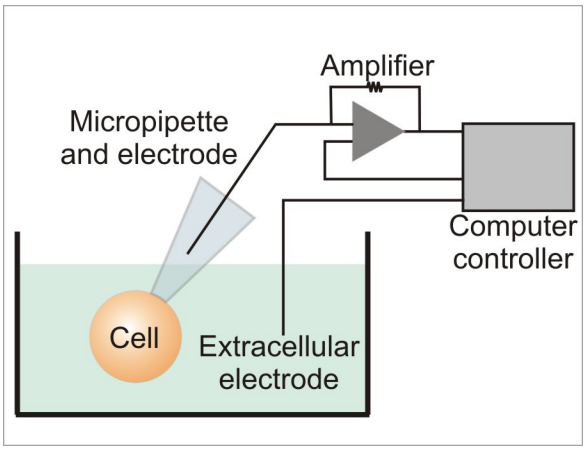

Figure 3: To perform a patch-clamp analysis on a single cell using the conventional technique a cell suspended in solution in a petri dish is found through a microscope and a glass micropipette is positioned against the cell using micromanipulators. Once the cell and micropipette are attached, the ion channel recordings can be collected using the micropipette electrode and extracellular electrode.

Performing patch-clamp analysis begins with placing a dish containing a solution of cells onto the stage of a microscope, which is situated on top of an anti-vibration platform inside of a faraday cage to reduce noise. Micromanipulators, located on either side of the microscope, hold the glass micropipette and the extracellular electrode. After an appropriate cell has been located with the microscope, the micromanipulators are used to move the tip of the micropipette towards the surface of the cell. This process must be slow so as not to puncture the cell membrane with the micropipette. As soon as the tip of the micropipette has made contact with the cell membrane, slight suction is applied to the micropipette to create the gigaseal [2, 50]. Once the patch of cell membrane is attached to the micropipette and the gigaseal is obtained, various types of patch-clamping analysis can be performed: cell-attached, perforated-patch, whole-cell, inside-out, and outside-out (Figure 4).

In cell-attached patch-clamping, the cell and micropipette remain in contact without rupturing the patch of membrane, and therefore a response in the ion channel currents due to a stimulus applied to the extracellular electrode is measured. A perforated patch is an extension of the cell-attached mode. In this case, a solution that causes pores to form in the membrane is placed into the micropipette, thus allowing the patch of membrane to be highly permeable so that a different type of measurement, voltage-clamping, can

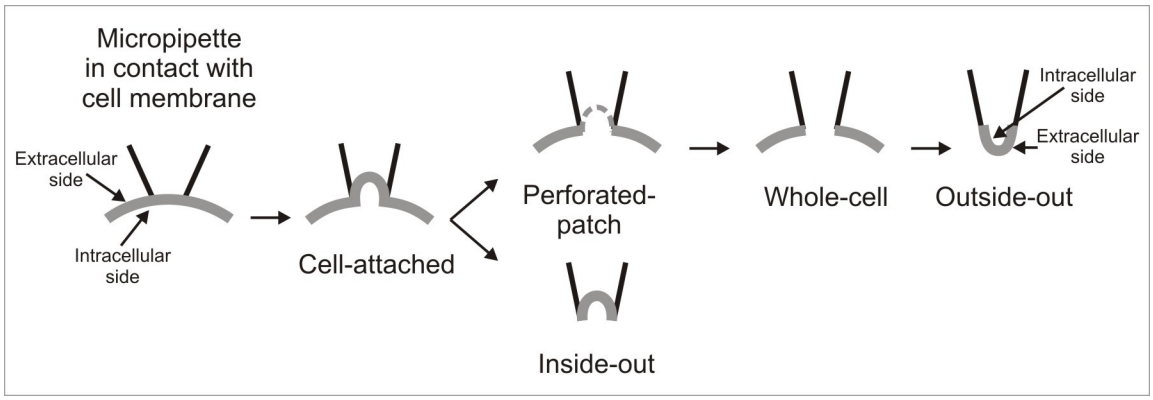

Figure 4: After the giga-seal has been formed between the micropipette and cell, various types of patch-clamp analysis can be performed: cell-attached, perforated-patch, whole-cell, inside-out, and outside-out.

take place. Voltage-clamping is performed on the entire cell rather than the patch of membrane. Whole-cell patch-clamping is similar to perforated patch-clamping in that it allows for voltage clamping to be performed. To produce a whole-cell patch-clamp, after the micropipette is attached to the patch of membrane, a voltage pulse is applied through the micropipette electrode. This pulse causes the patch to break leaving the micropipette electrode and electrolytic solution in direct contact with the intracellular environment.

While in the cell-attached configuration, if the micropipette is retracted, the patch of membrane may stay intact inside the tip of the micropipette creating an inside-out configuration. The inside of the micropipette is in contact with the extracellular side of the membrane, and this allows for different types of experiments to be performed since the solution on both the intracellular face and extracellular face of the patch of membrane can now be controlled. Outside-out configurations are the reverse of the inside-out condition; the inside of the micropipette is in contact with the intracellular surface of the membrane. To create such a patch, first a whole-cell patch attachment is made. Then, once the patch of membrane has been broken, the micropipette is retracted, pulling part of the membrane with it. Once the part of the membrane that is being pulled away from the rest of the cell breaks off, the patch will reform with the opposite side of the membrane facing into the micropipette. Again, this allows for different types of experiments since both the intracellular and extracellular solutions around the patch of membrane can be controlled [2,4,50,73,114].

Although the patch-clamp technique is invaluable to the study of ion channels, it is a highly skill intensive procedure that usually requires the hand of a trained and experienced scientist. Moreover, even with that experience, throughput remains low with 10 to 30 data points per day according to a literature survey [149]. Means to increase throughput include developing microsystems that enable automated and / or parallel patch-clamping. These devices are discussed later in this chapter as part of Section 1.2.

As was mentioned earlier, in the traditional patch-clamp technique, one electrode is positioned in the solution in close proximity to the cell under investigation while the second electrode is inside the glass micropipette. Typically, the micropipette electrode, also known as the reference electrode, is a silver (Ag) wire with a silver chloride (AgCl) coating, and is referred to as an Ag / AgCl electrode [4,50,135]. The choice of reference electrode material is based on the electrochemical reaction between an electrode and an electrolytic solution.

When a simple metal electrode is immersed into an electrolytic solution and electrical measurements are made, layers of built-up charge form around the electrodes. This electrochemical reaction, or electrical double layer, was first described by Helmholtz and is depicted in Figure 5 [8, 127]. The built-up charge creates a potential drop across the electrode / electrolyte interface and is referred to as the electrode potential. In an electrical equivalent circuit, the double layer at the surface of the electrode is represented by a capacitor and is in parallel with a transfer resistance that is determined by the ability of charges to transfer back and forth between the electrode and electrolyte (Figure 6). If charges can move freely between the electrode and electrolyte, then the transfer resistance is almost non-existent, and acts as a short across the capacitor. In this case, the electrode is termed ideally unpolarizable and the electrode potential is not easily affected by current flow across the electrode / electrolyte boundary. In the case of patch-clamping, to measure the small amounts of current, the electrode potential must remain fairly steady; therefore the reference electrodes used are nearly unpolarizable [127].

A stable reference electrode can be formed by coating the electrode with a layer of its soluble salt and immersing it in an electrolytic solution containing a soluble salt of the anions of the electrode coating. For patch-clamp experiments, this composition is provided

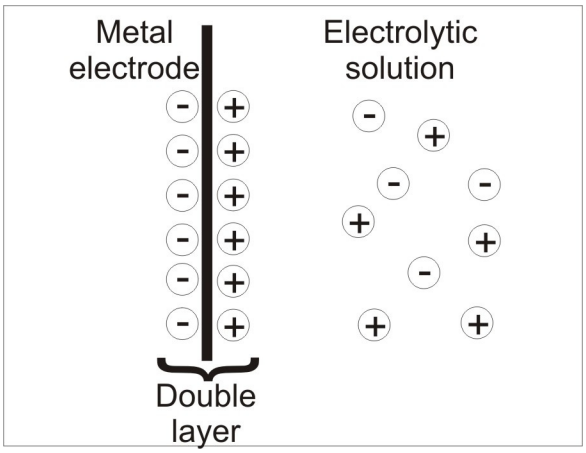

Figure 5: An electrical double layer will form when a metal electrode is used in an electrolytic solution. The charge build-up creates a potential drop across the electrode / electrolyte interface that can interfere with the electrical recordings.

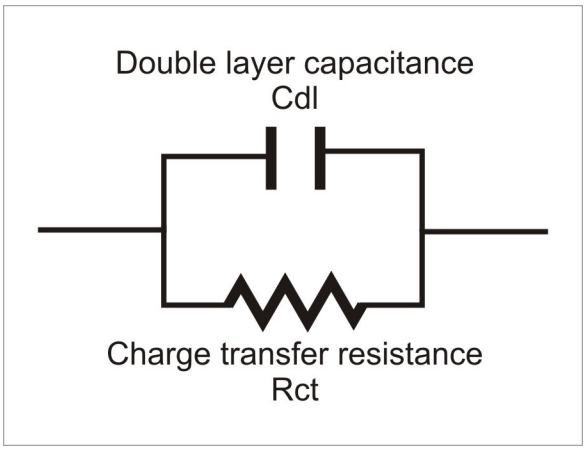

Figure 6: The electrical double layer circuit is comprised of the parallel combination of a capacitor (double layer capacitance) and a resistor (charge transfer resistance).

through a silver (Ag) wire coated in a layer of silver chloride (AgCl) and immersed in a potassium chloride (KCl) solution saturated with additional AgCl. Figure 7 shows a diagram of the electrode / electrolyte configuration within the micropipette. With the combination of the Ag / AgCl electrode and the KCl solution, this type of reference electrode has a low transfer resistance and is therefore fairly insensitive to polarization and maintains an electrode potential of approximately 0.2 V [127].

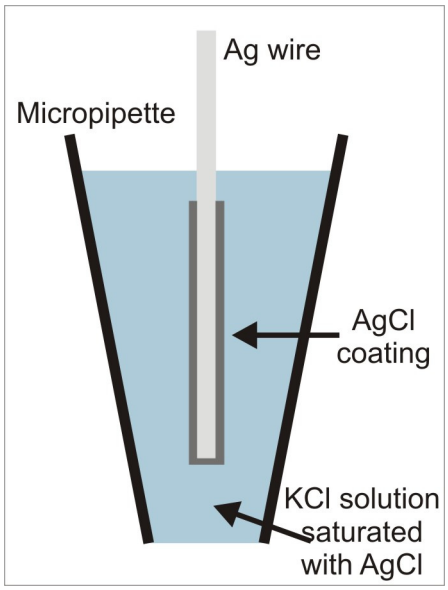

Figure 7: To form an adequate Ag / AgCl reference electrode, the Ag wire is coated in a layer of AgCl. The solution inside the micropipette is KCl saturated with AgCl, which limits the polarization of the electrode.

1.1.2.2 Patch-clamping Applications

There are numerous types of ion channels each serving a different purpose towards the proper function of a cell. Various diseases have been found to be the result of ion channel mutations, and studying how ion channels function can lead towards disease diagnosis and drug discovery. The patch-clamp technique has become an essential tool for the study of ion channels [4, 73].

Ion channel mutations can cause cardiac, neuronal, hearing, vestibular, renal, and metabolic diseases [132]. The following references are examples of the current research that utilizes the patch-clamp technique to study ion channel diseases. Nie et al. used patch-clamping on ventricular myocytes to investigate the effects of sulfur dioxide on cardiac disease [104]. Thinschmidt et al., Nomura et al., and Chen et al. have used the patch-clamp technique on neurons to study Alzheimer's disease [20, 105, 143]. Lucas et al. performed patch-clamping on Chinese hamster ovary cells expressing the human sodium channel to study epilepsy [88]. Liang et al. and Gale et al. studied hearing mechanisms by using patch-clamp analysis on guinea pig outer hair cells (OHC) [44, 85]. Zhang et al. and McCarty et al. have used patch-clamping on oocytes to study the cystic fibrosis transmembrane

conductance regulator (CFTR) gene, i.e. the gene responsible for cystic fibrosis [94, 154]. Additional reviews of ion channel diseases where patch-clamping is used can be found in Ashcroft, Jurkat-Rott et al., Cooper et al., and Shieh et al. [4, 25, 73, 132].

1.2 Microsystems for Whole-cell Analysis

Impedance spectroscopy is commonly applied to large systems, such as the cardiovascular or respiratory systems, tissue samples, and large collections of cells. Using impedance spectroscopy to study individual cells has been limited due to the difficulties of interfacing with a cell that is on the order of 10 to 100 microns in diameter. Patch-clamping does interface with individual cells, however the process to do so is extremely time consuming. Thus, the throughput of patch-clamp analyses is limited.

These problems are now being addressed through advances in micromachining technologies [91, 102]. Since features on the order of tens of microns are easily achieved in microsystems, such as valves, pumps, channels, and electrodes, the ability to quickly and easily interface with individual cells is possible. Microsystems can also increase the throughput of biological studies by reducing the complexity of the experimental setup, incorporating multiple analysis functions on a single device, and addressing an array of individual cells simultaneously [3].

Some biomedical applications that have been addressed through microsystems include: drug delivery, cell filtering and trapping, flow cytometry, and electroporation [15, 16, 21, 31, 62, 69, 84, 86, 95]. The advances in microsystems towards biomedical applications over the past two decades are further discussed in the reviews by Verpoorte et al., Andersson et al., Dario et al., and Reyes et al. [3, 29, 117, 146].

1.2.1 Microsystems for Impedance Spectroscopy

Microsystems used for impedance spectroscopy analysis have been developed by various research laboratories. The following are examples of some of these research efforts. In Ayliffe et al., a microsystem was fabricated out of glass and SU-8 epoxy-based photoresist and was used to make impedance measurements on ionic salt solutions, air, deionized (DI) water, human polymorphoneuclear leukocytes (PMN's), and teleost fish red blood cells

(RBC's) [6]. The impedance was measured over a frequency range of 100 Hz to 2 MHz, and the different samples were found to be distinguishable based on the magnitude and phase data. A microsystem made of glass, poly(dimethylsiloxane) (PDMS), and a photosensitive polyimide was fabricated by Gawad et al. and was used to differentiate between erythrocytes, leukocytes, and embryonic renal cells based on impedance measurements over a frequency range of 100 kHz to 15 MHz [45, 46]. The fabrication of a silicon (Si) and glass microsystem is described in Gomez et al. that is used to perform impedance spectroscopy analysis over a frequency range of 100 Hz to 1 MHz to detect the presence of bacterial cells in solution [54, 55]. Metz et al. used a combination of spin-on photosensitive and non-photosensitive polyimides to create thin-film, implantable electrodes [97]. As initial characterization, they collected impedance measurements over a frequency range of 100 Hz to 1 MHz with saline. Further testing involved impedance measurements on the muscle tissue of giant hissing cockroaches. Medoro et al. designed and fabricated a printed circuit board (PCB) device that can be used to detect microorganisms in a microfluidic channel through impedance measurements [96]. In Ozaki et al., a Si and silicon dioxide (SiO_2) microsystem was fabricated and used to detect the effects of drugs on ganglion cells through impedance measurements at a frequency of 5 kHz [107]. Glass and SU-8 epoxy-based photoresist was used in Yong et al. to fabricate a microsystem that was able to detect the presence of human prostate carcinoma cells (DU-145) based on impedance spectroscopy measurements at a frequency of 500 Hz [153]. A majority of these microsystems operate in a similar manner in that the sample containing the cells is sent through a micro channel and electrodes located at various points along the channel are used for recording the electrical signals.

1.2.2 Microsystems for Patch-clamping

To perform patch-clamping analysis in a microsystem, the cell must be positioned against a small (a few microns depending on the size of the cell under investigation) thru hole with enough force to create the necessary high-resistance gigaseal. Various research laboratories are attempting to fabricate microsystems for patch-clamp analysis and, therefore,

are trying to create this thru-hole using different types of MEMS techniques and materials. In Matthews et al., silicon (Si), silicon dioxide (SiO_2), and silicon nitride (Si_3N_4) were used to fabricate a microsystem with thru-holes ranging in diameter from 0.8 μm to 12.3 μm [93]. Cheung et al. fabricated an array of patch-clamping sites in an SOI (Si on insulator) wafer with additional SiO_2 and Si_3N_4 depositions [22]. They reported thru-hole diameters of 1 μm, 3 μm, and 10 μm and conducted preliminary whole-cell patch-clamping experiments on oocytes. Thru-holes of approximately 1 μm in diameter in a glass substrate were fabricated by Fertig et al. and were used to collect whole-cell patch-clamp recordings from mouse neuroblastoma cells and Chinese hamster ovary (CHO) cells [40, 41]. A Si, SiO_2, and glass microsystem with integrated electrodes was fabricated by Lehnert et al. and contains thru-holes from 2.5 μm to 10 μm in diameter [81, 82]. Using CHO cells, the microsystem was used to measure the seal resistance between the cell and the thru-hole and collect current measurements showing a cell response to a voltage stimulus. In Klemic et al., poly(dimethylsiloxane) (PDMS) was used to fabricate a patch-clamp microsystem with an array of thru-holes with diameters of 1 μm to 10 μm [75]. The array was also used to perform cell-attached patch-clamping on oocytes, and seal resistances of approximately 10 GΩ between the oocytes and the thru-holes were achieved. Tanabe et al. fabricated a microsystem out of Si, SiO_2, and a photosensitive polymer [142]. The microsystem contained an array of thru-holes less than 10 μm in diameter that were on top of a microfluidic channel. Preliminary experiments to test the ability to collect a sample on top of the thru-hole using suction through the micro channel were successfully performed with micro beads 15 μm in diameter. Peng et al., Pandey et al., and Schmidt et al. have also worked towards developing microsystems to be used for patch-clamping analysis using Si, SiO_2, and PDMS [108, 111, 126]. Besides academic research laboratories, companies such as AVIVA Biosensors Corporation, Axon Instruments, Molecular Devices, Sophion Bioscience, and Nanion Technologies are also developing and manufacturing systems that can perform high-throughput patch-clamp analysis [5, 128, 149].

1.3 Objective: Develop a Microfluidic System for whole-cell Analysis Using Low-Cost Micromachining Techniques

1.3.1 A Microfluidic System for Whole-cell Analysis

A key to improving disease diagnosis and drug discovery is by increasing the throughput of the already established techniques of whole-cell analysis. As current research is demonstrating, this high-throughput performance can be enabled through microsystems. Therefore, part of the objective of this research project is to develop a microfluidic system designed for whole-cell analysis. Two types of whole-cell analysis, impedance spectroscopy and patch-clamping, where chosen as the applications with which to test the viability of the developed microsystem.

The fabrication process utilizes sheets of the polyimide, Kapton® (DuPont), and the techniques of laser ablation, microstenciling, and heat staking to realize a biocompatible, multi-layer microfluidic system on a flexible substrate. In the work of Han et al., another microsystem that addresses both impedance spectroscopy and patch-clamping was developed [59]. Their device is similar in design to the microfluidic system developed in this research: both are meant to enable high-throughput impedance spectroscopy and patch-clamping analyses; both incorporate an array of analysis sites; and both use the same theory of operation. The difference is between the materials and methods used for the fabrication as well as the biological materials used during the testing of the systems. The microsystem developed by Han et al. is a silicon based device and therefore used more standard MEMS fabrication techniques such as patterning through photolithography and wet and dry etching, and their target biological materials for testing were chromaffin cells and breast cancer cells [58, 61]. The target biological materials for this system are head and neck cancer cells and tissue samples. The following chapters describe in detail the design, fabrication, and testing of this microfluidic system.

1.3.2 Significance of Using Low Cost Micromachining Materials and Techniques

The previously mentioned microsystems used for whole-cell analysis use typical materials found in MEMS processing: silicon, SiO_2, Si_3N_4, and glass. Some also incorporate polymers, such as PDMS and some spin-on photosensitive polymers, and the epoxy-based photoresist SU-8. The processing of these materials also follows standard MEMS fabrication techniques: photolithography for patterning metal traces and other features into the substrates; wet and dry etching of Si, SiO_2, glass, and polymers; and bonding with UV curable adhesives, PDMS, or anodic bonding between Si and glass. These standard MEMS processes require an infrastructure consisting of expensive pieces of equipment typically housed in a cleanroom environment. While this necessary infrastructure may be readily available to large universities and industrial companies, it may not be as accessible to smaller, more independent labs. Additionally, these methods involve serial processing from layer to layer, and therefore can require longer design to prototype cycles.

Part of the objective of this research project is to demonstrate that a less expensive (in terms of fabrication) microfluidic system can be attained through non-standard micromachining materials and techniques. Towards this end, laser ablation, microstenciling, and heat staking sheets of polyimide have been characterized and integrated to realize a multi-layer microfluidic system with electrical functionality for whole-cell analysis. This process requires less infrastructure than that for typical MEMS processing and allows for a faster design to prototype cycle. By also providing the ability to integrate complex arrangements of multi-layer electrical functionality, this non-standard process could be adapted for numerous applications to develop a variety of low-cost microfluidic systems.

CHAPTER II

MICROSYSTEM DESIGN AND THEORETICAL ANALYSIS

To aid in the biological analysis of tissue samples and cells, such as in impedance spectroscopy and patch-clamping, a microsystem needs to be able to perform certain functions including immobilizing the biological sample at analysis sites and interfacing that sample with electrodes. To perform these functions, certain features are required and include analysis sites, fluidic channels, and metal traces for electrical functionality. As part of the design of such a microsystem, a method to control the samples and fluids within the system also needs to be determined. This chapter discusses the design that was chosen and the method by which the microsystem is intended to be operated.

After a design has been established, theoretical analysis of the design and performance can be used to verify that the microsystem will function as intended. This chapter therefore also discusses the theoretical analysis and modeling of the microsystem.

2.1 Microsystem Design

2.1.1 Microsystem Layout

The two types of biological analysis techniques that this microfluidic system is to be used for are impedance spectroscopy and patch-clamping. Another objective of this microsystem is that it be able to collect data from separate biological samples in parallel, thus increasing throughput. To accommodate both analysis techniques and to allow for parallel data collection, the layout of the microsystem was determined such that it incorporates an array of analysis sites, or cavities, with each cavity interfacing with a fluidic channel and separate sets of electrodes. A multi-layer fabrication approach, using polyimide as the substrate material, allows for the fluidic channels, access ports, and cavities to be placed throughout the system. The electrical functionality can also be easily incorporated into such a multi-layer

system by placing metal traces between the layers of polyimide, which act as sufficient insulators between the metal traces. A diagram of the microsystem is shown in Figure 8. The six polyimide layers are labeled as follows (from bottom to top): base, isolation, channel, via, bottom cavity, and top cavity. The sample being tested - a liquid solution containing cells or a tissue sample - is contained on top of the array of analysis cavities in a containment well that is attached to the top of the microsystem and surrounds the array of cavities.

The microsystem substrate is comprised of six layers of polyimide and two metal layers and contains an array of individual cavities. The cavities are in contact with a backside microchannel through small vias located at the bottom of the cavities. Each cavity has a corresponding electrode located at the bottom of the underlying fluidic microchannel. During device operation, access to the fluidic microchannel occurs through inlet and outlet ports located at either end of the channel. Additionally, separate sets of two or four electrodes interface each of the cavities in the array. With more than two electrodes per cavity, performing additional types of analyses is possible. For example, by surrounding the biological sample with electrodes, constructing a 3D image of the sample could be possible through impedance measurements (impedance tomography) [100]. To show that this multilayer microfluidic system could be used for such other applications, some of the cavities in the array interface with four electrodes. However, to simplify the fabrication, the majority of the cavities interface with only two electrodes.

2.1.2 Theoretical Operation of the Microsystem

The operation of the microfluidic system begins by dispensing a small volume of solution containing cells into the containment well on top of the array of cavities. To pull the suspended cells into the cavities, a negative pressure is formed inside the fluidic channel. This is done by sealing off the outlet port of the channel and using suction on the inlet of the channel. With the appropriate pressure applied, the cells flow into the cavities. The cells are restricted from flowing into the fluidic channel by the via layer in the device. The via holes are big enough to allow fluid through, but they are too small for a cell to pass through. Once the cells are in the cavities, the negative pressure is maintained so as to keep

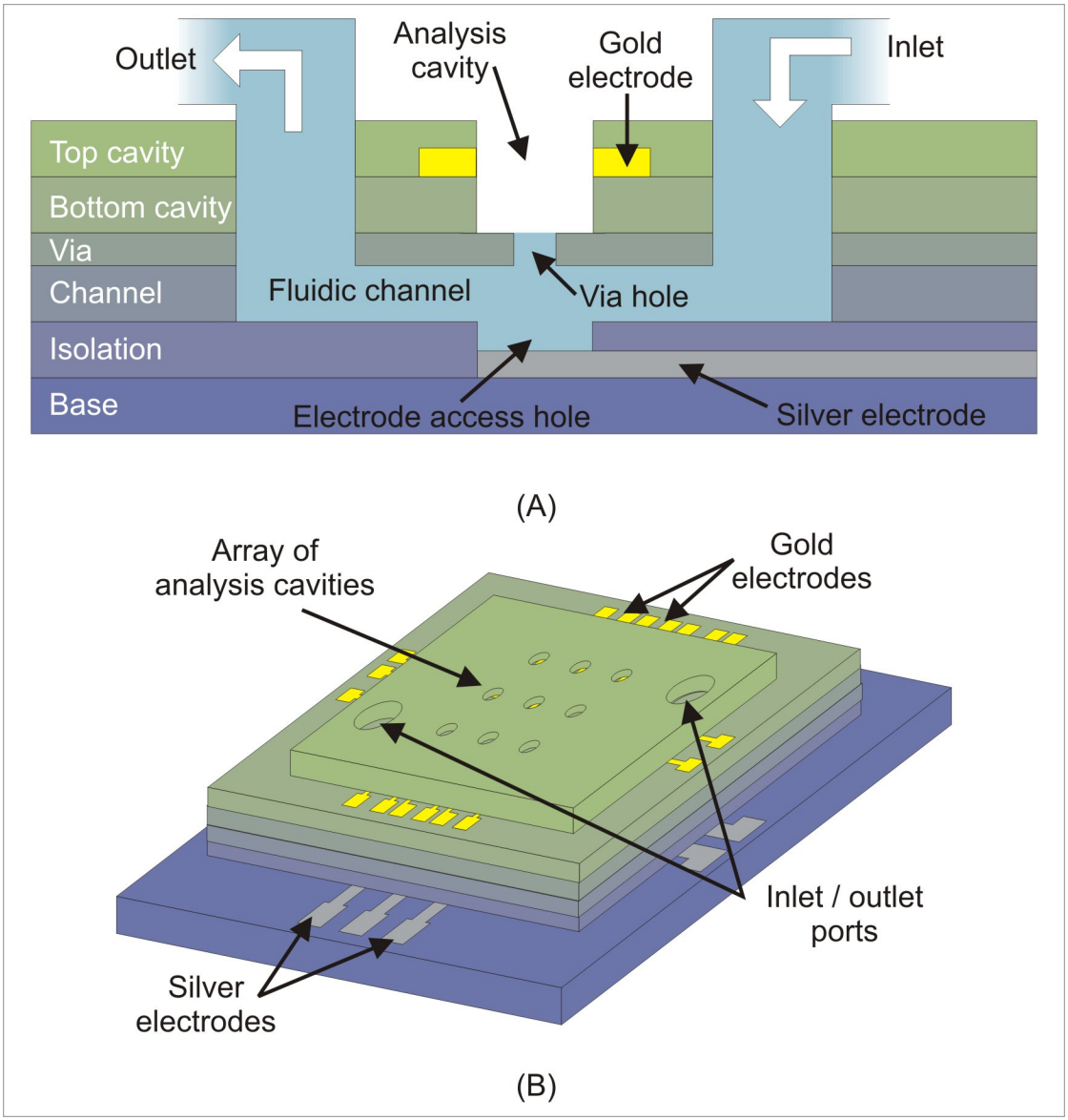

Figure 8: The microfluidic system is made of six layers of polyimide patterned separately and bonded together. The layers are labeled as follows (from bottom to top): base, isolation, channel, via, bottom cavity, and top cavity. (A) The cross-section shows how one of the analysis cavities and the inlet and outlet ports interface to the underlying fluidic channel. In this view, it can also be seen how the gold electrodes used for impedance spectroscopy interface around the analysis cavity and how the analysis cavity accesses the silver electrode at the bottom of the fluidic channel through the via hole. (B) The 3D perspective shows that a single device contains an array of analysis cavities (nine in this picture). The single fluidic channel is accessible through the inlet and outlet ports, and the gold and silver contact pads are along the periphery of the system.

the cell in position during analysis. Impedance spectroscopy or patch-clamping can then be performed.

For impedance spectroscopy analysis, the impedance between opposing electrodes that interface each cavity is measured (Figure 9). For patch-clamp analysis, the microfluidic system is designed such that it mimics the conventional patch-clamp technique (Figure 10). The via hole located between the microfluidic channel and the cavity acts as the end of the micropipette in a typical patch-clamp experiment. The reference electrode within the micropipette is provided in the microfluidic system as the silver electrode directly beneath the cell cavity at the bottom of the microfluidic channel. To use the microfluidic system to perform patch-clamp experiments, first a giga-seal must be formed between the cell and the via hole at the bottom of the cell cavity. This is confirmed by measuring the resistance between one of the cell cavity electrodes and the corresponding electrode located at the bottom of the fluidic channel. Once a giga-seal has been established, the current through either the patch of membrane sealed in the via hole or the entire cell membrane, depending on which type of patch-clamp analysis is being performed, is measured using the same two electrodes. Greater detail on both types of cellular analysis is given as part of the experimental methods in Chapter 3.

2.1.3 Design Versions of the Microsystem

Over the course of this project, certain changes have been made to the design of the microfluidic system to account for various issues encountered during fabrication and testing. The most significant changes were to cavity diameter, number of cavities in a device, size and number of alignment features, and number of separate fluidic channels per device. The changes are divided among four distinct versions of the microfluidic system. Figures 11, 12, 13,and 14 show schematic drawings of all four design versions. The first version of the microfluidic system contains an array of 16 small-diameter (15 μm) cavities each interfacing with electrodes. This version uses only large (4.7625 mm diameter) alignment features, and incorporates a single fluidic channel for all 16 cavities. The second version of the system has an array of only eight cavities with larger diameters (240 μm). Again only large alignment features are used and all eight cavities interface with a single fluidic channel. Version three of the microfluidic system maintains eight large-diameter cavities

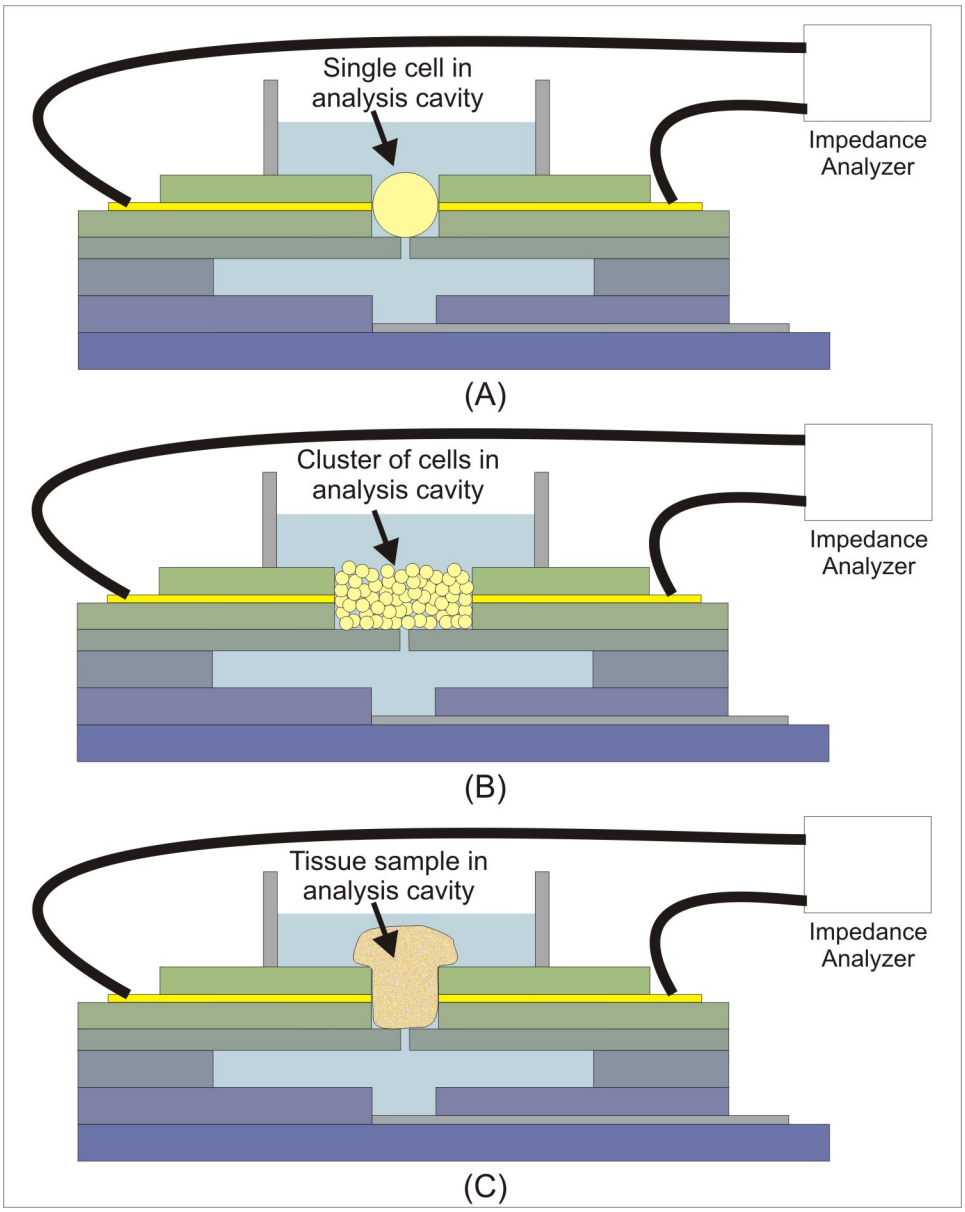

Figure 9: (A) For impedance spectroscopy experiments, a single cell, (B) a cluster of cells, (C) or a tissue sample is placed into the analysis cavity and wires bonded to the gold contact pads are connected to an impedance analyzer.

and a single fluidic channel, but for the alignment, it has both large and small (240 μm diameter) holes. Version four again has eight large-diameter cavities and uses both large and small alignment features, but rather than a single fluidic channel for all the cavities, it has four separate fluidic channels, each with access to two cavities.

The increase to the cavity diameter aids in alignment, both from layer to layer, but

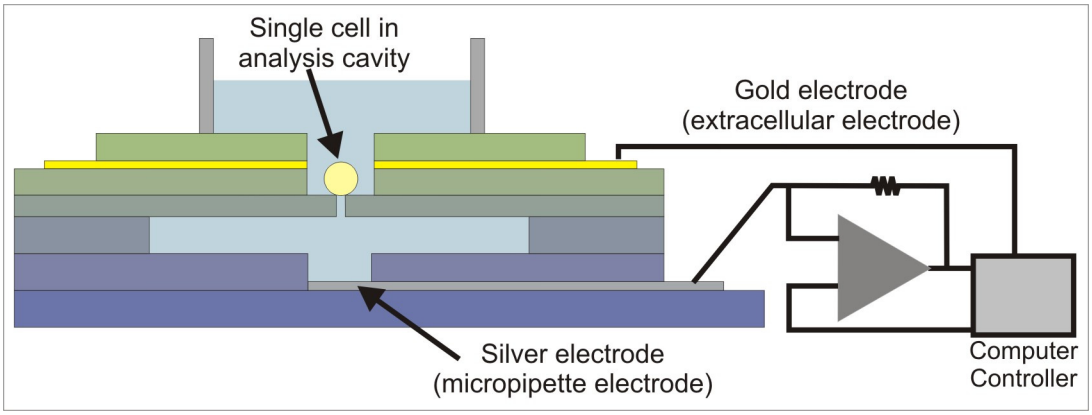

Figure 10: For patch-clamp experiments, a single cell is pulled into the analysis cavity and against the via hole using suction through the microfluidic channel. Wires bonded to the silver contact pad and to a gold contact pad corresponding to one of the gold electrodes at the analysis cavity are connected to the patch-clamp measurement equipment.

also from Kapton® layer to microstencil, a process that is described as part of the fabrication procedure in Chapter 3. Then, by decreasing the number of cavities per device, the microstencil for the electrode patterning is less complicated, and therefore easier to fabricate and use. Adding small alignment features greatly increases the ability to align all six Kapton® layers prior to bonding. Finally, by adding additional fluidic channels, fewer cavities are controlled by a single channel. This helps when trying to use negative pressure in the channel to move cells that are initially suspended in solution into a nearby cavity.

2.1.4 Overview of the Fabrication Steps

The fabrication of the multi-layer microfluidic system consists of laser ablation, microstenciling, heat staking, and packaging. First, features for the fluidic channel, access ports, cavities, via holes, and alignment marks are patterned into the individual polyimide layers through ablation using either an excimer or a CO_2 laser. For the metalization step, a microstencil first needs to be fabricated. Then, the metal is deposited onto the polyimide layer through the microstencil. Next, the patterned and metalized polyimide layers are aligned and bonded together by heat staking. For the packaging, the containment well is formed using stereolithography (SLA). Finally, the containment well and tubing are glued onto the microsystem and wires are electrically bonded to the metal contact pads and then sealed with epoxy. Each of these processing steps is described in greater detail as part of

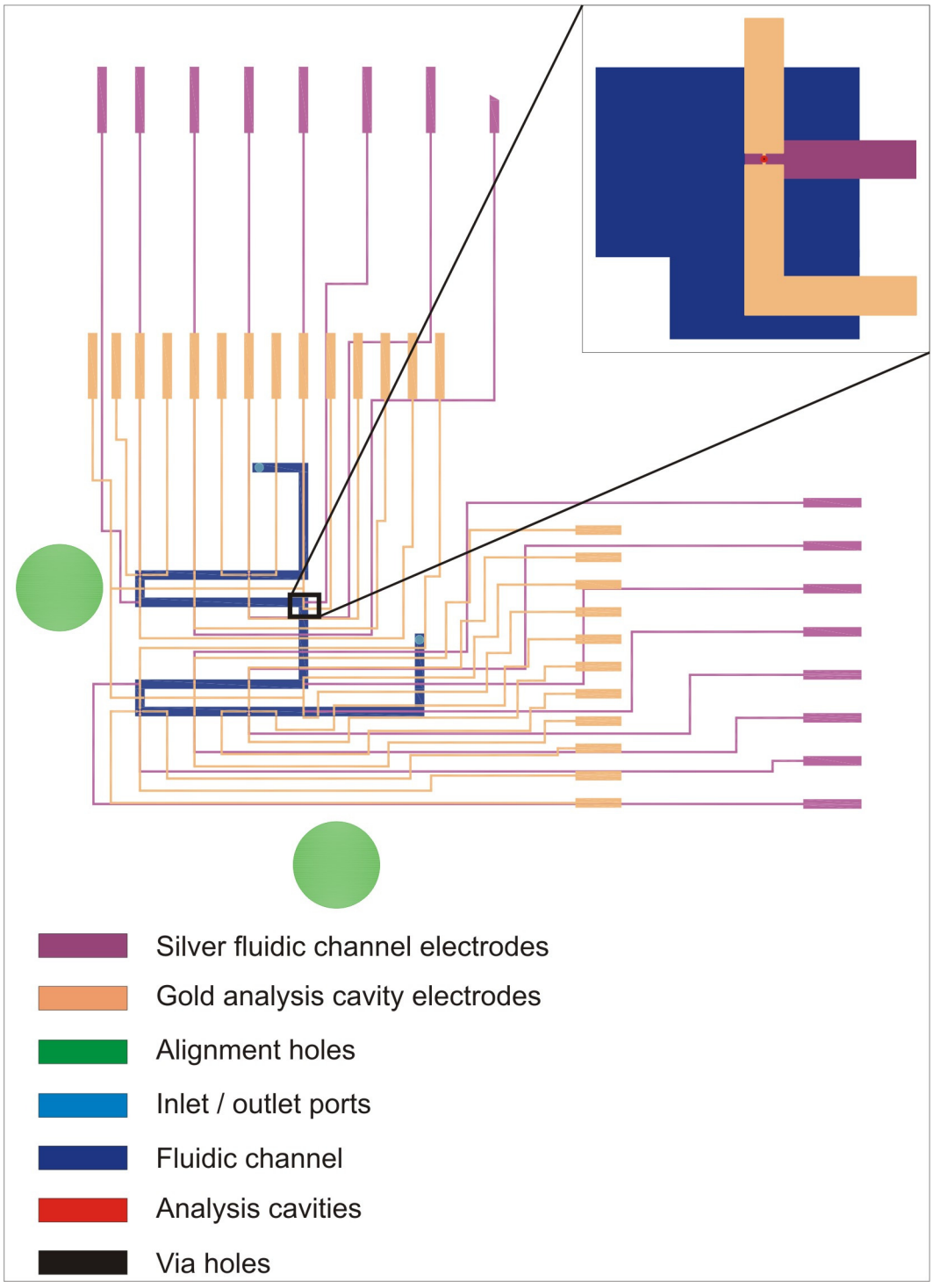

Figure 11: The first version of the microfluidic system contains an array of 16 small-diameter (15 μm) analysis cavities all interfacing with a single microfluidic channel. This design version uses only large alignment features (4.7625 mm diameter).

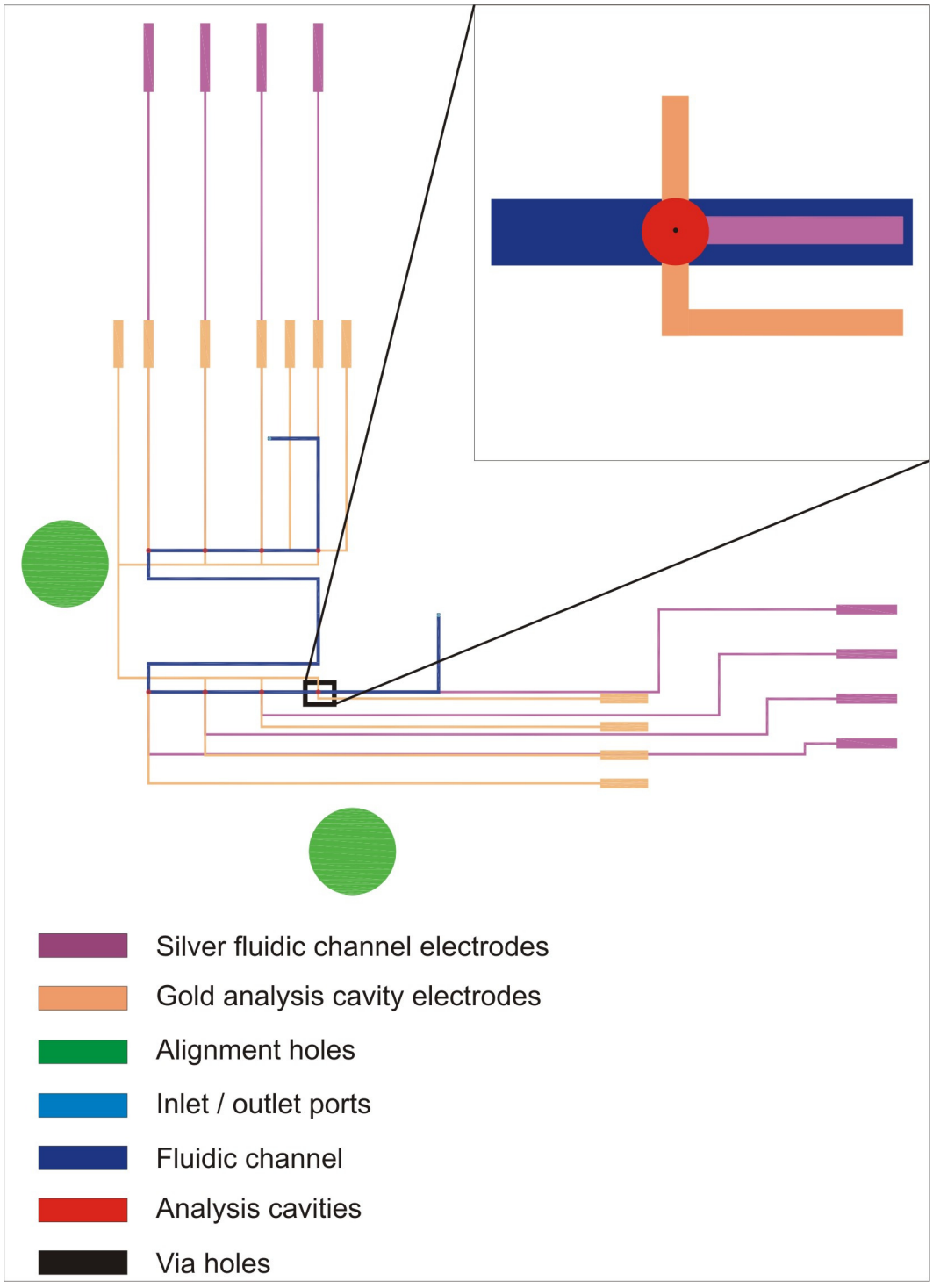

Figure 12: The second version of the microfluidic system contains an array of 8 large-diameter (240 μm) analysis cavities all interfacing with a single microfluidic channel. As with design version 1, only large alignment features (4.7625 mm diameter) are used.

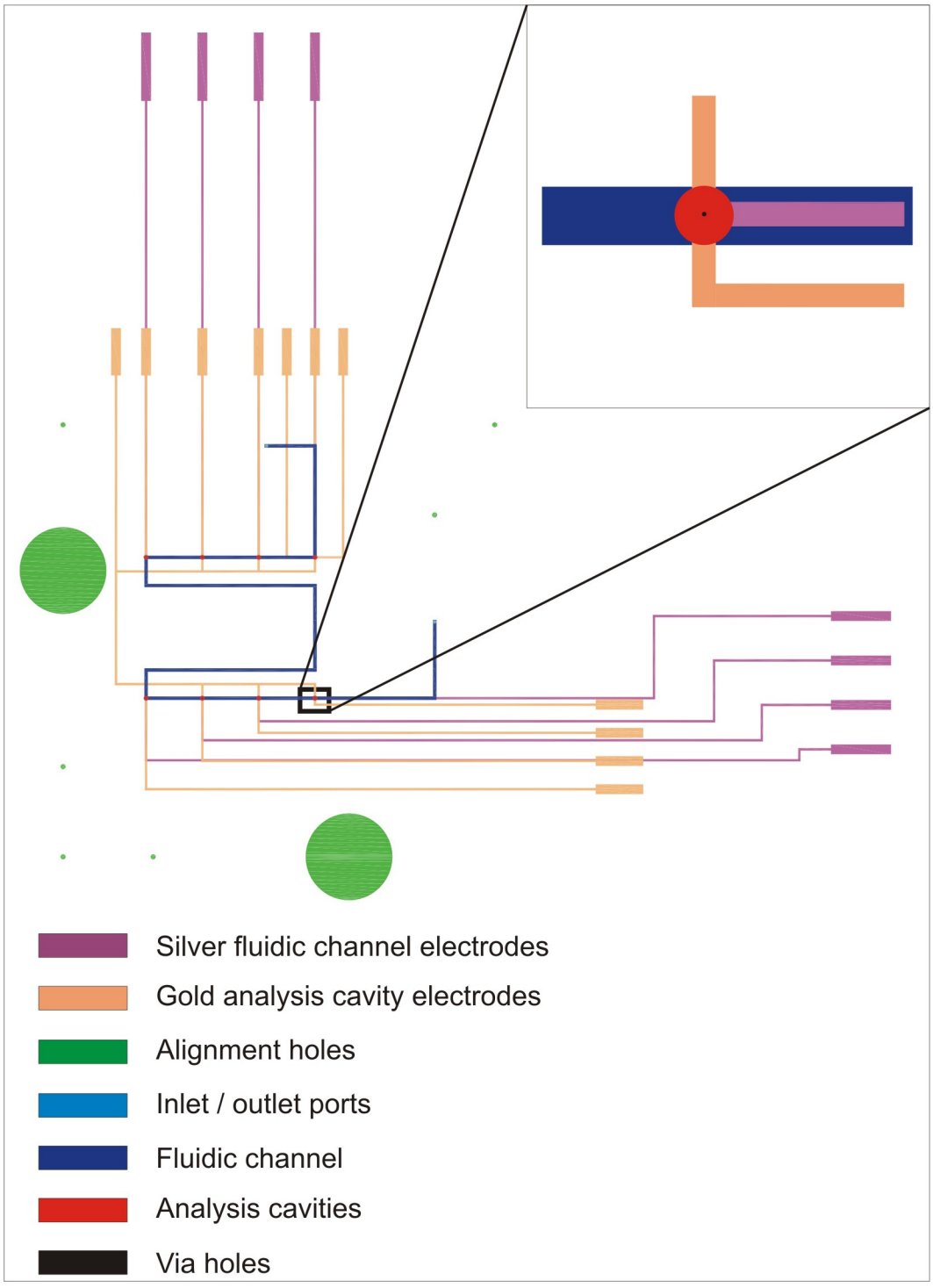

Figure 13: The third version of the microfluidic system contains an array of 8 large-diameter (240 μm) analysis cavities all interfacing with a single microfluidic channel. Unlike the two previous versions, version 3 uses both large (4.7625 mm diameter) and small (240 μm diameter) alignment features.

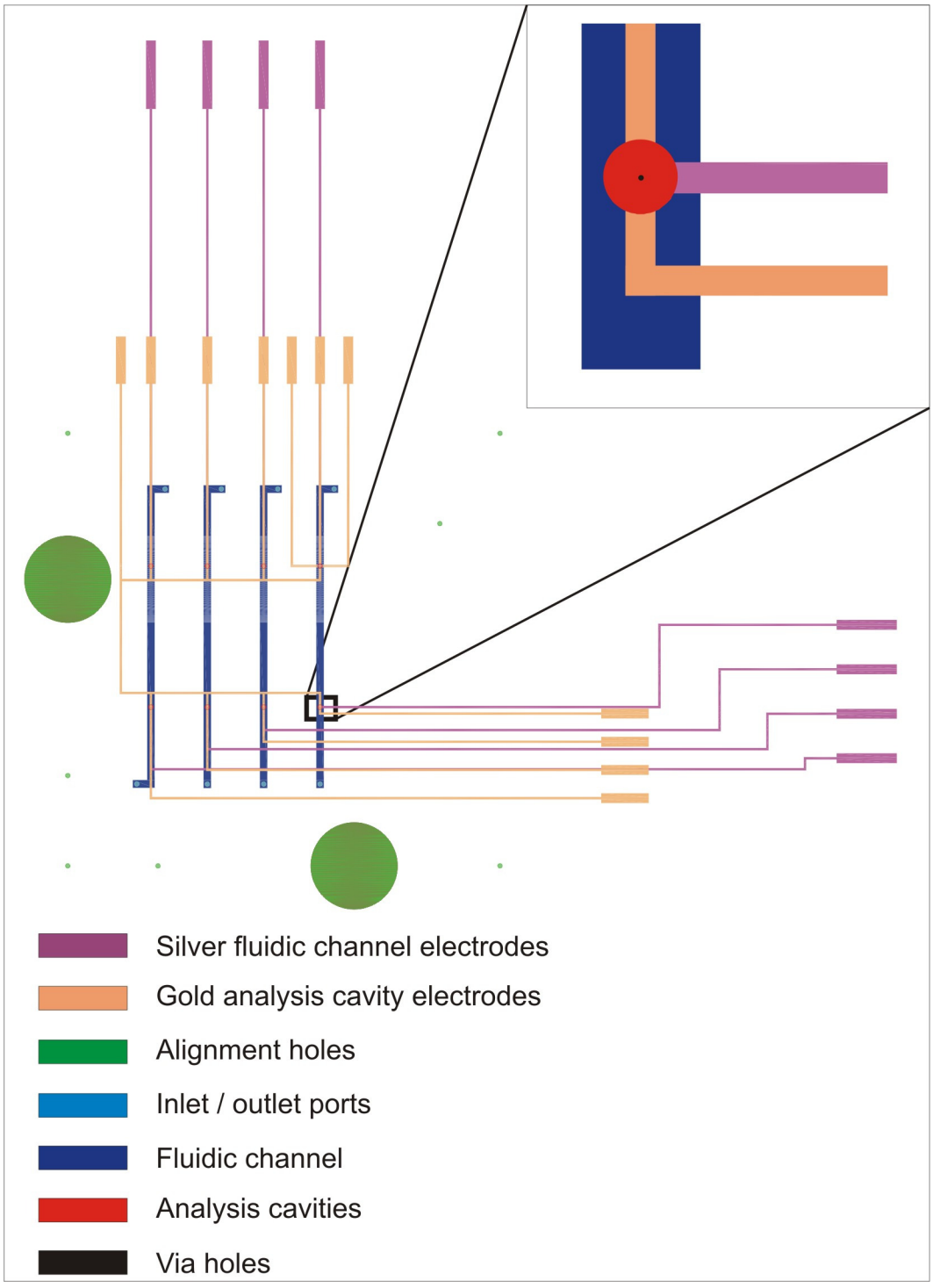

Figure 14: The fourth version of the microfluidic system contains an array of 8 large-diameter (240 μm) analysis cavities and uses both large (4.7625 mm diameter) and small (240 μm diameter) alignment features. Unlike all three previous versions, this design contains four independent fluidic channels each interfacing with only two analysis cavities.

the fabrication procedure in Chapter 3.

2.2 Theoretical Analysis and Modeling of the Microsystem

Theoretical analysis and modeling of any system is used to verify that the system functions as it was designed to function. For this project, the stability of the microfluidic system with respect to fluid mechanics was analyzed using the governing fluid mechanics equations. Then, an equivalent electrical circuit of the microfluidic system was developed to verify the collected impedance spectroscopy data.

2.2.1 Structural Stability Analysis of the Microsystem using Fluid Dynamics

During normal operation of the multi-layer microfluidic system, it is necessary that the layers not delaminate. The most critical location where delamination can take place is between the layers that form the microfluidic channel. The delamination can occur if a high enough pressure is exerted on the walls of the channel when fluid is pushed through the channel.

As was shown earlier in Figure 8, the fluidic channel is formed from three of the six polyimide layers. The isolation and via layers form the bottom and top walls of the channel respectively. The side walls of the channel are part of the channel layer itself. Normal operation of the microfluidic system involves filling the microfluidic channel with a cell buffer solution prior to dispensing the solution of cells on top of the array of cell cavities. The limit of how much pressure can be applied to the microfluidic channel before it begins to fail needs to be determined so that delamination of the polyimide layers will not occur. Although visual inspection of the channel during operation is sufficient in observing the formation of leaks, using theoretical analysis can help to more fully understand the behavior of the channel due to fluid dynamics.

To fill the microchannel, tubing is used to connect the inlet of the channel to a syringe that is controlled by a syringe pump that pumps at a user specified volumetric flow rate. Based on the set flow rate, the walls of the microchannel will experience a certain pressure. From the theories of conservation of energy and conservation of momentum, mathematical relationships between flow rate and pressure for fluid mechanics are derived [43,101]. These

governing equations for fluid dynamics are the Navier-Stokes equations. Due to their complexity, certain assumptions about the flow must be made before solutions can be found. By assuming a Poiseuille flow, which is an incompressible Newtonian fluid characterized by a fully-developed, laminar flow in a straight, horizontal, and circular tube, the Navier-Stokes equations simplify into Poiseuille's law as shown in Equation 3.

$$Q = \frac{\pi R^4 \Delta p}{8 \mu l} \tag{3}$$

In Poiseuille's law, Q is the volumetric flow rate $[\frac{m^3}{sec}]$, R is the radius of the tube [m], Δp is the pressure drop $[\frac{kg}{m \cdot sec^2}]$ between two points in the tube a distance l [m] apart, and μ is the viscosity of the fluid $[\frac{kg}{m \cdot sec}]$.

The first assumption made to obtain Poiseuille's law is that of an incompressible Newtonian fluid. This type of fluid is one in which a constant density and viscosity are maintained across the fluid such as water at a specific temperature. The next assumption is that the flow is fully-developed. As a fluid enters a tube, its initial velocity profile (the velocity of the fluid with respect to its distance from the wall) is uniform. However, as the fluid travels further into the tube, viscous forces between the fluid and the wall increase and cause the velocity profile to change. The profile continues to change until the flow reaches a point in the tube a specified distance from the entrance, l_e. After this point, the velocity profile will remain constant (so long as the tube remains straight) and is therefore considered to be fully-developed. For a laminar flow, the entrance length is calculated using Equation 4.

$$l_e = 0.06 \cdot D \cdot Re \tag{4}$$

In this equation, D is the diameter of the tube [m], and Re is a unitless term called the Reynolds number. The Reynolds number is the ratio of the inertia to viscous effects in the flow and is a function of fluid viscosity (μ), fluid density (ρ) $[\frac{kg}{m^3}]$, mean velocity of the fluid (V) $[\frac{m}{sec}]$, and the diameter of the tube, as shown in Equation 5.

$$Re = \frac{\rho V D}{\mu} \tag{5}$$

The next assumption is that the flow is laminar. For laminar flow, the velocity vector has only one component, which is in the same direction of the pipe. The velocity vector for turbulent flow is dominated by the velocity in the direction of the pipe, but it also contains components in other directions. To distinguish between these flow profiles, the Reynolds number is used. Generally, if $Re < 2100$, the flow is dominated by viscous effects and is considered laminar. If $Re > 4000$, inertia dominates the flow, and the flow is considered turbulent. Between 2100 and 4000 the flow may switch between laminar and turbulent flow in a random fashion and is considered transitional flow.

The final assumption needed to use Poiseuille's law is that the flow is contained in a straight, horizontal, and circular tube. Therefore, in order to use Poiseuille's law for a microchannel with a rectangular cross-section, an equivalent diameter needs to be determined. This equivalent diameter is also called a hydraulic diameter and is calculated using Equation 6.

$$D_h = \frac{4 \cdot A}{P} \tag{6}$$

In this equation, A is the cross-sectional area of the channel [m^2], and P is the wetted perimeter of the channel [m]. Therefore, for a channel with a cross-sectional width, w, and height, h, the hydraulic diameter simplifies to that shown in Equation 7.

$$D_h = \frac{2 \cdot h \cdot w}{h + w} \tag{7}$$

Finally, the Poiseuille's law equation can be rewritten in terms of the mean velocity of the fluid and rearranged to calculate pressure drop based on flow rate as shown in Equations 8, 9, and 10.

$$V = \frac{Q}{\pi R^2} \tag{8}$$

$$V = \frac{R^2 \Delta p}{8 \mu l} \tag{9}$$

$$\Delta p = \frac{8 \mu l V}{R^2} \tag{10}$$

Now Equation 10 can be used to solve for the theoretical pressure drop across the channel

in this microfluidic system for varying flow rates of water. For this analysis, the following parameters are used:

$\mu = 0.001002 \frac{kg}{m \cdot sec}$,

$\rho = 998 \frac{kg}{m^3}$,

$h = 50.8 \times 10^{-6}$ m,

$w = 500 \times 10^{-6}$ m, and

$l = 63.4 \times 10^{-3}$ m.

From Equation 7, D_h is found to be 92.2×10^{-6} m. Under normal operation of the microfluidic system, the volumetric flow rates (Q) through the channel are between 0 and 2.0 $\frac{mL}{hr}$, but for this analysis, flow rates up to 5.5 $\frac{mL}{hr}$ are considered. A flow rate of 5.5 $\frac{mL}{hr}$ equals 1.53×10^{-9} $\frac{m^3}{sec}$, which for the channel dimensions listed above corresponds to a flow rate (V) of 6.01×10^{-2} $\frac{m}{sec}$. Based on Equation 5, this range of flow rates leads to a maximum Reynolds numbers of 5.53, which means the flow through this channel is indeed laminar. Additionally, from Equation 4, the maximum entrance length (l_e) for this channel is 30.6×10^{-6} m. Therefore, for a 63.4×10^{-3} m long channel, an entrance length of 30.6×10^{-6} m is negligible, and the fully developed flow is assumed to be over the entire length of the channel.

As was shown earlier in Figures 11, 12, 13, and 14, the channel in the first three versions of the microfluidic system is not straight, rather it contains nine bends. For laminar flow with Reynolds numbers less than 15, it has been experimentally found that bends do not create significant additional pressure drops across the channel [152]. Therefore, for this analysis, the channel is assumed to be straight, and Poiseuille's law can be applied. Also for this analysis, only the longer channel from the first three design versions is considered. According to Equation 10, pressure drop decreases with decreasing channel length, and since this analysis is meant to find the maximum amount of pressure applied to the channel, only the longer channel needs to be taken into account. Figure 15 shows the results of the theoretical analysis using Poiseuille's law for determining pressure drop vs. flow rate. The theoretical maximum pressure drop across the channel due to a volumetric flow rate of 5.5 $\frac{mL}{hr}$ is 1.44×10^4 $\frac{kg}{m \cdot sec^2}$ (2.08 psi).

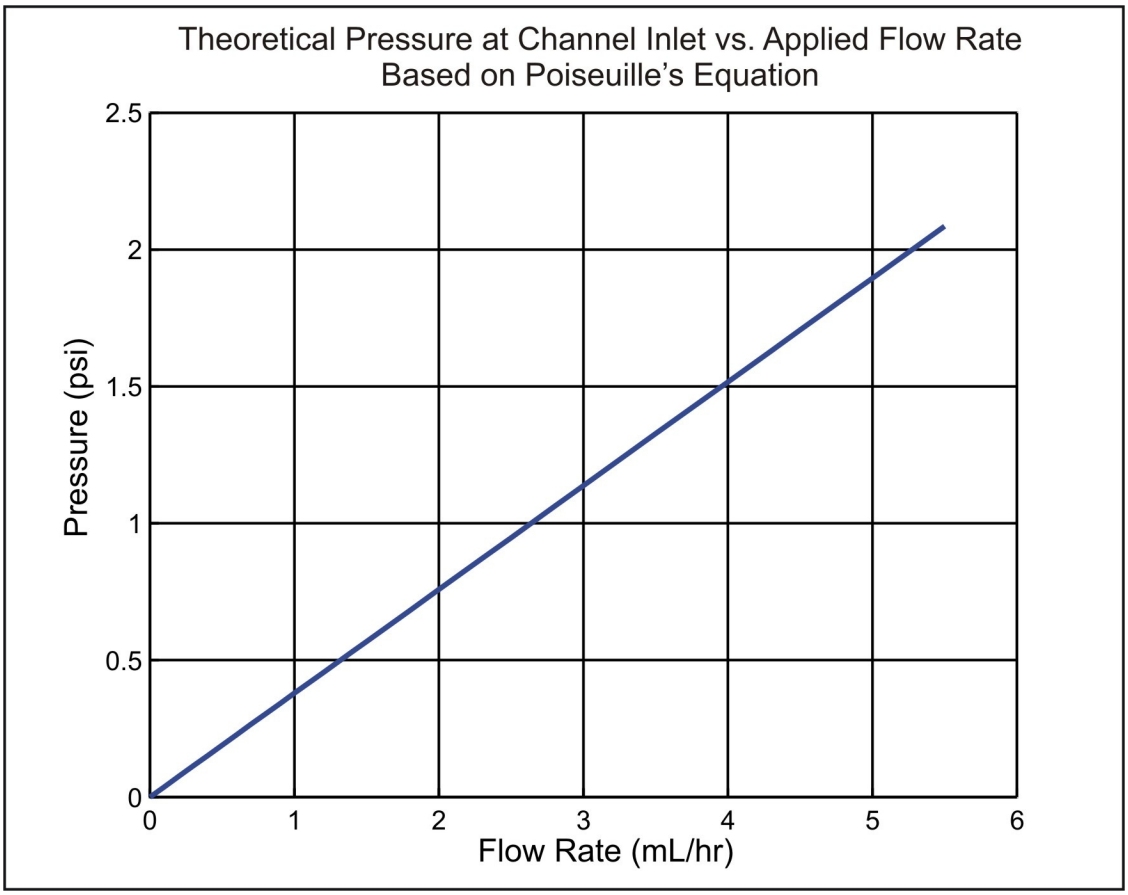

Figure 15: This plot of the pressure at the channel inlet due to an applied flow rate is determined from an analysis of Poiseuille's equation for laminar flow through a tube. The results show a linear increase in pressure due to increasing flow rates.

2.2.2 Equivalent Electrical Circuit of the Microsystem

The electrodes that interface the analysis cavities in the microfluidic system are used to perform impedance spectroscopy analysis on the material inside the cavities. The result of this analysis is displayed in a set of plots depicting the magnitude and phase of the impedance over a range of frequencies. An equivalent electrical circuit has been developed to model the expected impedance. The model includes all the components of the microfluidic system that can contribute to the measured impedance: the analyte and the carrier solution within the cavity, parasitics from the device, and the electrodes themselves. Figure 16 is a block diagram of the circuit used to model this system.

The first part of the circuit model is based on the parasitic effects that the device might have on the measured electrical signal. If a portion of the electrical signal between the two

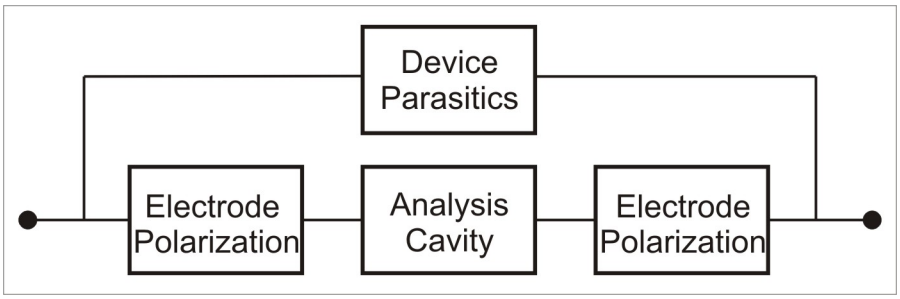

Figure 16: The circuit model for the microfluidic system can be divided into three different sections: (1) parasitic effects from the device itself, (2) polarization effects from both electrodes, and (3) a response due to the analyte inside the analysis cavity.

cavity electrodes travels through any part of the device besides the analysis cavity by means of the substrate material, then this additional pathway is the cause of the parasitic effects. For a single analysis cavity in the microfluidic system, the additional pathways are around the analysis cavity through the bottom cavity and top cavity layers and around the bottom of the analysis cavity through the via layer. The multiple pathways are combined and modeled by a simple RC parallel circuit in a shunt configuration to the main signal path. The R and C values are based on the resistivity (ρ) and dielectric constant (ϵ_r) specified for the main material of construction, Kapton® ($\rho = 1 \times 10^{15}$ Ω·m, $\epsilon_r = 3.5$), the dimensions of the analysis cavity (240 μm in diameter, 101.6 μm deep), and the thicknesses of each of the microsystem layers (50.8 μm thick) [35, 36]. These values are used in Equations 11 and 12, which lead to resistor and capacitor values of 1.4×10^{19} Ω and 2.3×10^{-15} F respectively. In these equations, ρ is resistivity [Ω·m], l is the length of the resistor [m], A_s is the cross-sectional area along the length of the resistor [m^2], ϵ_o is the permittivity of free space (8.85×10^{-12} $\frac{F}{m}$), ϵ_r is the dielectric constant [unitless], A_e is the cross-sectional area for the space between the plates of the capacitor [m^2], and d is the distance between the plates of the capacitor.

$$R = \frac{\rho l}{A_s} \tag{11}$$

$$C = \frac{\epsilon_o \epsilon_r A_e}{d} \tag{12}$$

The second part of the circuit model characterizes the metal electrodes. When an electrode is placed in an electrolytic solution (in a biological analysis the carrier solution

is typically an ionic solution), a double layer of charges will build up at the surface of the electrode, thus polarizing the electrode. This is shown in Figure 5 in Chapter 1 with regards to using reference electrodes in patch-clamping experiments. In this microfluidic system, the electrodes used for the impedance spectroscopy measurements are made of gold and are susceptible to electrode polarization. Therefore, the circuit model takes this into consideration with the addition of the two electrode polarization circuits, which are based on a Randles equivalent circuit [8]. The Randles equivalent circuit is comprised of a solution resistance (R_s) in series with the parallel combination of a double-layer capacitance (C_{dl}) and a charge transfer resistance (R_{ct}). The resistor and capacitor values are based on values found in the literature for gold electrodes in an electrolyte and on the cross-sectional area of the electrodes at the analysis cavity (30 μm^2): $R_s = 1 \times 10^4$ Ω, $C_{dl} = 1 \times 10^{-14}$ F, and $R_{ct} = 1 \times 10^5$ Ω [17, 66, 98].

The third part of the circuit model considers the analyte inside the analysis cavity. Again, this portion of the circuit is modeled by a simple RC parallel circuit, and Equations 11 and 12 are used to determine the resistor and capacitor values. Although the dimensions of the cavity remain constant, the resistor and capacitor values will change based on the characteristics of the material inside the analysis cavity. After device fabrication, the system is characterized by collecting impedance measurements with air, de-ionized (DI) water, and phosphate buffered saline (PBS), as is discussed later in Chapters 3 and 4. Therefore, these three materials have all been considered for the circuit model. The following resistivities, dielectric constants, and cavity dimensions have been used:

$\rho_{DIW} = 1.8 \times 10^5$ Ω·m,

$\rho_{PBS} = 0.2$ Ω·m,

$\epsilon_{r\_air} = 1.0006$,

$\epsilon_{r\_DIW} = 15$,

$\epsilon_{r\_PBS} = 81$,

$l_{cavity} = 2.5 \times 10^{-4}$ m, and

$A_{cavity} = 2.5 \times 10^{-8}$ m^2.

Figure 17 shows the three different circuit models used for air, DI water, and PBS.

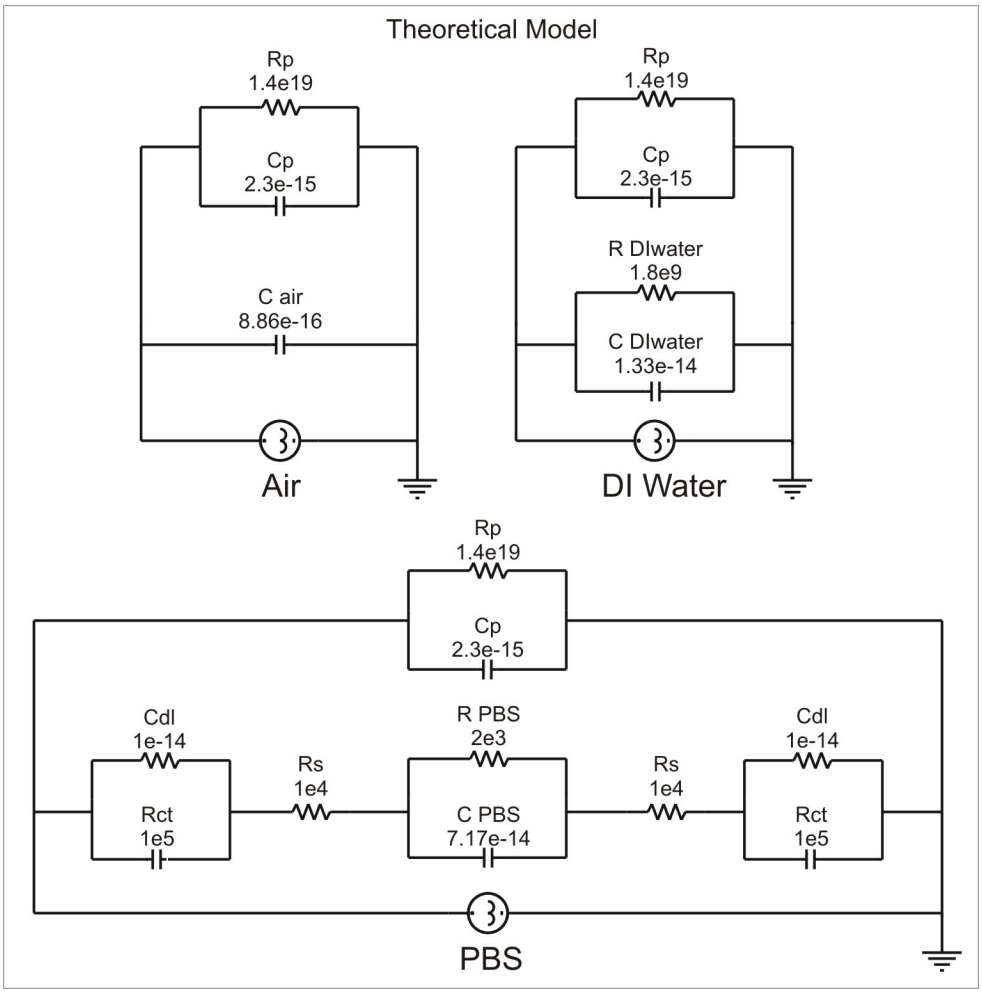

Figure 17: The circuit models for the microfluidic system with air, DI water, and PBS inside the analysis cavities are made up of a combination of RC circuits representing the device parasitics, electrode polarization effects, and the analyte itself. The polarization effects are not present for air or DI water.

For air, the RC circuit simplifies to a single capacitor. Since the electrode polarization only occurs for an electrode / electrolyte interface, this portion of the circuit model is not necessary for air or DI water; ideally, DI water does not contain free ions that would contribute to the charge build-up.

These circuit models were executed using the software OrCAD (Cadence Design Systems, San Jose, CA). The stimulus to the circuit was an AC current of 1 A, and the analysis was performed over a frequency range from 40 Hz to 10 MHz. Figure 18 shows the resulting magnitude and phase plots. It is noted that the magnitude drops from air to DI water to PBS. For DI water, the magnitude remains steady at low frequencies and starts to drop off

at 10 kHz, and the magnitude of PBS remains steady along the entire frequency spectrum. This is characteristic of the decreasing resistances and increasing capacitances from air to DI water to PBS. For the phase plots, air, which is purely capacitive, has a constant phase of $-90°$, and DI water and PBS have phase shifts at increasing frequencies again due to the differences in resistance and capacitance. These responses will be compared against the results from impedance measurements collected during device characterization as is discussed in subsequent chapters.

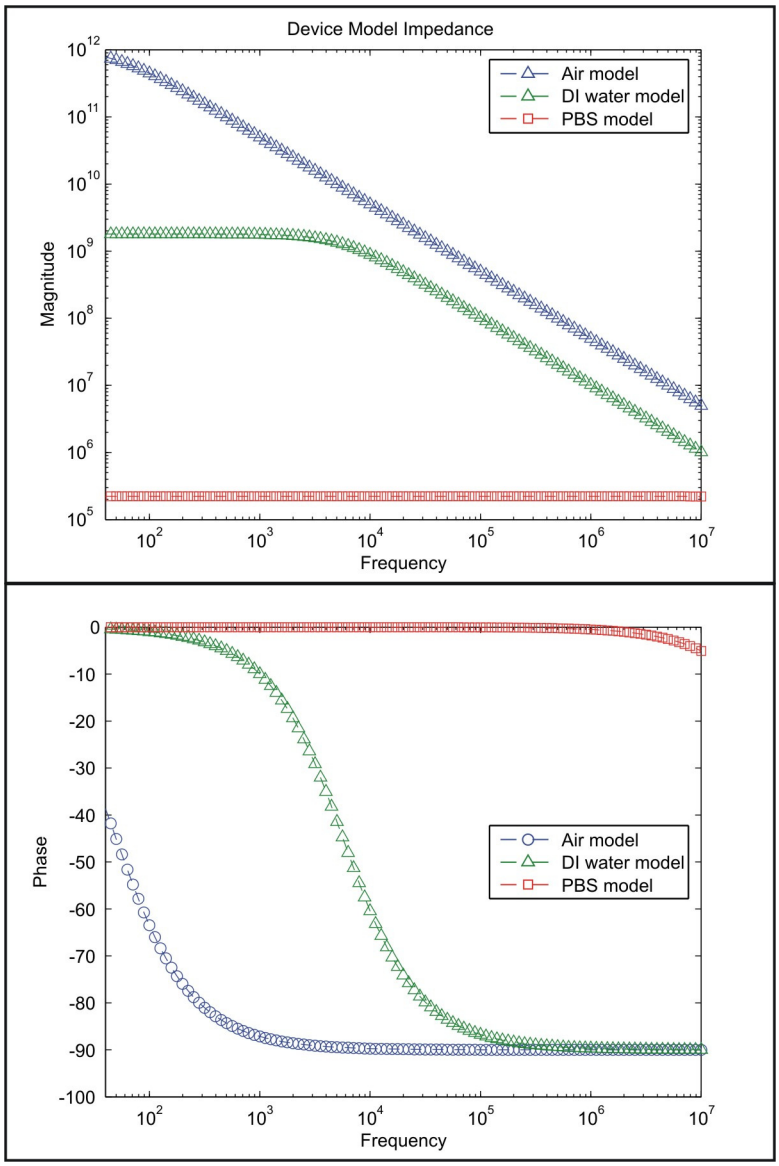

Figure 18: The impedance data (magnitude and phase) for the theoretical circuit model for air, DI water, and PBS in the analysis cavity over a frequency range of 40 Hz to 10 MHz show what trends are expected when experimental impedance data will be collected using the fabricated microfluidic systems.

CHAPTER III

MICROSYSTEM FABRICATION PROCEDURE

The initial step in fabricating a multi-layer microfluidic system is determining the appropriate material of construction. This is followed by, and sometimes in conjunction with, establishing the methods that will facilitate the patterning of the substrate material, including removal of material and the formation of electrodes in selected locations, and assembly of the individual layers. This chapter explains why Kapton® is the preferred substrate material and how laser ablation, microstenciling, and heat staking are used to fabricate a multi-layer microfluidic system.

3.1 Kapton as the Flexible Substrate Material

Characteristics that should be considered for the substrate material for a microfluidic device that is to be used for cellular analysis are biocompatibility, mechanical properties, and its compatibility with micromachining techniques. This microsystem is intended to be used only for cellular analysis experiments *in vitro*, and therefore, any type of immune response from a living host is not considered. However, the microsystem must still be biocompatible, meaning that it does not affect the extracellular fluid environment of the living cells. In terms of mechanical properties, the ideal material to use in a microsystem for biomedical applications would be durable such that it would not easily break during fabrication or during normal use in a final product.

Silicon (Si) and glass are readily used in conventional MEMS devices, and the procedures for processing them are well established [13,77]. Since they also exhibit biocompatible characteristics, Si and glass have become common materials to use in the fabrication of microsystems for biological analyses [3]. However, as a disadvantage, Si and glass are fragile and can easily break during fabrication and normal device use, and they require multiple processing steps for both patterning and assembly. In an attempt to ease fabrication and

introduce additional benefits, polymers are being incorporated into the design and fabrication of microsystems for biological analyses [69, 75]. Polymers are less fragile than Si and glass, and are therefore easier to process and handle in a final device without breaking. Some polymers are also biocompatible and transparent, and those that are photosensitive allow for simpler photolithographic processing [46].

Based on flexibility, biocompatibility, and the ability to process them using micromachining techniques, polymers that could be used for the microfluidic system include poly(dimethylsiloxane) (PDMS), poly(methyl methacrylate) (PMMA), parylene, polyethelene (PE), and various types of spin-on polyimides [34,60,71,86]. Another possible polymer, Kapton® (a commercially available polyimide made by DuPont), is already popular for use in electronic applications due to its electrical, thermal, mechanical, physical, and chemical stability over a wide temperature range. In fact, DuPont has combined its Kapton® product with an acrylic adhesive to form the product Pyralux, which is one of the common substrates used by flexible printed circuit manufacturers such as PFC Flexible Circuits Limited in Canada and All Flex Inc. in Minnesota. For its reliability in harsh environments, the flexible Pyralux substrates have been used for decades in the automotive and aerospace industries and now more frequently in the communications industry for cell phones and other small hand-held electronics. Although DuPont does not market Kapton® for biomedical applications, its biocompatibility has been verified through previous studies by Richardson et al., Cosofret et al. and Rousche et al. [26, 118, 123].

Outside of the electronic circuit board industry, the flexible yet durable characteristic of Kapton® has recently been noticed by researchers developing microsystems. Ramadoss et al. and Chang et al. have used Kapton® in fabricating MEMS based capacitive sensors and switches [18, 116]. In both cases, the Kapton® with patterned electrodes is the movable membrane. Some MEMS based biomedical applications have also investigated the use of Kapton® as the substrate for microelectrode arrays for stimulating and recording electrical signals from cardiomyocytes and neurons [1, 53, 90, 124, 141]. Li et al. used Kapton® as a compliant substrate for a silicon based pressure sensor that is designed to fit inside of a catheter for neonatal intravascular blood pressure measurements [83]. In this device, the

Kapton® substrate and the pressure sensor are bonded together using conductive polymers. Giordano et al. have also adapted a Kapton® substrate for their polymerase chain reaction (PCR) chip used in DNA amplification [52]. Kapton® was chosen for its high glass transition temperature and optical transmission in the IR range.

In addition to being flexible, microsystems made with Kapton® might also benefit from Kapton®'s thermal and optical characteristics. The ability to operate a microsystem over a wide temperature range is not a requirement for the types of cellular analysis performed as part of this research project, but it is a requirement of other biomedical applications. For example, polymerase chain reaction (PCR) uses temperature cycling between 35°C and 96°C for DNA amplification, and thermal field flow fractionation (TFFF) systems require integrated heaters at approximately 71°C, and both are applications currently being incorporated into microsystems [38, 76, 154]. Therefore, by using a material that is stable over a wide temperature range, other types of biomedical applications could be possible in polymer-based microfluidic systems. This is also an advantage if the microsystem were required to be used in harsh environments. Kapton® therefore provides some versatility to the microfluidic system since it is stable over a wide temperature range even greater than 350°C [35, 36].

As for the necessary optical properties of a microsystem, depending on the type of analyses and experiments a laboratory is conducting, the visual inspection could be performed with either an upright or inverted microscope that can be lit from the backside or the topside. Additionally, biomedical studies frequently use fluorescence to aid in analyzing their results. The transparent property of Kapton® allows for these various optical imaging techniques to be employed, and although other possible polymers are also transparent, a silicon-based microsystem would limit the options of the end user.

Of the possible polymers mentioned, Kapton® is the preferred substrate material for this multi-layer, microfluidic system; it is flexible yet durable, biocompatible, stable over a wide temperature range, transparent, and lends itself well to laser ablation and heat staking. The ability to pattern these sheets with laser ablation has been tested and confirmed as part of this research project, and the parameters for that process are described in a subsequent

section of this chapter. Forming metal electrodes on top of Kapton® sheets has been previously investigated by Graff et. al, and the procedures used for this project are described in a subsequent section of this chapter [56]. Several types of Kapton® are available and have different material properties (e.g. Young's modulus, coefficient of thermal expansion, and moisture uptake). For this research project, 50.8 μm thick sheets of Kapton® E and EKJ are used. The most important characteristic of these types of Kapton® that makes them ideal for the fabrication of a multi-layer microsystem is their ability to bond to each other. Kapton® EKJ sheets have a 3-layer composition: Kapton® KJ polyimide adhesive film on either side of a Kapton® E core. The Kapton® KJ adhesive film is not tacky, but bonds to neighboring material when placed under high temperature and pressure (350°C and 1.65 MPa). Thus, a stack combining Kapton® E and Kapton® EKJ enables the formation of a freestanding, multi-layer structure.

Besides Kapton® and other polymers that are available as a dry film, spin-on polymers can also be used to create multi-layer microsystems [46,59]. A spin-on polyimide is beneficial in that it can be prepared in a range of thicknesses by altering the spin speed. For this microfluidic system, the via layer requires feature sizes of approximately two to five microns in diameter, which can be easier to obtain in a substrate thinner than the 50.8 μm thick Kapton® sheets. Therefore, at the beginning of this research project, two types of spin-on polyimides, PI-2555 (HD Microsystems) and Photoneece PWDC-1000 (Dow Corning), were considered.

The polyimide PI-2555 can be patterned through either dry or wet etching techniques. The process flow for both methods is shown in Figure 19. For the dry etching method, the PI-2555 is spun onto a silicon (Si) wafer into a thickness of approximately 15 μm. A metal layer, titanium (Ti), is then deposited on top of the polyimide to act as a mask layer during the etching process. The Ti is patterned with photoresist, and then the exposed areas of Ti are etched in a diluted hydrofluoric acid (HF) solution. The sample is next placed in a reactive ion etch (RIE) in which an oxygen plasma is used to remove the exposed PI-2555. After etching, any remaining Ti is removed again in a diluted HF solution. The patterned layer of PI-2555 is then released in isopropyl alcohol (IPA). For the wet etching method,

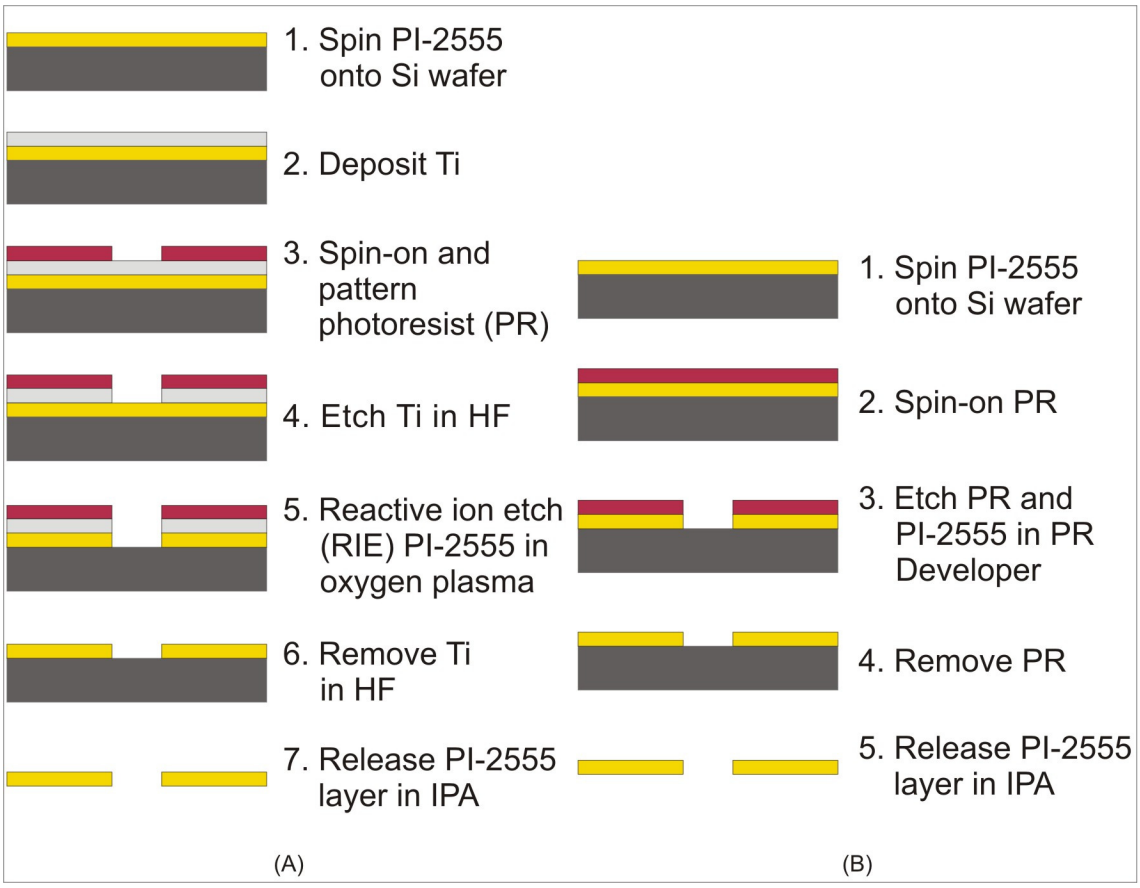

Figure 19: Thin layers for the microfluidic system can be made using the spin-on polyimide, PI-2555, which can be processed through either dry (A) or wet (B) etching techniques.

again the PI-2555 is spun onto a Si wafer into a thickness of approximately 15 μm. Next, photoresist, AZ-5214 (Clariant), is patterned on top of the polyimide to act as a mask during the etching process. During photoresist development, the sample remains in the developer (diluted MIF 312, Microchem Corp.) until the polyimide has been etched. The patterned layer of PI-2555 is then released in IPA with the aid of a razor blade.

The polyimide PWDC-1000 is a photosensitive polyimide and therefore can be patterned through typical photolithography techniques. The process flow for creating a patterned layer of PWDC-1000 is shown in Figure 20. First, a sacrificial metal layer (Ti) is deposited onto the Si wafer to act as a release layer at the end of processing. Then the PWDC-1000 is spun onto the Ti into a thickness of approximately 7 μm. Next, the polyimide is patterned directly without the use of a mask layer and developed in MF 319. Finally, the PWDC-1000 layer is release by etching the Ti in a diluted HF solution.

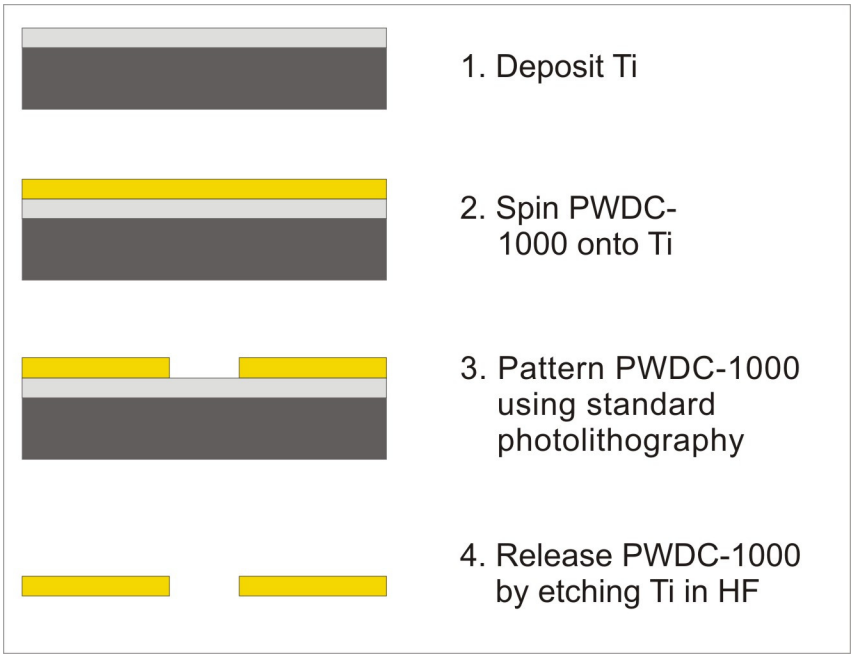

Figure 20: Thin layers for the microfluidic system can be made using the photosensitive spin-on polyimide, PWDC1000. This material can be patterned using standard photolithographic processes.

The results from processing both the PI-2555 and PWDC-1000 are discussed later in Chapter 3. However it can be said that using a material that is already in sheet form reduces the processing steps required for depositing, patterning, and releasing a spin-on polyimide and thus simplifies the entire procedure of creating a multi-layer microsystem. Therefore, so long as the small diameter via holes can be laser ablated into the 50.8 μm thick Kapton® sheets, the thin layers made possible by using a spin-on polyimide would no longer be necessary.

3.2 Metals Used for Electrodes

Besides the substrate material, the only other material used in this multi-layer microfluidic system is the metal for the cell cavity electrodes and the fluidic channel electrodes. First, the metals chosen must be appropriate for the application. And second, since the metal is deposited through typical MEMS techniques, as will be described later, the metal should be commonly found in MEMS fabrication. A common metal used in MEMS is gold, and since gold is biocompatible, it is also a common metal found in biomedical applications [12,13,79].

Therefore, gold is used for the cell cavity electrodes. The fluidic channel electrodes are meant to mimic the electrodes located in the glass micropipette in the conventional patch-clamp technique. As was described in Chapter 1, those electrodes are typically a silver (Ag) wire with a silver chloride (AgCl) coating. To mimic this aspect of the conventional patch-clamp technique, the fluidic channel electrodes are made with silver, which is another metal available through standard MEMS techniques. The silver chloride (AgCl) coating is applied to the Ag traces after they are patterned onto the Kapton® sheet through a microstencil as described in a subsequent section. To create the coating, a 5% HCl solution is applied to the ends of the Ag traces for 5 to 10 seconds, after which the sheet of Kapton® is rinsed in running DI water for approximately 30 seconds.

3.3 Microsystem Fabrication Procedures

Typical MEMS fabrication techniques for processing microsystems out of Si, glass, or even polymers include photolithography, wet and dry etching, and anodic or adhesive-based bonding of substrates [6,54,55,81]. Patterning materials through laser ablation and microstenciling and bonding substrates through heat staking to fabricate microsystems are not as common. Laser ablation of polymers has been performed in Kancharla et al. to create microchannels and filtration membranes [74]. In Graff et al., a microstenciling process for repeatable patterning of metal traces as narrow as 10 μm onto polymer substrates has been developed [56]. Using high temperature and pressure to bond polymer substrates has been investigated by Han et al. and Su et al. [60,138]. The results from these individual research efforts are promising and show that the integration of laser ablation, microstenciling, and heat staking could be used in place of traditional MEMS techniques for the fabrication of microfluidic systems for cellular analyses.

As is shown in Figure 21, the complete fabrication procedure for developing this multi-layer microfluidic system includes the following steps: patterning of features through laser ablation, deposition of appropriate metals for electrodes through microstenciling, assembly of the individual layers through heat staking, and packaging the system with appropriate electrical and fluidic interfaces. Each of these steps is described in detail in the following

sections.

3.3.1 Patterning Individual Layers with Laser Ablation

Each of the six layers in the multi-layer microsystem requires some features to be defined in the polyimide. These features include alignment holes, inlet / outlet ports, cell cavity openings, via holes, and fluidic channels and range from a few microns to a few millimeters in diameter. This patterning is accomplished through laser ablation with two different laser systems: an excimer laser system and a CO_2 laser system. The excimer laser system can provide a beam spot size from a few microns to hundreds of microns in diameter. The CO_2 laser system has a limited range of available beam spot sizes, but it is faster than the excimer laser, and is therefore beneficial for certain applications. Determining which laser is used for the multiple layers of the microfluidic system is discussed later as part of the results of the laser ablation in Chapter 4.

Ultraviolet (UV) laser ablation has been shown to be an efficient method for defining features in polyimide, including Kapton® [28, 39, 151]. The LPX200 series excimer laser (Lambda Physik) operates at a wavelength of 248 nm, which is within the UV range on the electromagnetic spectrum. This system uses krypton (Kr) / fluorine (F) as the rare / halide gas mixture and neon (Ne) as the buffer gas. The laser provides 20 ns pulse-lengths, operates at up to 100 Hz, and produces up to 600 mJ of energy per pulse. The laser is directed through a series of optics and interfaces with a computer-controlled stage (Micromaster large excimer laser workstation, Resonetics). Figure 22 shows a schematic diagram of the layout of the laser and the workstation. The laser has an initial beam spot size of 4 mm by 15 mm. In the workstation, the laser beam first travels through an attenuator, which can scale the energy from 5% to 98% of the original value. The beam is then projected through a metal mask with openings of varying diameters depending on the desired size of the feature to be ablated. The final stage of the workstation uses demagnification optics to focus the beam down to 4 - 14 times the projected size. Based on user inputs, a computer running the laser software, Lightdeck (Resonetics), controls the energy and pulse rate of the original laser beam and interfaces with the workstation directly to control the attenuation,

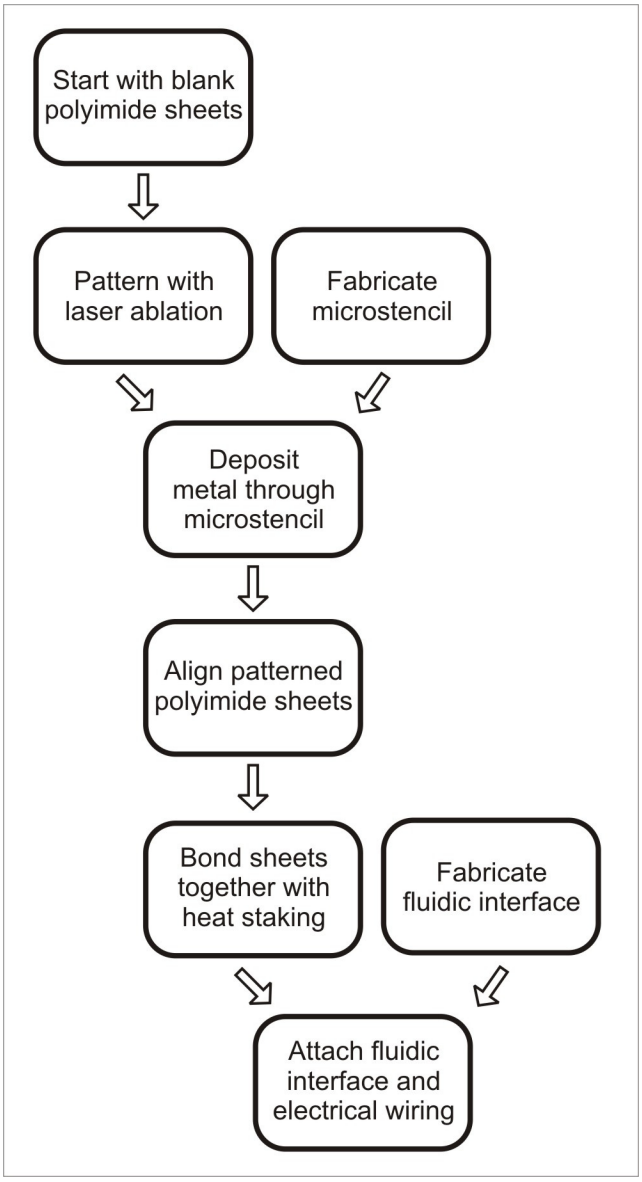

Figure 21: The fabrication procedure for the multi-layer, microfluidic system begins with selecting the substrate material. This is followed by patterning the material through laser ablation and microstenciling. After the multiple layers are bonded together, the final step of the fabrication is packaging.

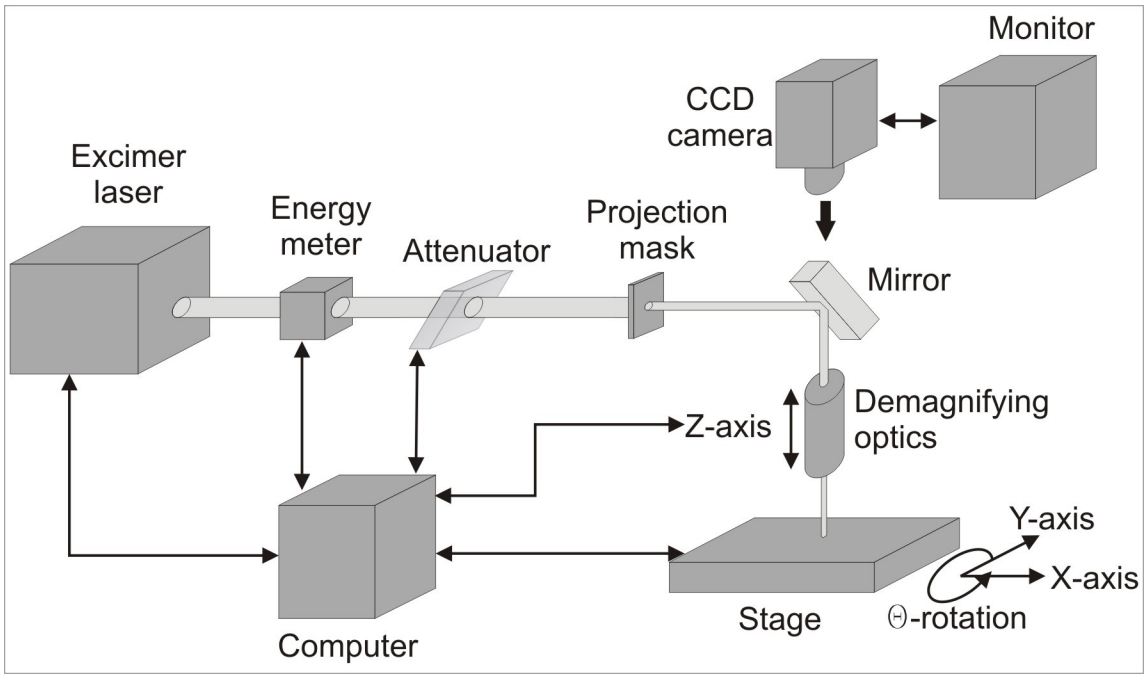

Figure 22: The excimer laser beam travels through an attenuator, projection mask, and de-magnification optics before reaching the movable stage. The laser parameters and stage are controlled through a computer and the projection mask is positioned by hand. A CCD camera and monitor aid in observing the process.

demagnification, and focus of the beam. The computer also controls the x-y position and rotation of the stage that holds the material to be ablated. The metal projection mask, located between the attenuator and demagnification optics, is positioned into the path of the laser by hand.

To ablate specific patterns into a sheet of Kapton® located on the stage of the workstation, the stage must be moved according to the location of those patterns. The laser software bases the movement of that stage on two types of input files as well as user defined parameters. The first type of file is a tab-delineated ascii file (.txt) that simply provides a list of x-y coordinates where single holes are to be ablated. The second type of file is used to move the stage in circles and straight lines and is based on an AutoCAD (Autodesk Inc.) drawing file (.dwg). Before the .dwg file can be used by the laser software, it is first converted into a .dxf file through AutoCAD. Then using the laser software, the .dxf and .txt files are combined with user inputs such as operating frequency and number of pulses to create .oms files. The information in the .oms files tells the workstation when and where to

move the stage, how fast to move it, and when and for how many pulses to fire the laser. By running multiple .oms files with different sized metal projection masks, features of various sizes can be defined on a single substrate.

The LS500XL series CO_2 laser (Gravograph) operates at a wavelength of 10.6 μm. While this type of laser is typically used for industrial applications such as welding, heat treatment, drilling, and engraving, it is also suitable for patterning polymers [28, 70]. This laser system is simpler than the excimer laser system with fewer user defined parameters. The laser beam is not attenuated, limited by a projection mask, or demagnified. Rather, it is sent directly through a focusing lens and onto a metal stage where the target material is located. The focusing lens determines the beam spot size. The available lenses have focal lengths of 2 inches, 2.5 inches, 3.5 inches, and 4 inches, from which the minimum beam spot size available is a constant 160 μm with the 2 inch focal length lens. Also, unlike the excimer laser system, the CO_2 laser beam is moved over the material rather than the stage moving. A diagram showing the layout of the laser is shown in Figure 23. The CO_2 laser movement and firing is controlled through a computer running the laser software, LaserStyle (Gravograph). An AutoCAD drawing (.dwg), similar to that used with the excimer laser, is made and converted into a .dxf file. This file in imported into the laser software. Within this software, the user can define only a few parameters. The power level can be set to 10-100% of 60 watts, and the speed of the moving laser beam can be set to 1-100% of 200 $\frac{mm}{sec}$. The laser software uses this information to control the movement and firing of the CO_2 laser.

When ablating with either laser system, first a sheet of Kapton® is pre-cut into an appropriate size for the layer of the microsystem that will be processed. That sheet is taped down onto an aluminum block, which is then placed onto the laser stage. Next, the focus is adjusted by moving the optics of the excimer laser or the stage of the CO_2 laser. The final step before running the laser is to set the x-y coordinates accordingly such that the pattern will be ablated in the correct location on the Kapton® sheet.

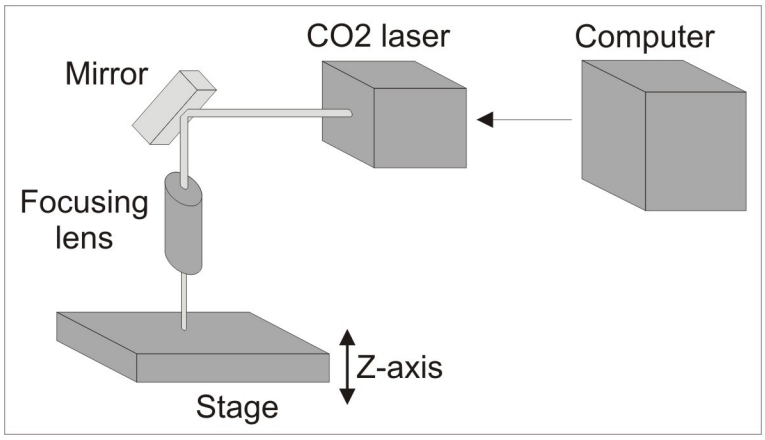

Figure 23: The CO_2 laser is simpler than the excimer laser. It only travels through a single focusing lens before reaching the stationary stage. The firing and movement of the laser is controlled through a computer.

3.3.2 Electrode Formation Through Microstenciling

The microfluidic system contains two metal layers. The first metal layer forms the electrodes located at the bottom of the fluidic channel, and the second metal layer forms the electrodes that interface at the sides of the analysis cavities. Both metal layers are directly patterned onto the surface of the Kapton® sheets through a microstenciling technique. Microstenciling enables patterning of vapor-deposited films and sputtered thin metal films onto materials (e.g. thermoplastics, metal oxides) incompatible with standard photoresist processing by eliminating any photolithography and wet micromachining processes that would be directly applied to those materials [56]. In addition, microstencils are reusable, and therefore simplify the batch fabrication of these microfluidic systems.

The microstenciling technique begins with a silicon wafer that is through-wafer etched using inductively coupled plasma (ICP) etching. The etched pattern in the silicon microstencil defines the areas through which the thin metal films are to be deposited onto an underlying substrate. After defining the through-wafer pattern in the silicon wafer, the microstencil is mounted on top of and in contact with a substrate, i.e. the Kapton® sheet. Subsequently, the thin metal films are deposited through the microstencil and onto the substrate. After metal deposition, the microstencil is lifted off of the substrate, leaving behind the metal pattern, Figure 24. This procedure has been shown to produce repeatable

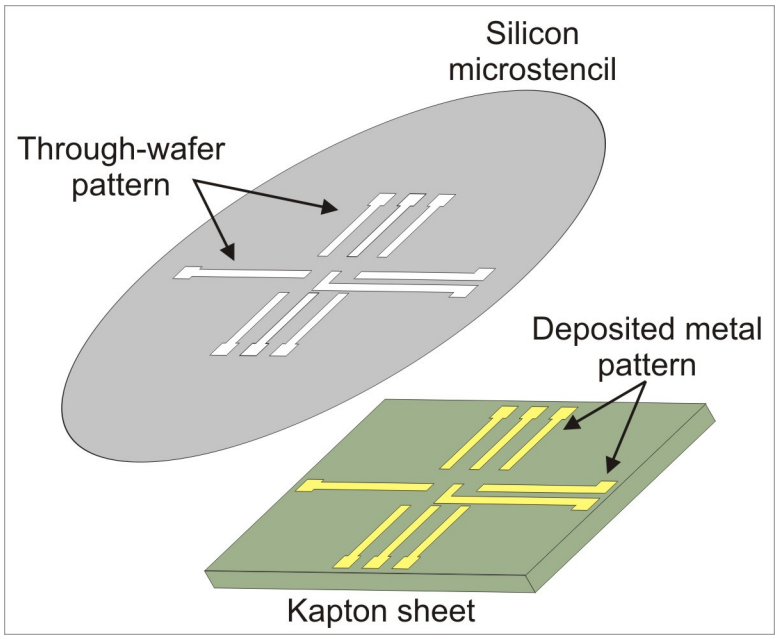

Figure 24: Microstenciling enables patterning of thin metal films onto substrates not necessarily compatible with standard photolithographic processes. The technique involves making a silicon stencil and using it to mask the substrate material during either evaporated or sputtered metal deposition.

metal patterns as small as 5 μm with high quality adhesion between the deposited metal and polyimide substrates [56, 99].

The fluidic channel electrodes are 100 μm wide along their entire length and terminate at 500 μm wide contact pads. The microstencil for the fluidic channel electrodes is made with a 450 μm thick, 4 inch Si wafer. Figure 25 shows an AutoCAD image of the layout of the fluidic channel electrodes along with the cell cavity arrays. This single microstencil is used to pattern the fluidic channel electrodes for four separate microfluidic systems at a time, one in each quadrant of the Si wafer. A processing diagram for creating the microstencil and depositing the metal is shown in Figure 26. First, NR9-8000 negative photoresist (Futurrex, Inc.) is spun onto the wafer at 700 RPM for 30 seconds, which results in a 25-30 μm thick layer of photoresist. The photoresist is then defined using a light-field mask containing the pattern for the fluidic channel electrodes. The photoresist is exposed to UV radiation on an Optical Associates Inc. Mask Aligner at a dose of 600 $\frac{mJ}{cm^2}$ and then developed in RD6 (Futurrex, Inc.) for 120 seconds. Next, the wafer is placed in a Plasma-Therm ICP reactive ion etch (RIE) and etched using the Bosch process. The Bosch process outlines a

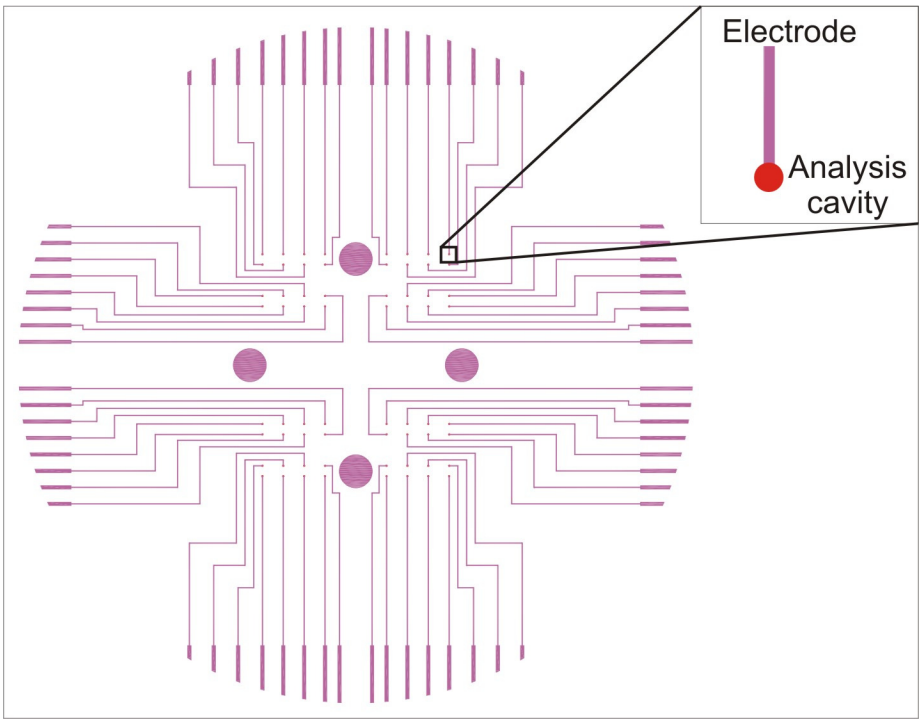

Figure 25: The features for the fluidic channel electrode microstencil span the area of a 4 inch silicon wafer. This microstencil can be used to pattern the metal traces onto four separate microfluidic systems at one time. The traces are 100 μm wide along their entire length and terminate at 500 μm wide contact pads. The four large circles are used for alignment of the microstencil to the substrate. Inset: A close-up of the end of a single trace showing how it would be aligned to the overlaying analysis cavity.

repeated series of steps in which a Si wafer is etched and then a material is deposited onto the sidewalls to reduce undercutting of the Si [80]. This process is used to obtain straight sidewalls when performing deep RIE (DRIE), as is the case for creating a microstencil.

Once the pattern is completely etched through the Si wafer, the microstencil is mounted resist-side down on top of the Kapton® sheet. By mounting the microstencil resist-side down, sharper edges in the deposited metal are obtained. The apparatus for holding the microstencil and the Kapton® sheet together during metal deposition is shown in Figure 27. To maintain alignment during metal deposition, 4.7625 mm pins are placed through both the microstencil and the Kapton® sheet and into the holder. A large, flat metal ring is placed on top of the microstencil and Kapton® sheet to help hold the microstencil in contact with the Kapton®. The holder is then placed into a CVC DC sputterer for metal deposition. First 600 $\dot{A}$ of Cr is deposited. Then 600 $\dot{A}$ of Pt is deposited on top of the Cr layer. This is

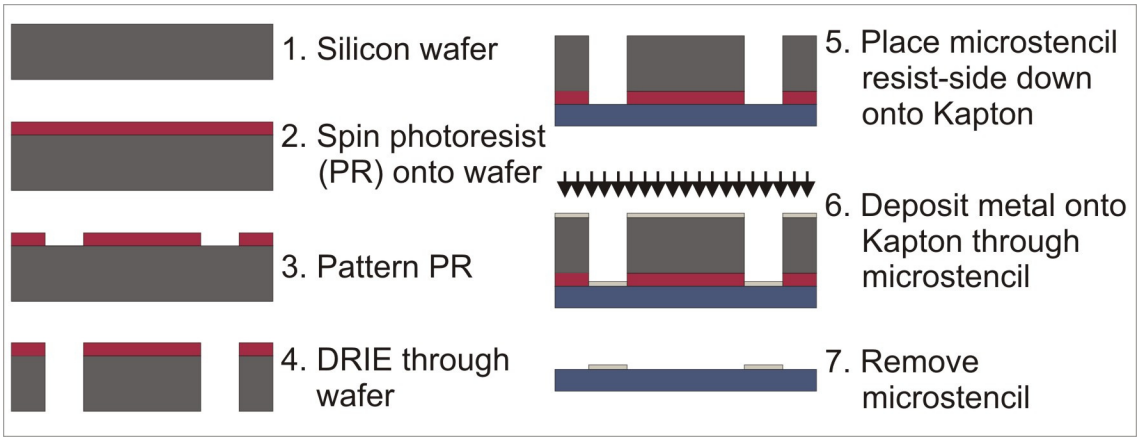

Figure 26: The fluidic channel electrode microstencil is processed on only one side of the silicon wafer. The features are etched completely through the wafer using the BOSCH process. During metal deposition, the microstencil is mounted resist-side down on top of the substrate to achieve sharper edges in the patterns.

then followed by the deposition of 2000 $\dot{A}$ of Ag. After metal deposition, the microstencil is removed, and the metal traces remain on the Kapton® sheet. The microstencil can then be used again to pattern the fluidic channel electrodes onto additional sheets of Kapton®. At this point, the silver chloride (AgCl) coating is applied to the Ag traces using the process described earlier in this chapter.

The electrodes that interface the analysis cavities have smaller dimensions in some areas than the fluidic channel electrodes. For some of the analysis cavities, two electrodes interface at the sides of the cavity, while four electrodes are present at other cavities. For the two-electrode design, the metal electrodes are 8 μm wide at the analysis cavity and then expand to 100 μm wide. For the four-electrode design, an additional stepping size is required to be able to place more traces around the perimeter of the cell cavity without shorting the traces together. These traces are also 8 μm wide at the analysis cavity but then step up to 20 μm wide and then to 100 μm wide. All the cavity electrodes terminate at 500 μm wide contact pads. Figure 28 shows two AutoCAD images. The first image is for the first version of the microfluidic system with 16 analysis cavities, and the second is for the second, third, and fourth versions of the system with eight analysis cavities. The figure also contains a close-up of the four- and two-electrode design. As with the fluidic channel microstencil, this single microstencil is used to pattern the cavity electrodes for four separate microfluidic systems at

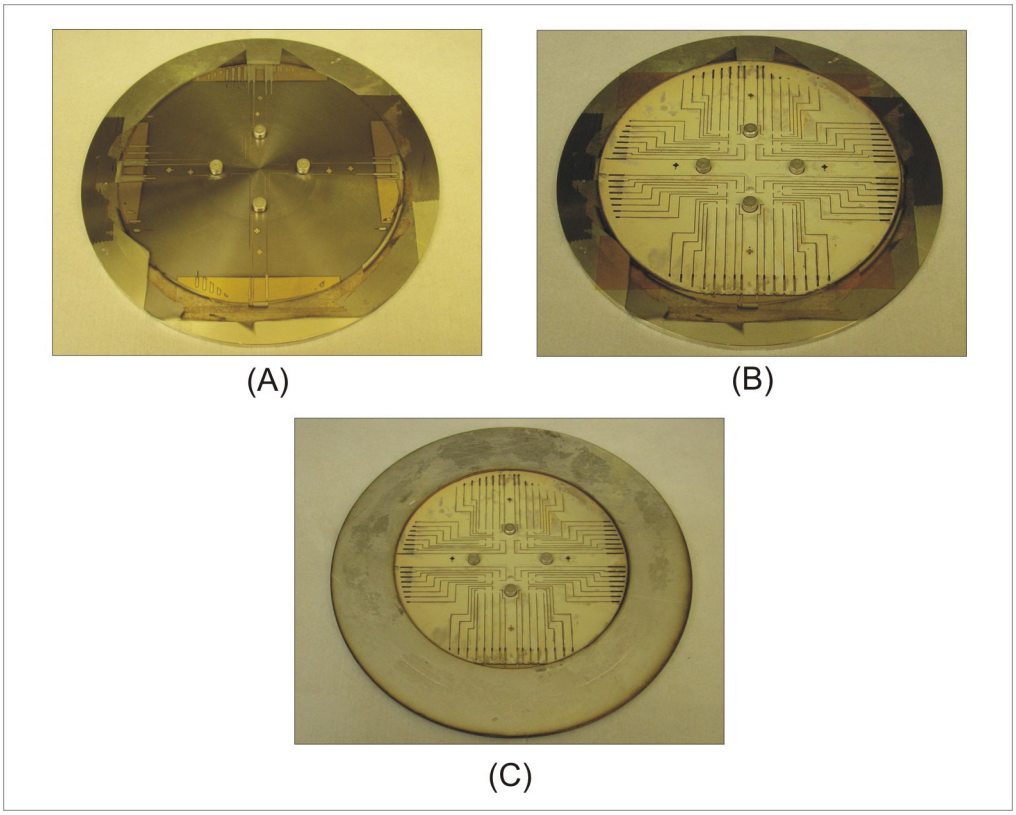

Figure 27: (A) The base plate contains four holes the same size as the large alignment features. (B) The substrate material is placed onto the base plate and the microstencil is placed on top. The four alignment pins are fit into the holes in the stencil, the substrate, and the base plate. (C) A metal ring in positioned on top of the stack to keep the microstencil in contact with the substrate and to cover any exposed edges of the substrate.

a time, one in each quadrant of the Si wafer. Since the cavity electrode microstencil contains smaller features than the fluidic channel electrode microstencil, a different approach to the processing of the microstencil is required. The cavity electrode microstencil is made with a 350 μm thick 3 inch Si wafer. An 8 μm wide trench in a 350 μm thick wafer results in an aspect ratio greater than 40:1. A feature with this aspect ratio is difficult to produce even with the Bosch process. To reduce this aspect ratio without having to use a thinner Si wafer, small areas that correspond to the location of only the 8 μm and 20 μm wide features on the topside of the Si wafer are thinned by etching in those areas from the backside of the wafer first.

A processing diagram for creating the cell cavity electrode microstencil by using both topside and backside processing and depositing the metal is shown in Figure 29. First, a 2.5 μm thick layer of silicon dioxide (SiO_2) is deposited onto the topside of the Si wafer in a Unaxis plasma enhanced chemical vapor depositor (PECVD). Next, NR4-8000 negative photoresist (Futurrex, Inc.) is spun onto the backside of the Si wafer at 2500 RPM for 5 seconds, which results in a 20 μm thick layer of photoresist. The photoresist is then defined using a light-field mask containing small rectangles. The photoresist is exposed to UV radiation on an MA-6 Mask Aligner (Karl Suss) at a dose of 1080 $\frac{mJ}{cm^2}$ and then developed in RD6 for 165 seconds. The positions of the rectangles correspond to the locations of the 8 μm and 20 μm wide features that are to be patterned on the topside of the Si wafer. Figure 30 is an AutoCAD image that shows the placement of these rectangles with respect to the cell cavity electrodes for a four-electrode and a two-electrode configuration portion of the microstencil. The wafer is next placed in a Plasma-Therm ICP RIE and etched using the Bosch process. Approximately 270 μm of the 350 μm thick Si wafer is etched through in the rectangles defined by the photoresist. Then, the NR4-8000 is removed in acetone, and the topside of the wafer is patterned. NR4-8000 is spun onto the topside of the Si wafer at 3000 RPM for 40 seconds, which results in an 8 μm thick layer of photoresist. The photoresist for the topside of the wafer does not have to be as thick as that used on the backside of the wafer since the SiO_2 layer will act as the silicon etch mask as opposed to the photoresist. The cell cavity electrode pattern is defined on the topside of the wafer using a

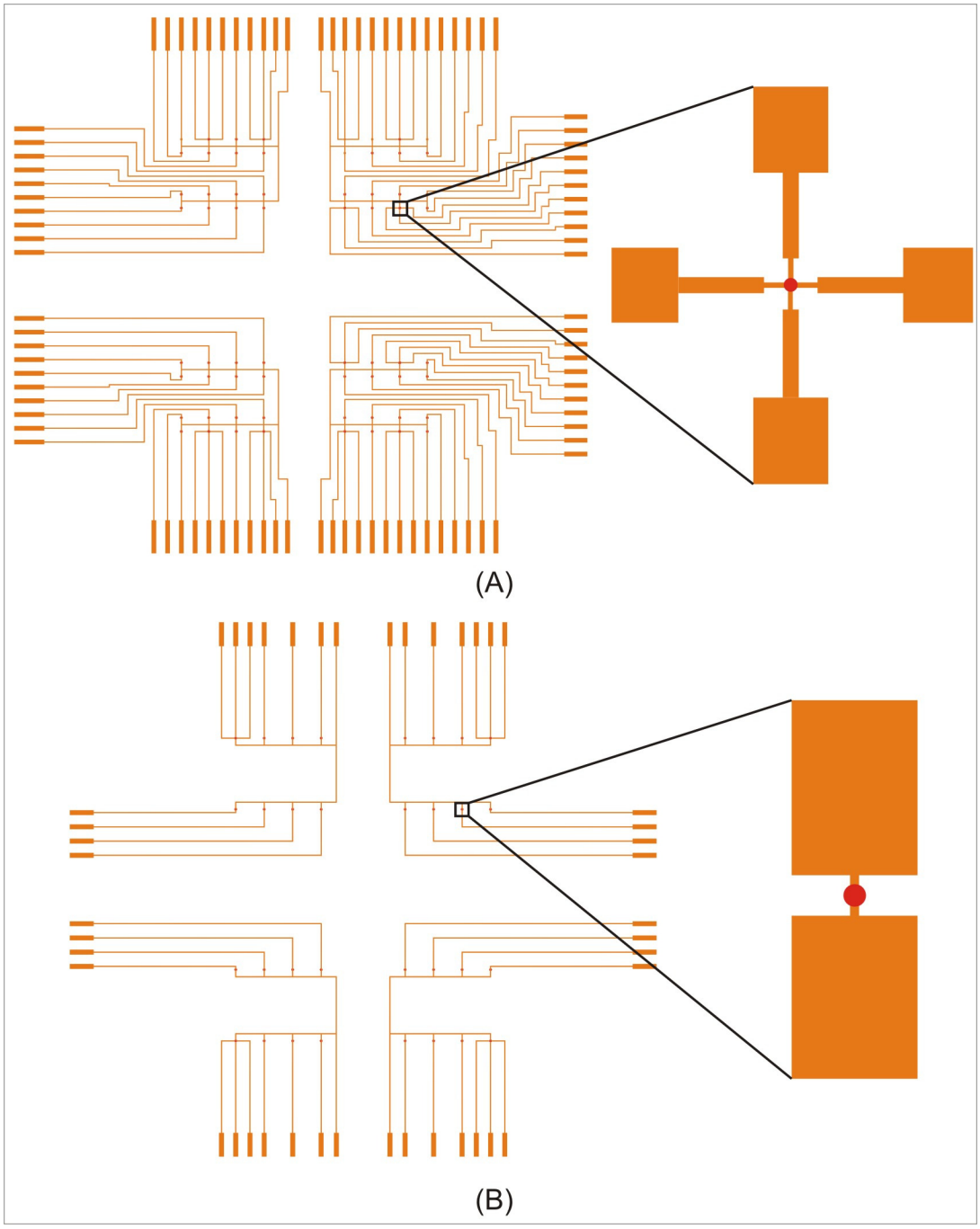

Figure 28: The features for the cavity electrode microstencil span the area of a 3 inch silicon wafer. This microstencil can be used to pattern the metal traces onto four separate microfluidic systems at one time. The traces are 8 μm wide, 20 μm wide, and 100 μm wide at various stages along their length and terminate at 500 μm wide contact pads. Each analysis cavity interfaces with either two or four electrodes. (A) The first version of the microfluidic system has 16 analysis cavities for each device. Inset: A close-up of the location around a single analysis cavity with four electrodes. (B) Versions 2, 3, and 4 of the microfluidic system have 8 analysis cavities. Inset: A close-up of the location around a single analysis cavity with two electrodes.

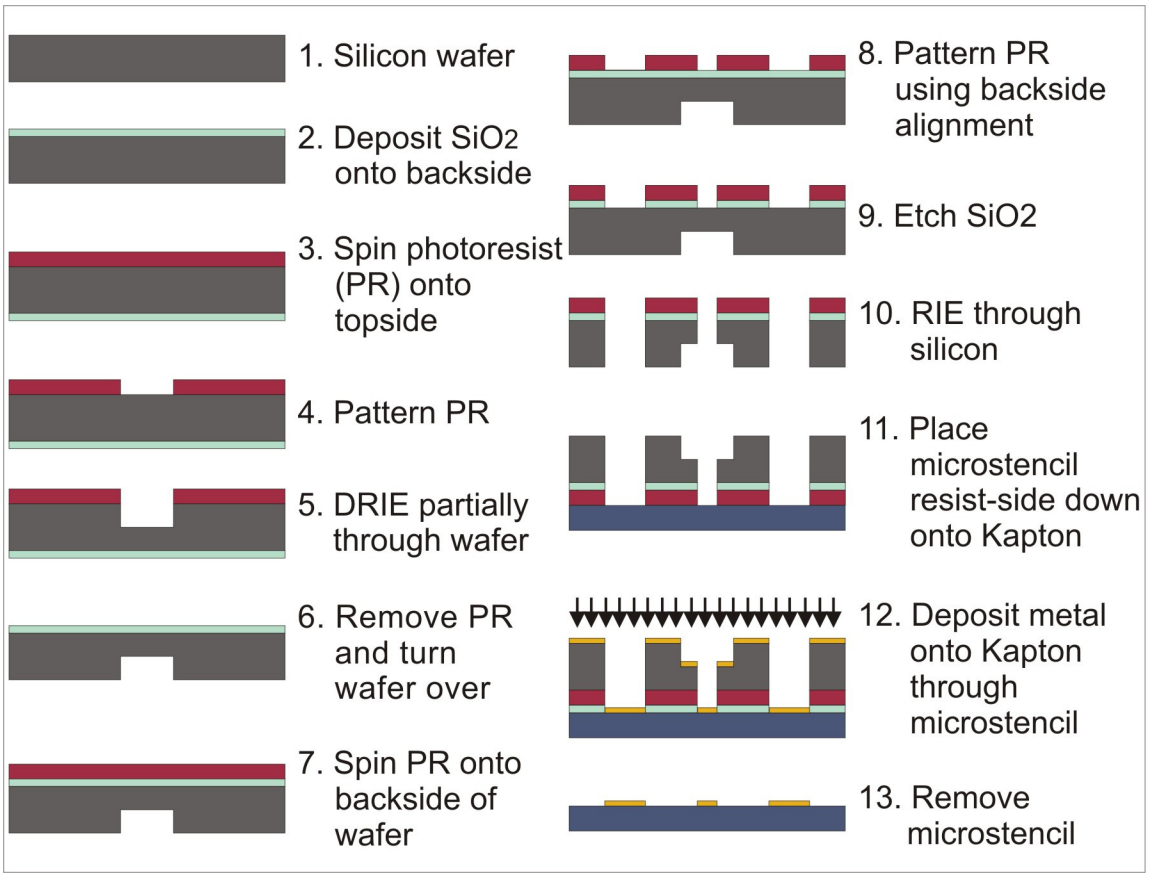

Figure 29: The cavity electrode microstencil goes through both topside and backside processing to achieve high aspect ratio features (greater than 40:1). The BOSCH process is used to obtain straight sidewalls during etching. During metal deposition, the microstencil is mounted resist-side down on top of the substrate to achieve sharper edges in the patterns.

light-field mask by using backside alignment of the electrode pattern to the rectangle pattern previously etched into the backside of the wafer. The backside alignment and photoresist exposure to UV radiation is performed in a MA-6 Mask Aligner at a dose of 168 $\frac{mJ}{cm^2}$. The photoresist is then developed in RD6 for 120 seconds. The wafer is again placed in a Plasma-Therm ICP RIE, and first the 2.5 μm thick layer of SiO_2 is etched through using an oxygen plasma. Then the cell cavity electrode pattern is completely etched through the Si wafer using the Bosch process.

Once etching is complete, the microstencil is mounted resist-side down on top of the Kapton® sheet. The microstencil and the Kapton® must be aligned such that the electrodes will accurately meet up to the analysis cavities. To perform this alignment, the microstencil is placed in a holder as shown in Figure 31. The holder contains a recessed

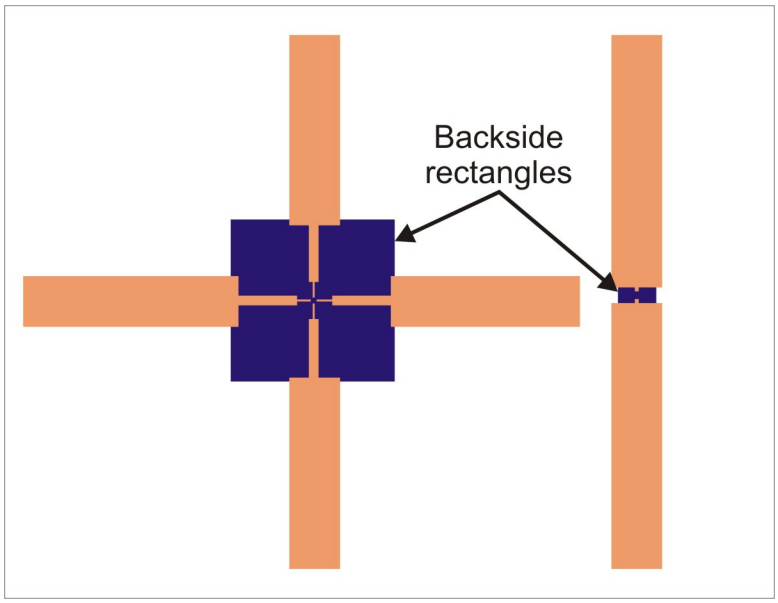

Figure 30: The rectangles patterned onto the backside of the wafer and etched part way through the silicon are positioned such that they are aligned with the smaller features to be patterned on the topside of the wafer.

grove for the microstencil such that the sheet of Kapton® can be placed on top and be held flush to both the holder and the microstencil. The Kapton® is taped to a glass plate and placed on top of the microstencil. With the aid of a microscope, the glass plate is moved around until the analysis cavities patterned into the Kapton® sheet are aligned to the microstencil. The glass plate and holder are then clipped together using two medium-sized binder clips. The entire apparatus is then placed into a CVC E-beam evaporator such that the microstencil remains facing down. Evaporation, as opposed to sputtering, is a directional metal deposition technique and is required to produce the small metal traces for the cavity electrodes. First, 1000 $\dot{A}$ of titanium (Ti) is evaporated. The Ti acts as an adhesion promoter between the Kapton® and the Au. Then, 2000 $\dot{A}$ of Au is evaporated. After metal deposition, the Kapton® is moved off of the microstencil, and the metal traces remain on the Kapton® sheet. The microstencil can now be used again to pattern the cavity electrodes onto additional sheets of Kapton®.

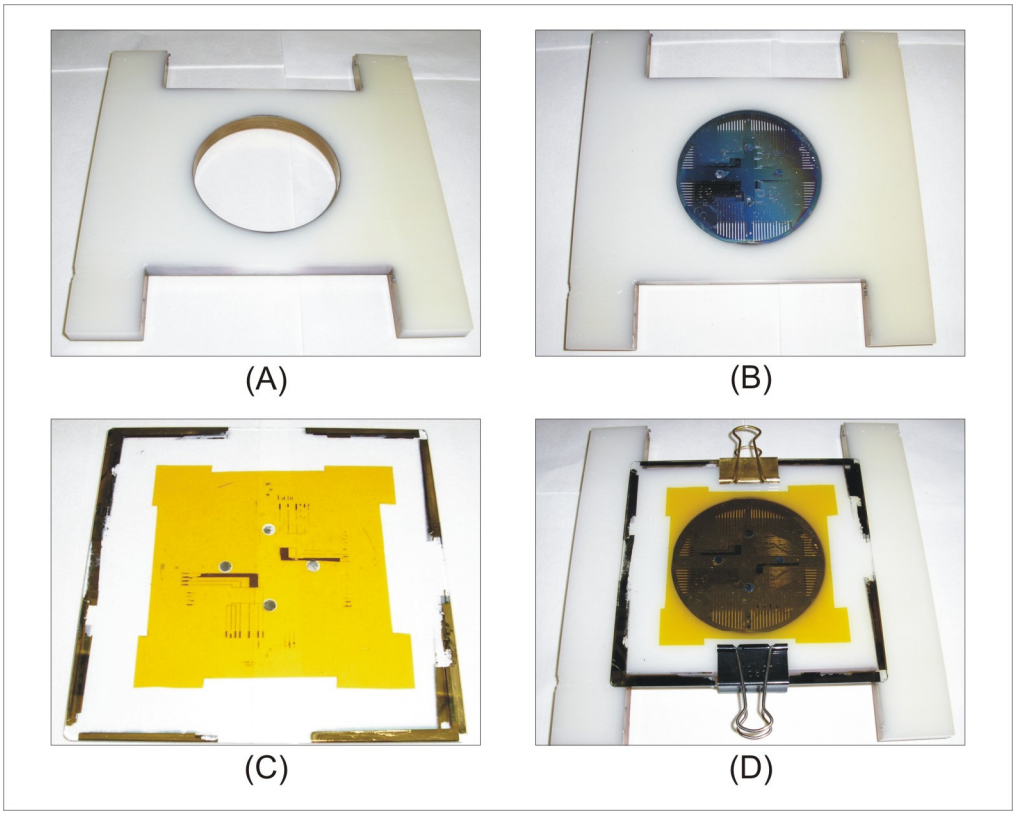

Figure 31: (A) The base structure is a molded polymer. (B) It contains a recessed grove for the microstencil. (C) The substrate is taped down to a glass plate. (D) The glass plate is turned upside down so that the side with the substrate on it is held against the microstencil. The patterned substrate is hand-aligned to the features in the microstencil using a microscope. Once aligned, the glass plate and base structure are clipped together.

3.3.3 Alignment and Heat Staking of Individual Layers

Once all the Kapton® layers for the microfluidic system have been patterned through laser ablation and microstenciling, they are aligned and bonded together. The alignment is performed using the large and small alignment holes that are patterned during laser ablation. The types and number of alignment holes used varies based on which version of the microfluidic system is being fabricated. Figure 32 shows the placement of those holes on one of the laser ablated sheets of Kapton® that would be used for versions three and four of the microfluidic system. This sheet is patterned for four separate devices, one in each quadrant. The large alignment holes are 4.7625 mm in diameter, which corresponds to the diameter of a $\frac{3}{16}$ inch metal post. The metal posts are used to position the Kapton® sheets in the overall correct location relative to one another; however, the precision in their diameters is not sufficient for complete alignment of all the features in the microfluidic system. To achieve greater precision, the small alignment holes, 242.2 μm in diameter, are used. Fiber optic strands, specified at 240 μm in diameter with a standard deviation of ± 0.52 μm, are threaded through the small alignment holes on each of the six Kapton® layers. The alignment is performed on a stainless steel plate, Figure 33, which contains holes for all the alignment posts and is used during the heat staking process. The plate is designed to hold four separate microfluidic systems at one time, one in each quadrant.

The alignment process begins by cleaning all the layers of Kapton® in an ultrasonic bath (Boekel Scientific Inc.). This removes any residue from the laser ablation process. The layers are then dried with nitrogen. The base layer of the microfluidic system is placed on the stainless steel plate, and all the alignment posts are threaded through their corresponding holes. Each subsequent layer is then positioned on top of the stack by lining up the alignment holes and posts and pushing the Kapton® layer down until it is flush with the previous layer. Alignment is verified after each layer is added by visual inspection using a microscope. In versions one and two of the microfluidic system, when only the large alignment features are used, additional adjustments are made to each layer by hand to aid in alignment. When alignment of a particular layer is deemed sufficient, a small piece of Kapton® tape (DuPont) is applied to keep it in place. In versions three and four of the

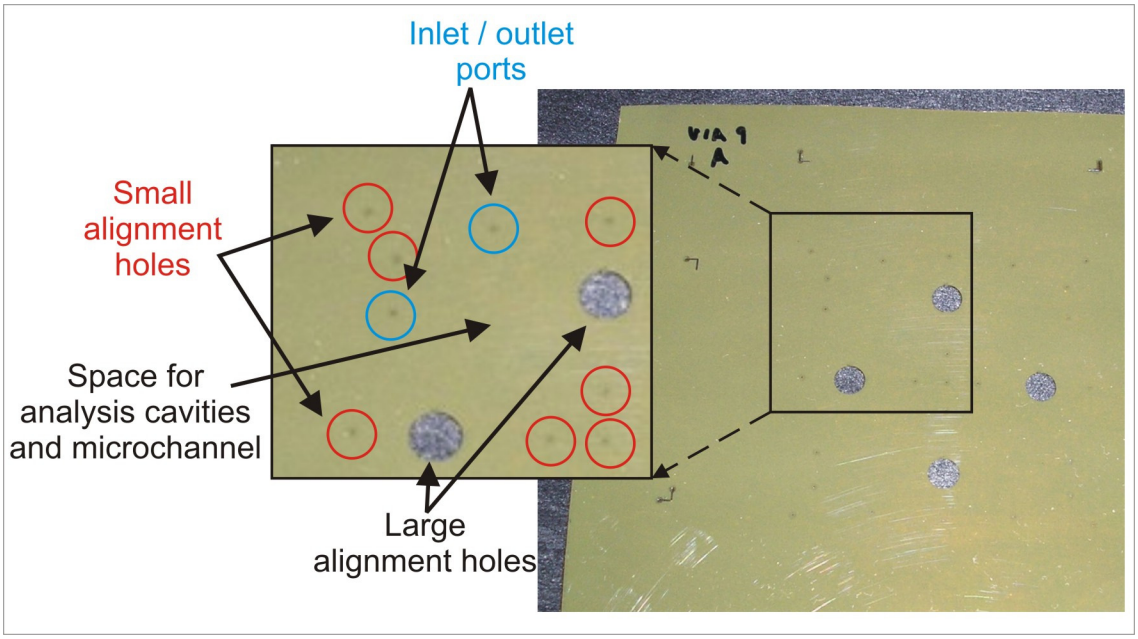

Figure 32: For a single microfluidic system, seven small alignment holes and two large alignment holes are laser ablated into each layer of Kapton®.

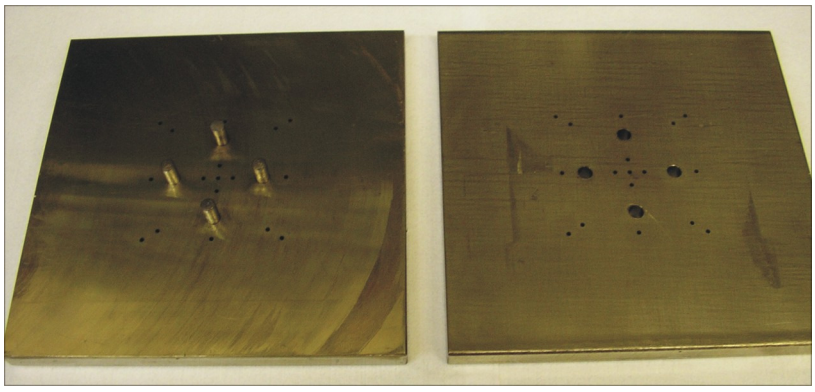

Figure 33: The plates used for aligning and heat staking the multiple layers of the microfluidic system contain holes for the large and small alignment pins. The plates are designed to hold four separate microfluidic systems at one time, one in each quadrant.

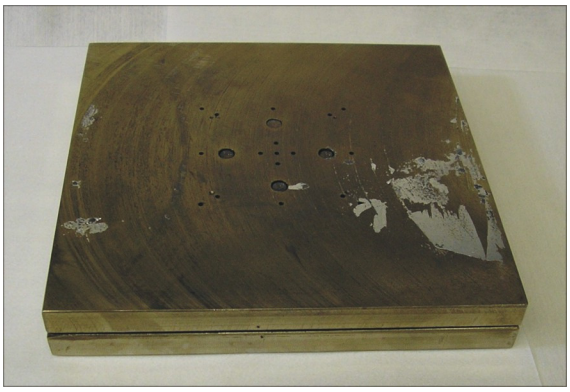

Figure 34: After all the individual layers have been aligned, the top plate is positioned on top using the large alignment holes and pins as guides.

Figure 35: The heat press is run at 350°C for 60 minutes in a vacuum sealed chamber at an applied pressure of 1.65 MPa.

microfluidic system, when both large and small alignment features are used, no additional adjustments by hand are made nor is any Kapton® tape used.

After alignment of the entire stack is verified, another stainless steel plate, with corresponding alignment holes, is situated on top of the first plate, Figure 34. Each plate is 5 inches square and 0.375 inches thick. The inside faces of each plate are polished to a surface roughness of 4 μm to ensure that bonding occurs evenly over the entire microfluidic system. The plates are then placed in a compression molding press (Vantage Series, Wabash MPI.), Figure 35, and 1.65 MPa of pressure is applied at a temperature of 350°C for 60 minutes. The heat staking process is run in a vacuum sealed chamber to reduce the formation of voids between the Kapton® layers.

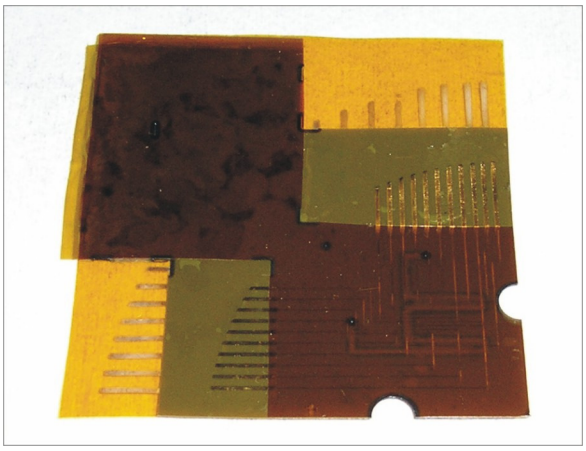

Figure 36: After heat staking, the six Kapton® layers now form a freestanding, multi-layer structure, which can now be packaged.

3.3.4 Packaging of Fluidic and Electrical Connections

After the heat staking process, the six Kapton® layers now form a freestanding, multi-layer structure, as shown in Figure 36. At this point, wires and tubing need to be attached to the contact pads and inlet / outlet ports. Additionally, a containment well for the solution of cells that are to be placed on top of the array of analysis cavities needs to be fabricated and attached to the microfluidic system.

The containment well is made with a polymer resin that is shaped using a laser that cures the resin at specified locations, a process known as stereolithography (SLA). To fabricate the SLA part, first a 3D rendering of the part is designed in SolidEdge, a 3D computer aided design software package. The part file, .par, is then converted into an .stl file, which is the file type used by the Viper Stereolithography System (3D Systems, Valencia, CA). The Viper software, Lightyear, converts the .stl file into the information required by the SLA system that determines where to fire the laser. After the part is formed in the SLA system, it is cured in a UV oven for one hour.

Different versions of the design for the containment well exist based on how the fabrication and testing of the microfluidic system progressed. The first version of the containment well has four 1 mm thick walls with inner dimensions of 10.5 mm by 9.5 mm that fits around the array of analysis cavities. With this version, tubing used to access the inlet and outlet ports are connected perpendicular to the surface of the microfluidic system using plastic

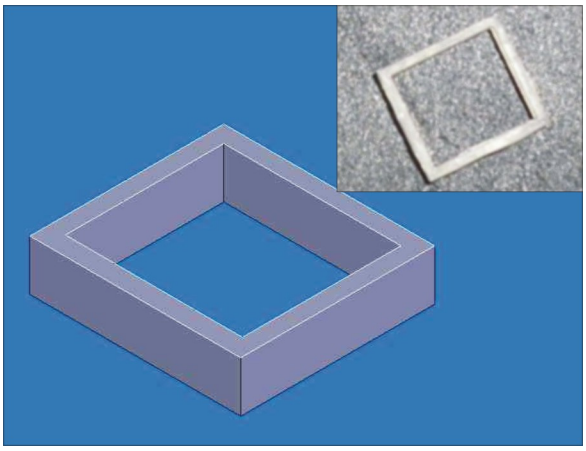

Figure 37: The first containment well is a simple four-walled structure simply used to contain a solution of cells on top of the array of analysis sites. Inset: Actual SLA part.

ferrules (Upchurch Scientific, Oak Harbor, WA). Figure 37 shows the 3D schematic of the containment well and the resulting SLA part. This design is sufficient for isolating the fluid solution on top of the array of cavities and for providing access to the inlet and outlet ports without leaking. However, when viewing the array of cavities with an upright microscope, the tubing coming up from the inlet and outlet ports obstructs the microscope objectives. Therefore, not all of the cavities are viewable. The second version of the containment well addresses this problem by including channels that provide access to the inlet and outlet ports in the SLA part itself, Figure 38. These channels allow the tubing that access the inlet and outlet ports to remain parallel to the surface of the microfluidic system. The third version of the containment well is defined for the fourth design of the microfluidic system only. These containment wells also provide access to the inlet and outlet ports, but since they are designed for the microfluidic system with four independent fluidic channels, they provide access to four sets of inlet and outlet ports, Figure 39.

The containment well and microfluidic system are aligned by hand with the aid of a microscope. Both parts are transparent, and therefore, it is possible to see the inlet and outlet ports through the containment well and vice versa. Once they are aligned, they are held in place with binder clips and bonded together with a two-part epoxy. The tubing for the inlet and outlet ports is Teflon® FEP (Upchurch Scientific, Oak Harbor, WA) with an inner diameter of 0.03 inches and an outer diameter of 0.0625 inches. The tubing is slid into

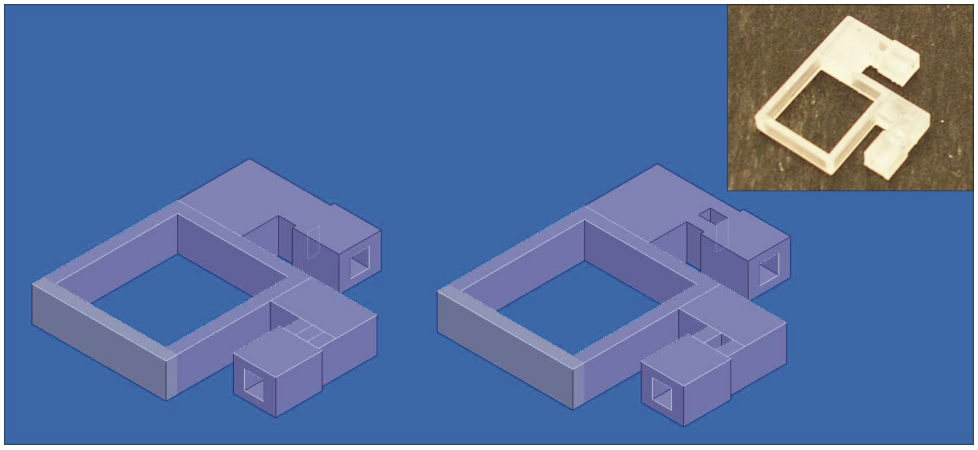

Figure 38: The second containment well included channels that provided access to the inlet and outlet ports. This part allowed tubing connected to the microfluidic system to remain parallel to the device itself, which is necessary for using a microscope with the system. Both a top and bottom 3D-view are shown. Inset: Actual SLA part.

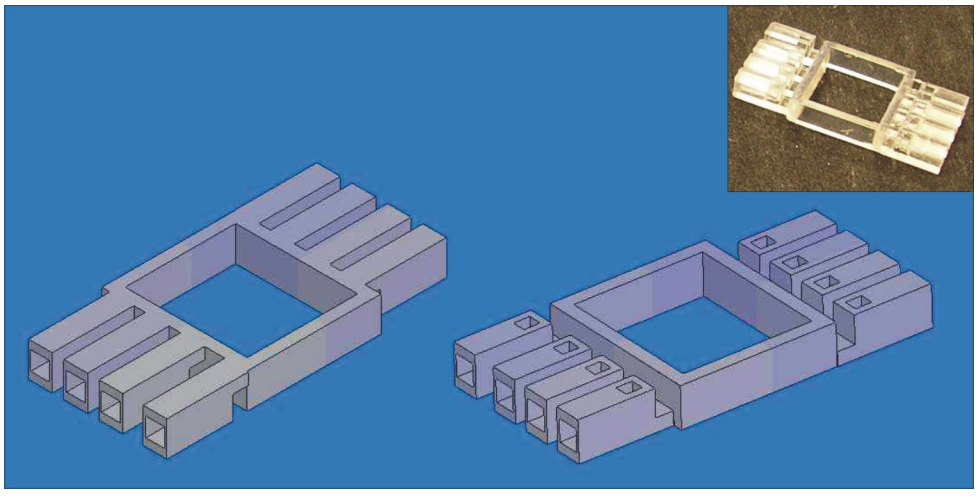

Figure 39: The third containment well is designed for the fourth version of the microfluidic system: four independent fluidic channels each with and inlet and an outlet port. Both a top and bottom 3D-view are shown. Inset: Actual SLA part.

the channels in the SLA part and sealed into place also with two-part epoxy. The wires for the analysis cavity electrodes and the fluidic channel electrodes are electrically connected to the exposed contact pads with silver paste (SPI Supplies) and then covered with two-part epoxy to hold them in place and to provide electrical isolation. After the epoxy is applied to the SLA parts and the wires, the devices are set aside for at least 24 hours to insure adequate curing.

CHAPTER IV

EXPERIMENTAL METHODS USED FOR STRUCTURAL ANALYSIS AND DATA COLLECTION

Ensuring device functionality is a critical part of the development of any device. For this multi-layer microfluidic system, proper functionality includes mechanical stability after fabrication and packaging and during normal operation and the ability to accurately perform the intended cellular analyses. This chapter first describes the method used to verify mechanical stability and then explains the techniques followed for collecting impedance spectroscopy data and giga-seal measurements.

4.1 Monitoring Structural Stability During Flow through the Microchannel

As is discussed in Chapter 2, normal operation of the multi-layer microfluidic system involves filling the microchannel with a cell buffer solution prior to dispensing the solution of cells on top of the array of cell cavities. The limit of how much pressure can be applied to the fluid flowing through the channel before the device fails is determined by pushing fluid into the channel through the inlet port at a specified rate while measuring the pressure at that inlet port. Visual inspection of the channel during this test is also used to verify the formation or absence of leaks.

To measure the pressure seen at the inlet to the channel in the microfluidic system while applying a steady flow rate to the fluid being pushed through the channel, the experimental setup shown in Figure 40 is used. First, a syringe (Becton, Dickinson and Company, San Jose, CA) filled with 10 mL of de-ionized (DI) water is placed in a syringe pump (KD Scientific, Holliston, MA) that will be used to control the applied volumetric flow rate. Teflon® FEP tubing (Upchurch Scientific, Oak Harbor, WA), with an inner diameter of

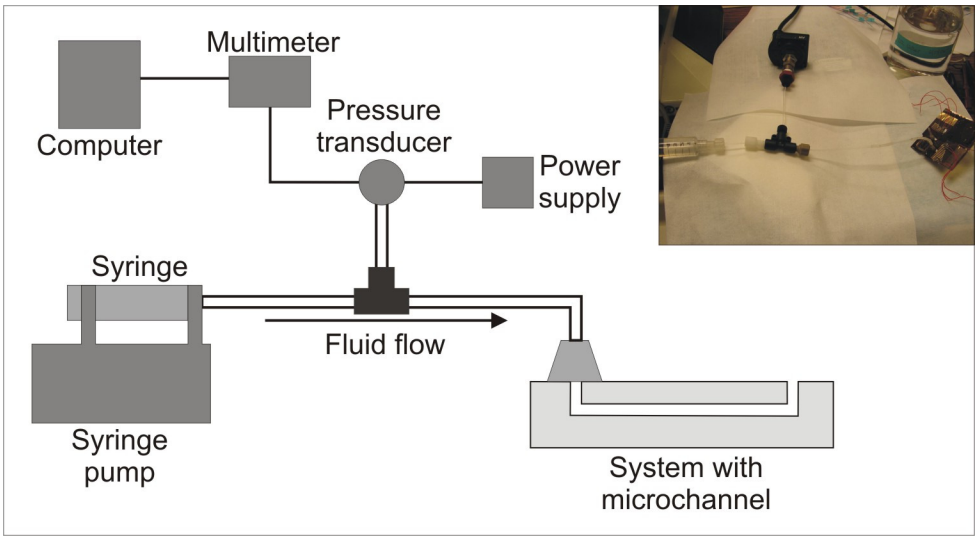

Figure 40: This experimental setup allows the pressure at the inlet of the microfluidic channel to be measured using a pressure transducer located in-line with the syringe / syringe pump and microfluidic channel. The output of the transducer is a voltage that corresponds to the induced pressure. This signal is measured by a multimeter and then read-in by a computer running a LabView program. Inset: A picture of the syringe, pressure transducer, and microfluidic system.

0.03 inches, is attached to the syringe through a luer-lok connector. A tee-connector (Upchurch Scientific) is used to interface this tubing and the tubing already attached to the inlet of the packaged microfluidic system. The third outlet of the T-connector leads to the pressure transducer (PX182-015GI, OMEGA Engineering Inc., Stamford, CT). The pressure transducer is powered with a DC power supply (E3611A, Hewlett-Packard, Palo Alto, CA) set at 10 V, and its output voltage, which corresponds to the pressure seen at the inlet, is measured with a digital multimeter (3458A, Agilent, Palo Alto, CA). A computer is connected to the multimeter and uses a LabView (National Instruments, Austin, TX) program to record the voltage and convert it into the corresponding pressure value.

The testing begins by running the LabView program, which starts collecting the voltage measured by the pressure transducer. Then, the flow rate is set on the syringe pump, and the flow is turned on. An increase in pressure at the inlet to the channel, as shown by the software, occurs until the pressure reaches a steady state value. This steady state value, as well as the applied flow rate, is recorded. The flow rate on the syringe pump is then increased to the next value of interest. Again, the pressure will increase and eventually

reach steady state. This process is continued until steady state pressures are recorded over the range of relevant flow rates. Flow rates from 0.2 $\frac{mL}{hr}$ to 5.5 $\frac{mL}{hr}$ are used for this analysis.

In addition to collecting pressure vs. flow rate data, visual inspection of the microfluidic system during this test is also used to detect any possible leaks. Since the device is transparent, it is possible to focus on every layer using a microscope. Therefore, it is also possible to see fluid flow throughout the channel; and if the layers delaminate, it is possible to see fluid leak between the layers.

4.2 Techniques Used for Data Collection with the Microsystem

As part of the validation of the developed multi-layer microfluidic system, the device was used to collect impedance spectroscopy data on dissociated cells and tissue samples and to perform giga-seal tests with fluorescently-labeled 1 μm and 10 μm diameter polystyrene microbeads (Bangs Laboratories Inc.) and dissociated cells. The dissociated cells and tissue samples were derived from squamous cell carcinoma of the head and neck (SCCHN) and were obtained from the laboratories of Dr. Georgia Chen and Dr. Doug Shin at Emory University in Atlanta, Georgia. The protocols for the maintenance and preparation of the samples are described in Appendix A.

4.2.1 Impedance Spectroscopy Analysis

Impedance spectroscopy measurements are collected on air, DI water, PBS, dissociated cells, and tissue samples using three of the developed microfluidic systems (devices A, B, and C). Devices A and B are both from the third design version discussed in Chapter 2: eight, large-diameter (240 μm) cavities, large and small alignment features, and a single fluidic channel. Device C is from the fourth design version, which is the same as version three except that there are four separate fluidic channels, each with access to two cavities. Data is collected using all eight cavities on each device.

The two types of dissociated cells used are 686LN and 686LN-M4e, which were representative human head and neck cancer cells at different progression stages. The 686LN cells metastasize poorly in nude mice, while the 686LN-M4e cells, which were selected from

the 686LN cells through an orthotopic animal model, are highly metastatic. As part of maintaining the dissociated cells, a cell passage is performed every four days; within these four days, the cells will proliferate and double in number, and therefore at the end of the four days, half of the dissociated cells are removed from the culture. It is known that cell properties will change after a certain number of passages, therefore for both these cell types, data is collected once at each passage from passage four through passage ten.

Unlike dissociated cells, tissue samples cannot be maintained for long periods of time without placing them in cryopreservation. Therefore, data is collected on fresh tissue samples within 24 hours of receiving them or on frozen samples within a few hours of thawing. The tissue samples are obtained from sections of human tumors grown in mice and surgically removed as part of a research project at Emory University. The research involves injecting cells from a human head and neck cancer cell line (KB-3-1) into specified locations on the mice and letting one group of the tumors grow without any medical interference (the control group) and the other groups grow while treating them with different drugs. The tissue samples used in this research for testing the microfluidic system included one fresh control sample and one fresh treated sample.

Before placing the cells or tissue samples onto the device for testing, some preparation of the device itself is performed. First, a 3 mL syringe with a luer-lok fitting (Becton, Dickinson and Company) is filled with deionized (DI) water or phosphate buffered saline (PBS). One end of a piece of flexible silicone tubing (Helix Medical, Inc., inner diameter of 0.04 inches and outer diameter of 0.085 inches) is connected to the syringe using a luer-lok adaptor (Becton, Dickinson and Company), and the other end fits snugly over the end of the tubing leading to the inlet port on the device, thus allowing the microchannel to be filled with the solution, Figure 41. The containment well surrounding the analysis cavities is then filled with the same solution. To ensure that any air bubbles trapped inside the via hole and / or cavity are removed, an ultrasonic bath (Boekel Scientific Inc.) is used. The portion of the device with the cavities is submerged for no more than 5 seconds into a pool of the same solution in a container floating in the bath. Visual inspection under a microscope is used to verify the absence of any air bubbles. The ultrasonic bath is used

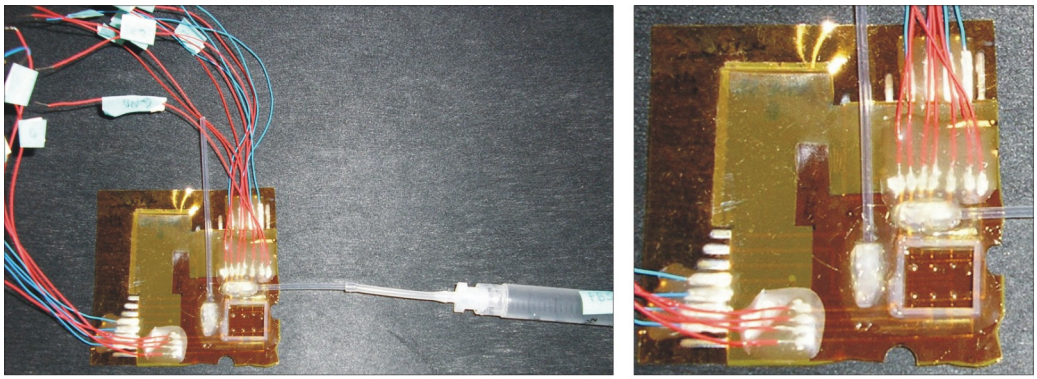

Figure 41: In preparation for running impedance spectroscopy experiments, the microfluidic channel is filled with a buffer solution. (A) Tubing connected to the outlet of the channel is left open while tubing at the inlet is attached to a syringe using larger diameter flexible tubing. (B) A close-up of the system shows the placement of the SLA containment well around the array of analysis cavities.

repeatedly until all air bubbles have been removed.

Once the device has been prepared, it is placed onto the stage of a microscope, and the wires bonded to the contact pads on the device are connected to an impedance analyzer (4294A, Agilent Technologies Inc., USA). The impedance analyzer is connected to a computer running a LabView program (Appendix B) that automatically collects and saves the magnitude and phase measurements based on user inputs and prompts. Data is collected over the frequency range of 40 Hz to 10 MHz at 800 data points based on a linear and logarithmic distribution within that range. Point averaging at four measurements per data point is also used. The microscope is fitted with a camera that sends a video image to the computer. The video is displayed through Measurement and Automation Explorer software (National Instruments), which is used to save .png image files. Figure 42 shows the testing setup.

The devices to be used for impedance spectroscopy analysis are first characterized with air, DI water, and PBS in the analysis cavities before collecting measurements on the dissociated cells or tissue samples. For the biological testing, additional preparation of the device takes place. When dispensing the dissociated cells or the tissue samples onto the device, a great amount of control is required so that the sample ends up in the cavity of

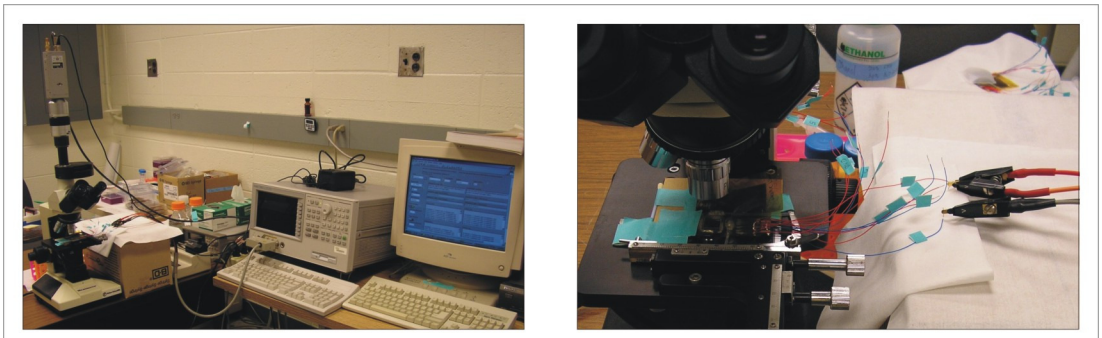

Figure 42: (A) For performing impedance spectroscopy experiments, a microscope, impedance analyzer, and computer running data and image acquisition programs are used. (B) The microfluidic system is positioned on the microscope stage and the wires attached to the contact pads on the device are connected to the leads from the impedance analyzer.

interest and not floating around in the containment well. To help with the control, most of the solution in the containment well is removed just prior to testing leaving only enough to maintain fluid in the cavities.

For collecting impedance spectroscopy data on the dissociated cells, measurements from only one cavity at a time are collected. To start, 1.2 μL of the cell suspension is dispensed from a pipette into the cavity of interest. The microscope is used to verify that the cavity is filled with the cell suspension. If the cavity is not full, manual manipulation of the dispensed solution is used to move the cells into position or another 1.2 μL of the cell suspension is dispensed. Once the cavity is filled, the LabView program controlling the impedance analyzer is run, and an image of the filled cavity is captured. Figure 43 shows a cavity filled with only PBS and a cavity filled with the cell suspension. This procedure is repeated for all the cavities and devices under investigation.

The procedure for collecting impedance spectroscopy data on the tissue samples is the same except for the placement of the tissue sample into the cavity. For the tissue samples, a blunt-end 30-gauge needle with an inner diameter of 152.4 μm and outer diameter of 300 μm (Small Parts, Inc.) is used to isolate a small section of the tissue sample. The same needle is then used to place the small section of tissue into the cavity of interest. To ensure that the sample does not dry up during the data collection, 2 μL of the solution in which the tissue sample is maintained is dispensed on top of the tissue while in the cavity. Then,

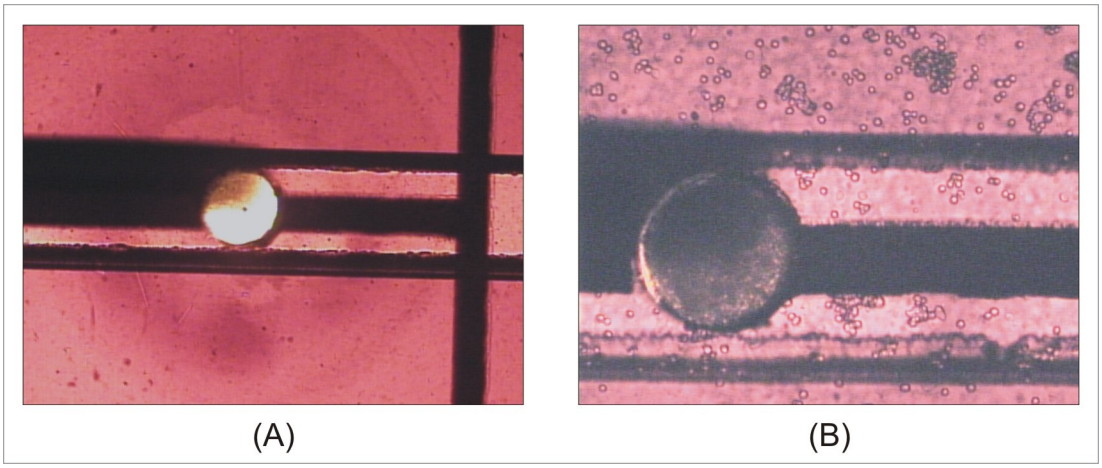

Figure 43: Impedance measurements are collected and an image of the analyzed cavity is captured once it is verified that the cells are in the cavity. (A) Prior to dispensing the cells, the analysis cavity is filled with PBS. (B) Data is collected once the analysis cavity contains a cluster of cells.

as with the dissociated cells, the LabView program is run and an image is captured, and the procedure is repeated for all the cavities and devices under investigation.

After all the cavities in one device have been tested with either dissociated cells or tissue samples, the containment well is filled with Trypsin (0.05%, Mediatech, Inc.), which is an enzyme that breaks down protein and therefore aids in the release of any biological material from the device if it has adhered to the surface. The portion of the device with the cavities is then submerged for no more than 5 seconds into a pool of DI water in a container floating in an ultrasonic bath. The device is then inspected under a microscope to verify the absence of any cell or tissue debris, and the bath is used repeatedly until all debris has been removed.

4.2.2 Giga-seal Testing

Giga-seal testing is performed with fluorescently-labeled 1 μm and 10 μm diameter polystyrene microbeads and dissociated cells using four of the developed microfluidic systems (D, E, F, and G). These microsystems are all from the fourth design version discussed in Chapter 2: eight, large-diameter (240 μm) cavities, large and small alignment features, and four separate fluidic channels each with access to two cavities. Testing is done on all eight cavities on each device. Unlike with the impedance spectroscopy analysis, only one of the dissociated

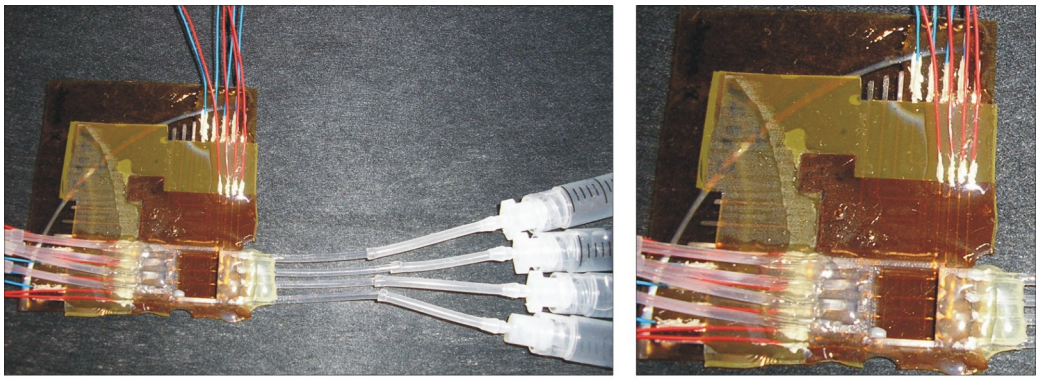

Figure 44: In preparation for collecting giga-seal measurements, the microfluidic channel is filled with a buffer solution. (A) This device contains four independent microfluidic channels, and therefore requires tubing and syringes to be attached at all four inlet ports. (B) A close-up of the system shows the placement of the SLA containment well around the array of analysis cavities.

cell types (686LN-M4e) is used for the giga-seal tests. Additionally, this test is unconcerned with the passage number of the cells, and therefore the cells are used at any passage number.

As with performing the impedance spectroscopy analysis, before placing the microbeads or cells onto the device to collect giga-seal measurements, some preparation of the device itself is performed. First, a 3 mL syringe with a luer-lok fitting (Becton, Dickinson and Company) is filled with deionized (DI) water or phosphate buffered saline (PBS). One end of a piece of flexible silicone tubing (Helix Medical, Inc., inner diameter of 0.04 inches and outer diameter of 0.085 inches) is connected to the syringe using a luer-lok adaptor (Becton, Dickinson and Company), and the other end fits snugly over the end of the tubing leading to the inlet port on the device, thus allowing the microchannel to be filled with the solution. For devices from versions one, two, or three of the microfluidic system, there is only one channel, so only one syringe is connected. For devices from version four of the microfluidic system, there are four independent channels and hence four inlet ports, so a syringe is connected to each of the channels, Figure 44. A piece of the same flexible silicone tubing approximately 1 inch in length is fit onto the tubing at the outlet of the channel. This flexible tubing is used so that the outlet can be clamped off using a binder clip during the giga-seal tests.

Once the device has been prepared, it is placed onto the stage of a microscope, and the wires bonded to the contact pads on the device are connected to a digital multimeter (3458A, Agilent Technologies Inc., USA). The digital multimeter is connected to a computer running a LabView program (Appendix C) that automatically collects and saves the impedance between the cavity electrode and the fluidic channel electrode. The impedance is continuously displayed on the screen on a graph plotting impedance vs. time. The microscope is fitted with a camera that sends a video image to the computer where Image-Pro Plus software (Media Cybernetics) saves the images as .tif files. This microscope also has the ability to detect fluorescence, which is used for part of the giga-seal testing.

For the giga-seal testing, the containment well does not need to be filled prior to running the experiment as was the case with the impedance spectroscopy analysis. Alternatively, to fill the cavities, the outlet port is clamped and pressure is applied to the syringe at the inlet, which forces fluid through the via holes and into the cavities. This procedure is verified through the microscope.

Giga-seal measurements from only one cavity at a time are collected. The LabView program collecting and displaying the resistance data is started prior to dispensing any microbeads or cells onto the cavity under investigation. In this way, the resistance for a fluid alone in the cavity, via hole, and channel as well as the change in resistance for when a particle is pulled towards the via hole is recorded. The image software is used at any time to record an empty cavity, particles floating around the cavity, and sequences of images showing the manipulation of particles due to negative pressure through the via hole.

At this point, 3.0 μL of the microbead or cell suspension is dispensed from a pipette on top of the cavity of interest. The microscope is used to verify that the microbeads or cells are in the vicinity of the cavity, and if they are not, manual manipulation of the dispensed solution is used or another 3.0 μL of the suspension is dispensed. For the microbeads, the microscope is used in a fluorescent mode. Once the samples are in an appropriate location relative to the cavity and via hole, a negative pressure is formed inside the cavity using the syringe. After resistance data is recorded for that particular cavity and via hole, the procedure is repeated for all cavities and devices under investigation.

After the cavities and via holes in one device have been tested with either the microbeads or dissociated cells, the containment well is filled with Trypsin to help release any material that might have adhered to the surface. The containment well is then rinsed with DI water to clean out the Trypsin and any debris, and the device is inspected under a microscope to verify the absence of any microbeads or cell debris. Rinsing with DI water is continued until all debris has been removed.

CHAPTER V

RESULTS AND DISCUSSION OF FABRICATION, STRUCTURAL TESTING, AND DATA COLLECTION

The procedures and methods described in Chapters 3 and 4 were used to fabricate and test multi-layer microfluidic systems. This chapter describes the results of using laser ablation to pattern the Kapton® sheets, creating microstencils and using them to pattern metal traces onto the Kapton® sheets, and using heat staking to bond the six patterned Kapton® sheets together. A completely fabricated and packaged microfluidic system is also described. The second half of this chapter presents and discusses the results for the fluidic channel testing as well as data that has been collected from the impedance spectroscopy analysis and giga-seal measurements.

5.1 Fabrication Results and Discussion

5.1.1 Material Selection

As was discussed in Chapter 3, spin-on polyimides were considered for the via layer of the microfluidic system since they could be used to produce layers that were thinner than the 50.8 μm thick Kapton® sheets. However, the characterization results for both the PI-2555 and the PWDC-1000 were not favorable. For the dry etching of the PI-2555, the oxygen plasma did not evenly etch the polyimide over the entire surface of the Si wafer, and some of the smaller features were not completely etched before the mask layer had been removed or the other features had been over-etched. Wet etching the PI-2555 in the photoresist developer did not cleanly remove the exposed polyimide, and the smaller features again did not come out. The PWDC-1000 did produce well patterned layers; however, they easily tore during the release stage.

The spin-on polyimides require more processing steps than polyimides that are already in sheet form. Additionally, the produced layers are of poor quality due to either incomplete

patterning or ripping during releasing. Therefore, since it has been found that it is possible to form the small diameter via holes into the 50.8 μm thick Kapton® sheets through laser ablation (as will be discussed later in this chapter), the thin layers made possible by using a spin-on polyimide are no longer necessary.

Besides spin-on polyimides, other biocompatible polymers (e. g. PDMS, PMMA, and parylene) are available with which to fabricate a microsystem for cellular analysis. For this project, characteristics of the material other than just biocompatibility are important. Kapton® maintains adequate rigidity while also providing flexibility, which can aid in fabrication and operation. Its wide operating temperature range allows a microsystem made of Kapton® to be used in many types of applications and environments. Since Kapton® is also transparent, such a microsystem can be placed into most existing laboratory setups. Finally, the ability to pattern it with the necessary features and to bond multiple layers of Kapton® to each other makes it an ideal material with which to fabricate a multi-layer microsystem.

For this microfluidic system, Kapton® E is used for the base and top cavity layers and Kapton® EKJ is used for the isolation, channel, via, and bottom cavity layers (Figure 45. At one point in the development of the fabrication process, alternating between Kapton® E and EKJ from layer to layer was attempted. However, this arrangement did not produce favorable results during testing of the structural stability of the microchannel, which is discussed in a later section of this chapter. Therefore, only devices that had Kapton® EKJ for all the interior layers were used for structural testing and data collection.

5.1.2 Laser Ablation

The six layers of the microfluidic system require features from a few microns to a few millimeters in diameter to be defined in the Kapton® sheets. These features include alignment holes, inlet / outlet ports, cavity openings, via holes, and fluidic channels. Schematics showing the placement of these features were presented in Figures 11, 12, 13,and 14 in Chapter 2. Table 1 lists all the layers of the microfluidic system, the features patterned into each of those layers, and the dimensions of those features. Based on these requirements and the

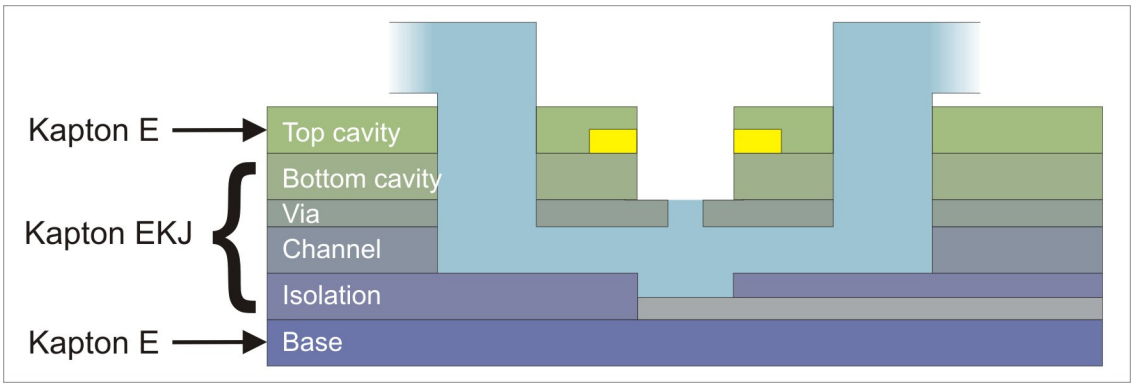

Figure 45: Kapton® E is used for the top and bottom layers (Base and Top Cavity) of the microfluidic system while Kapton® EKJ is used for all interior layers.

characteristics of the excimer and CO_2 laser systems described earlier in Section 3.3.1, the excimer laser can be used to pattern any of the layers; but due to the limited beam spot sizes available, the CO_2 laser can only be used to pattern the base, isolation, and channel layers.

Before patterning the Kapton® sheets with the excimer laser, characterization tests were run on 50.8 μm thick Kapton® E and EKJ sheets to determine the appropriate ablation parameters. The LPX200 laser exhibits stable performance at energy levels from 150 mJ to 300 mJ and at operating frequencies of 60 Hz and 100 Hz. Metal projection masks with diameters ranging from 70 μm to 2.4 mm were readily available, therefore a demagnification of 10 was used to achieve the various beam spot sizes for the required features. The characterization was performed under the following conditions: laser energy from 90 mJ to 400 mJ, pulse frequency of either 60 Hz or 100 Hz, optical demagnification of 10, attenuation from 30% to 95% transmission, 70 to 400 pulses for a single point, and projection mask diameters of 2.4 mm, 2 mm, 1 mm, 200 μm, 100 μm, and 70 μm. For the various projections masks, this showed sufficient ablation at 250 mJ, 60 Hz, 75% transmission, and from 100 to 140 pulses. Table 2 lists the ablation parameters used for the various features on each layer in the microfluidic system. On average, 100 to 120 pulses are required to pattern features from 4 μm to 250 μm in diameter into the 50.8 μm thick Kapton® sheets. Some results of the excimer laser ablation process are shown in Figure 46.

Table 1: The features patterned into each of the layers of the microfluidic system through laser ablation range in size from 4.7625 mm down to 4 μm in diameter. The layers with only features greater than 160 μm in diameter can be patterned using the CO_2 laser, while all the other layers must be patterned on the excimer laser.

	Microfluidic System Layer					
Feature	Base	Isolation	Channel	Via	Bottom Cavity	Top Cavity
Large Alignment Holes	4.7625 mm					
Small Alignment Holes	240 μm					
Electrode Access Holes	-	240 μm	-			
Channel	-		500 μm	-		
Inlet / Outlet Ports	-			240 μm		
Via Holes	-			4 μm	-	
Analysis Cavities	-				240 μm, 100 μm, or 20 μm	
All Dimensions Refer to Diameter Except the Channel Width						

Table 2: To pattern the features into the 50.8 μm thick Kapton® sheets, the excimer laser was run at 250 mJ, 60Hz, and 75% transmission. The appropriate sized features were obtained using projection masks 2.4 mm in diameter down to 70 μm in diameter with a demagnification of 10. On average, 100 to 120 pulses were required to ablate through the Kapton®.

	Laser Ablated Features								
Laser Parameters	Large Alignment Holes	Small Alignment Holes	Channel	Electrode Access Holes	Inlet / Outlet Ports	240 μm Cavities	100 μm Cavities	20 μm Cavities	Via Holes
Projection Mask Diameter	2.4 mm					2.4 mm	1.0 mm	200 μm	70 μm
Resulting Beam Size	240 μm					240 μm	100 μm	20 μm	7 μm
Pulses	100	110	120	110	110	100	100	110	120
Common Laser Parameters: Energy = 250 mJ, Frequency = 60 Hz, Transmission = 75%, De-magnification = 10									

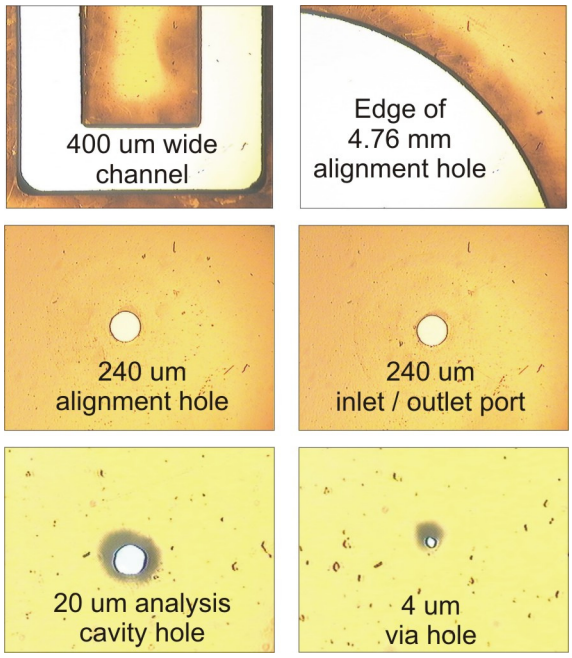

Figure 46: The excimer laser can be used to ablate any of the features in the microfluidic system. This laser produces smooth lines with minimal thermal damage.

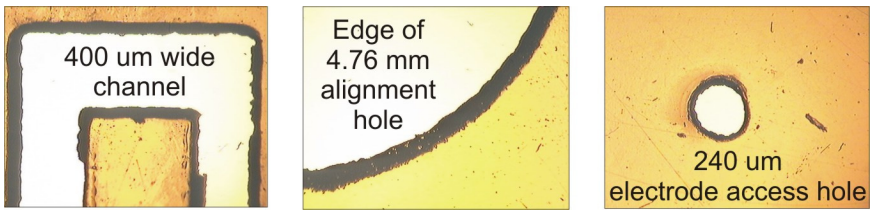

Figure 47: The CO_2 laser can be used to ablate features greater than 160 μm in diameter: large and small alignment holes, large-diameter analysis cavities, fluidic channels, electrode access holes, and inlet / outlet ports. This laser produces rough edges as compared to the excimer laser due to thermal effects.

Characterization was also performed with the CO_2 laser system prior to patterning the Kapton® sheets. This process was simply done by varying the power level and speed on a 50.8 μm thick sheet of Kapton® while maintaining a minimum beam spot size of 160 μm. Characterization showed that sufficient ablation occurred at 10% power and 15% speed. Results of the CO_2 laser ablation process on the base, isolation, and channel layers are shown in Figure 47.

Besides the fact that the CO_2 laser beam cannot be physically masked, thus limiting the minimum beam spot size to 160 μm, another issue that deems the excimer laser system superior is surface roughness of the ablated regions of Kapton®. As seen in Figure 48, the

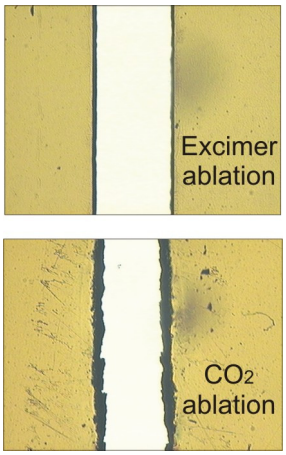

Figure 48: Both the excimer and the CO_2 lasers can produce 400 μm wide trenches. Due to thermal effects, the CO_2 laser leaves behind edges that are much more rough than with the excimer laser. However, the CO_2 laser is much faster. For features where size and topography are not critical, rough surfaces are an acceptable trade-off to speed.

excimer laser system leaves much smoother edges on the ablated features than the CO_2 laser system. The difference in surface roughness is due to the different methods the excimer laser and the CO_2 laser use to remove material. With an excimer laser, the energy in the laser is used to break the bonds in the polymer chains, and the force of the impact actually pushes the material out of that region [10]. With a CO_2 laser, a thermal process is responsible for the degradation of the material in that region [70]. Therefore, thermal damage will occur in the ablation region, and a rougher edge will remain. For the larger features, which the CO_2 laser would be used to pattern, size and topography are not critical, and therefore, the edges of the ablated features do not have to be completely smooth. In addition, as was mentioned previously, the CO_2 laser system is much faster than the excimer laser system. For example, a 4 mm diameter hole ablated into a sheet of Kapton® takes 90 seconds on the excimer laser with a 240 μm diameter beam, whereas it only takes 3 seconds on the CO_2 laser. Therefore, for larger features, greater than 160 μm, where the size and topography are not critical, rough surfaces are an acceptable trade-off to speed.

An issue with any laser system during ablation is the attenuation of the energy density through the thickness of the substrate material. In a 50.8 μm thick Kapton® sheet, this causes the exit opening to have a smaller diameter than the entrance opening. This occurrence can be seen in Figure 49 in which the entrance to the laser ablated holes are

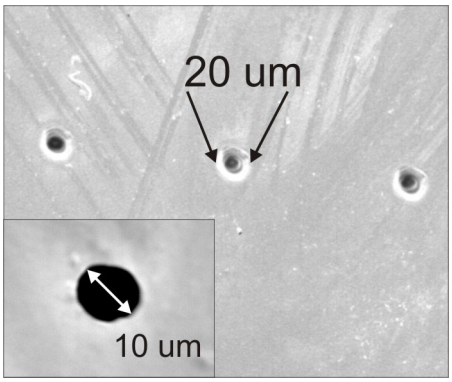

Figure 49: The energy density of a laser attenuates through the thickness of a substrate material. This causes a tapering effect: the entrance hole is larger than the exit hole. The main image shows a 20 μm diameter feature on the topside of the substrate. The inset shows that same hole from the backside of the substrate, and it's diameter has shrunk to 10 μm.

20 μm at their widest points while the exit hole is only 10 μm at its widest point. Further examples of this taper can be found in Crafer et al. [28]. For the small-diameter analysis site openings and the via holes, the diameters are critical. Therefore, this attenuation has been taken into consideration when setting the ablation parameters. Acceptable feature sizes are obtained by basing the beam spot size on the diameter of the exit opening that would be achieved. As shown earlier in Table 2, beam spot sizes of 200 μm and 70 μm were used to form the small diameter analysis cavity holes and the via holes respectively. Due to the tapering, these settings formed 15 μm diameter and 4 μm diameter holes on the backsides of the sheets of Kapton®, which are the target sizes of the aforementioned features.

5.1.3 Microstenciling

For the fluidic channel electrodes, the metals that are to be deposited were initially determined such that these electrodes would comply with the protocol that is used in conventional patch-clamp experiments, which is silver (Ag) with a silver chloride (AgCl) coating. Based on common MEMS fabrication techniques, to promote adhesion between the Kapton® and the Ag, a thin adhesion layer, such as chromium (Cr), needs to be deposited before the Ag [56, 99]. After metalization, the patterned Kapton® sheets undergo a high temperature bonding process. During fabrication, it was found that the simple Cr / Ag layers did not handle the high temperature process well, and they became poor conductors. In fact, before

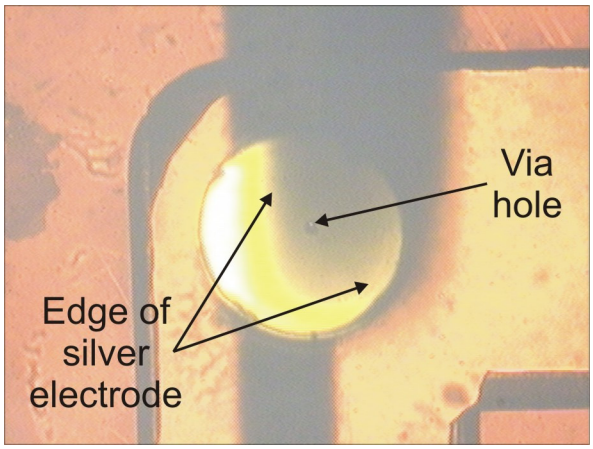

Figure 50: The holder used to align the fluidic channel electrode microstencil to the Kapton® sheet uses only large alignment holes and pins, and therefore may not provide perfect alignment during metal deposition. However, since the alignment of the fluidic channel electrode to any overlaying features in not critical, the amount of mis-alignment is acceptable.

pressing, the traces had an average resistance of 35.46 Ω, and after pressing a resistance from one end of the trace to the other end would not register on a hand-held multi-meter. Therefore, an additional metal that could handle high temperatures better, platinum (Pt), was added between the Cr and Ag. After pressing, the Cr / Pt / Ag traces had an average resistance of 31.4 Ω.

The placement of the fluidic channel electrodes onto the base layer of the microfluidic system is not critical. The traces are located at the bottom of the fluidic channel, and therefore only need to be under the analysis cavity and not in contact with any specific feature. The holder used to keep the Kapton® sheet and microstencil together during metal deposition provides sufficient alignment with 4.7625 mm pins. Based on measurements made on more than 10 fabricated microsystems, the fluidic channel electrode and the via hole are off-center from each other by an average of only 69.8 μm, which is sufficient for collecting giga-seal measurements (Figure 50). Figure 51 shows a fluidic channel electrode microstencil and the resulting metalized Kapton® sheet. A single microstencil has been used over 10 times without any statistically significant changes in the resulting metal traces.

To create the cell cavity electrode microstencil, rather than having to process from both sides of the Si wafer, a thinner wafer could have been used. Previous attempts used 150 μm

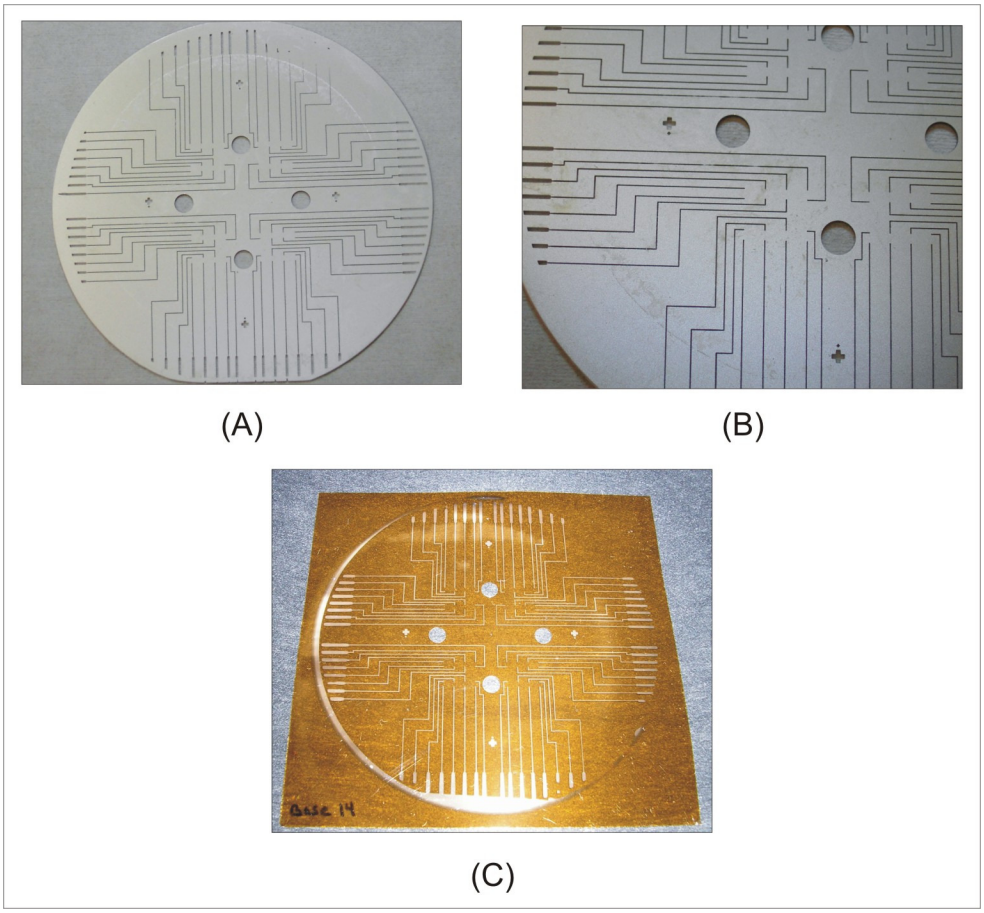

Figure 51: (A) The fluidic channel electrode microstencil is fabricated out of a 4 inch silicon wafer, which can be used to pattern sheets of Kapton® for four microfluidic systems at one time. (B) It contains features as small as 100 μm wide that connect to 500 μm wide features at the edge of the wafer. (C) A single microstencil has been used to pattern the fluidic channel electrodes onto sheets of Kapton® over 10 times without any statistically significant changes in the resulting metal traces.

thick Si wafers and only etched features from one side of the wafer. However, this procedure was difficult to complete without breaking the wafers. This had two causes. First, a 150 μm thick wafer is fragile and can easily break during normal handling. Second, the patterns that were being etched into the wafer were complex and took up most of the surface area of the wafer. After the etching process, some parts of the wafer were only connected by a 100 μm wide section of silicon. These sections were mechanically weaker on the thinner wafers than the 350 μm thick wafers and tended to break easily. So even if the wafer survived its own fabrication, the microstencil easily broke during the fabrication of the microfluidic systems. Therefore, the benefit of being able to pattern multiple sheets of Kapton® with a single microstencil no longer existed. The 350 μm thick microstencils that go through both topside and backside processing are more durable and can therefore be used in the patterning of multiple sheets of Kapton®.

The trenches etched into the analysis cavity electrode microstencil must line up to the analysis cavities ablated into the Kapton® sheet. Since this alignment is performed by hand, a microscope is used to verify alignment prior to clamping the glass plate and microstencil holder together as was described in Section 3.3.2. With the first version of the microfluidic system, with 15 μm diameter analysis cavities, alignment was poor (Figure 52). By increasing the analysis cavity diameter to 240 μm, alignment was much easier to obtain, as shown by some later samples in Figure 53. An intermediate analysis cavity diameter, 100 μm, was also attempted. These features were also easily aligned by hand, however, since the microstencil and Kapton® sheet were not in perfect contact during metal evaporation, the metal traces shorted around the smaller diameter opening. Since the 240 μm diameter cavities provided the most success with alignment without resulting in shorting the electrodes together, this cavity size was used in the microfluidic systems used for all data collection. Figure 54 shows a cavity electrode microstencil and the resulting metalized Kapton® sheet. A single cavity electrode microstencil has been used to repeatedly pattern over 15 Kapton® sheets without any statistically significant changes in the resulting metal traces.

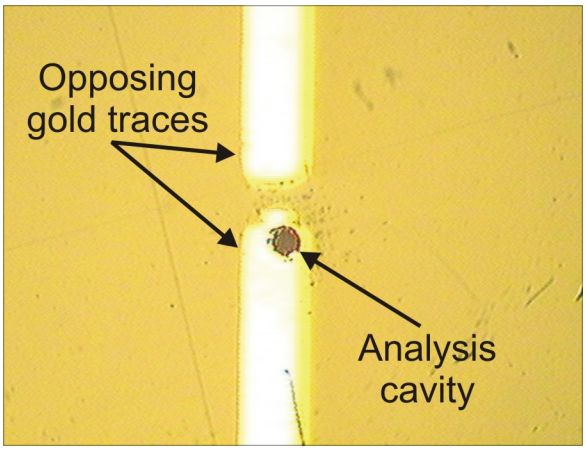

Figure 52: Since the alignment of the cavity electrode microstencil and laser ablated Kapton® sheet is performed by hand, a certain amount of mis-alignment is possible. This mis-alignment was substantial enough with the small-diameter analysis cavities (15 μm) that the metalized layers would be unusable for microfluidic system testing.

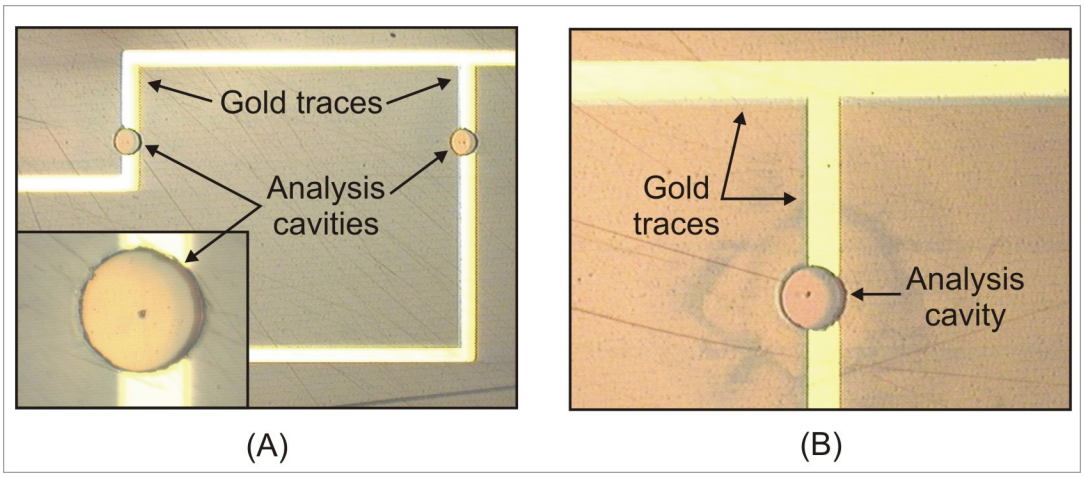

Figure 53: With a large diameter analysis cavity (240 μm), repeatable and acceptable alignment between the cavity electrode microstencil and the laser ablated Kapton® sheet was possible to perform by hand.

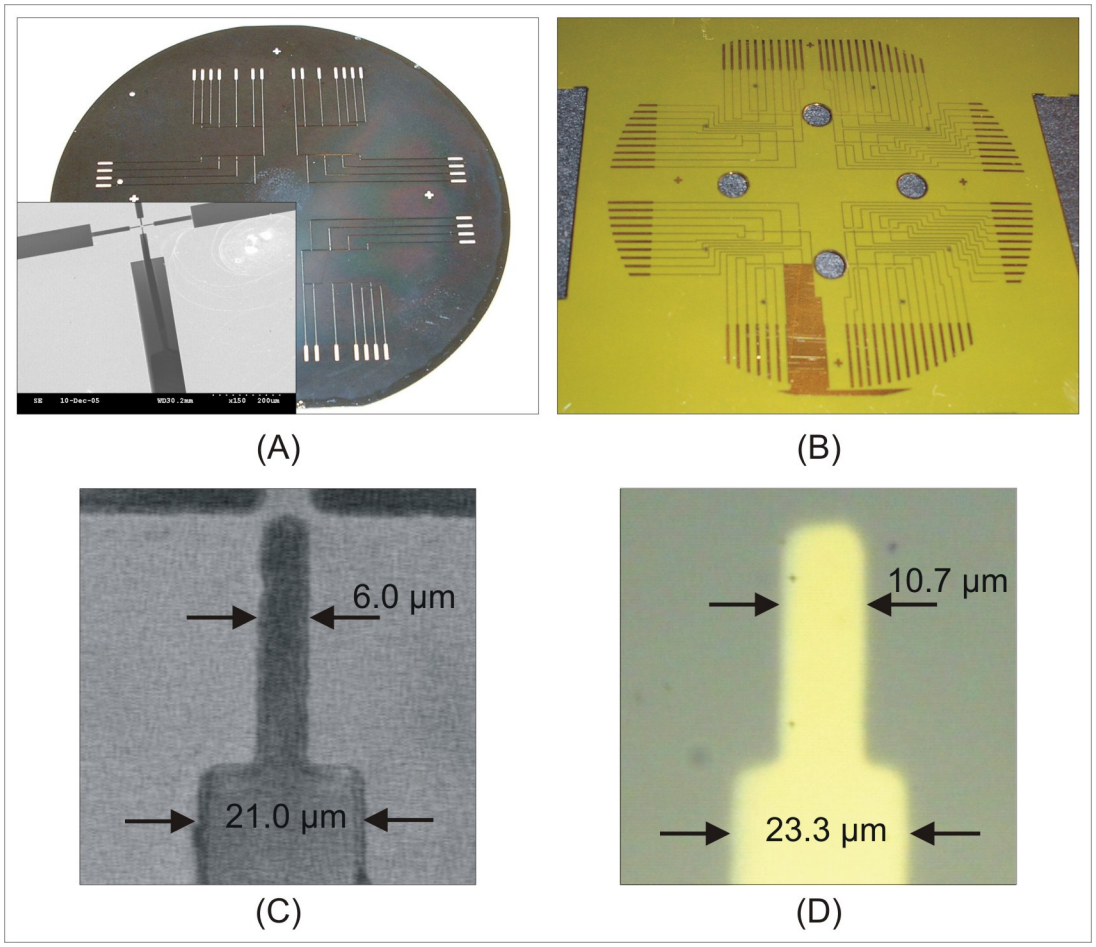

Figure 54: (A) The cavity electrode microstencil is fabricated out of a 3 inch silicon wafer, which can be used to pattern sheets of Kapton® for four microfluidic systems at one time. Due to both backside and topside processing, it contains features as small as 8 μm wide. Inset: An scanning electron micrograph (SEM) of the 8 μm, 20 μm, and 100 μm wide features. (B) A single microstencil has been used to pattern the cavity electrodes onto sheets of Kapton® over 15 times without any statistically significant changes in the resulting metal traces. (C) A close up of the smallest etched feature in the microstencil shows the final actual size is around 6 μm. (D) A close up of the resulting metal trace onto a sheet of Kapton® shows the actual size is around 10 μm. This spreading is due to imperfect contact between the microstencil and the Kapton® during metal deposition.

5.1.4 Alignment and Heat Staking

The most critical parts of the microfluidic system that need to be aligned from layer to layer are the analysis cavities and the via holes. The cavities are formed by the bottom cavity layer and the top cavity layer. The electrodes are patterned on the bottom cavity layer such that they end up between the two cavity layers. For the system to function as designed, the two layers that make up the cavity must be aligned and the via hole must be aligned such that it is within the footprint of the cavity.

In versions one and two of the microfluidic system, only the large alignment holes and posts were used. Initially, with the small-diameter analysis cavities, the precision in alignment was not satisfactory, and the two layers of the analysis cavity and the via hole did not line up well, Figure 55. In version two, with the large-diameter cell cavities, the layers still were not well aligned, but the larger features provided sufficient overlap such that the device could still function as intended. On average the features were 50 μm off, as shown in Figure 56. The introduction of the small alignment holes and posts in versions three and four of the microfluidic system enabled highly accurate alignment without any need for adjustments of any layer to be made by hand. After heat staking, the displacement between features was measured to be an average of 6.4 μm off. A sequence of images showing the progression of stacking all six layers together using both the large and small alignment features is shown in Figure 57.

After heat staking, visual inspection of the microfluidic system through a microscope confirmed that the high temperature and pressure process did not cause any damage to or deformation of the features that had been laser ablated. Figure 58 shows images of a multilayer system after heat staking. The layers also seemed to be adequately bonded together, however further investigation of the quality of the bond is discussed in Section 5.2 as part of the testing of the structural stability of the microchannel. Voids between layers where bonding did not occur could be detected visually. The use of the vacuum chamber and the polished stainless steel plates during heat staking reduced the formation of voids. As was discussed in the previous section, the heat staking process did have an effect on the metal traces. The Cr / Ag combination used for the fluidic channel electrodes did not maintain

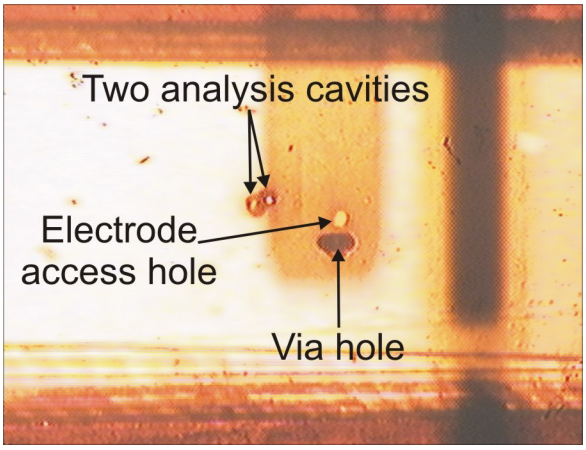

Figure 55: In design version 1 of the microfluidic system, small-diameter analysis cavities and large-diameter alignment features were used. This combination produced insufficient alignment between the top and bottom cavity layers and the via layer in the final bonded system.

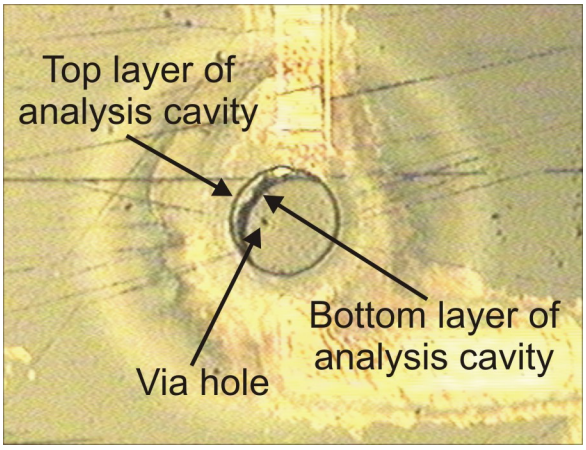

Figure 56: In design version 2 of the microfluidic system, large-diameter analysis cavities and large-diameter alignment features were used. Although some mis-alignment is still present, this combination produced sufficient overlap between the top and bottom cavity layers and the via layer in the final bonded system.

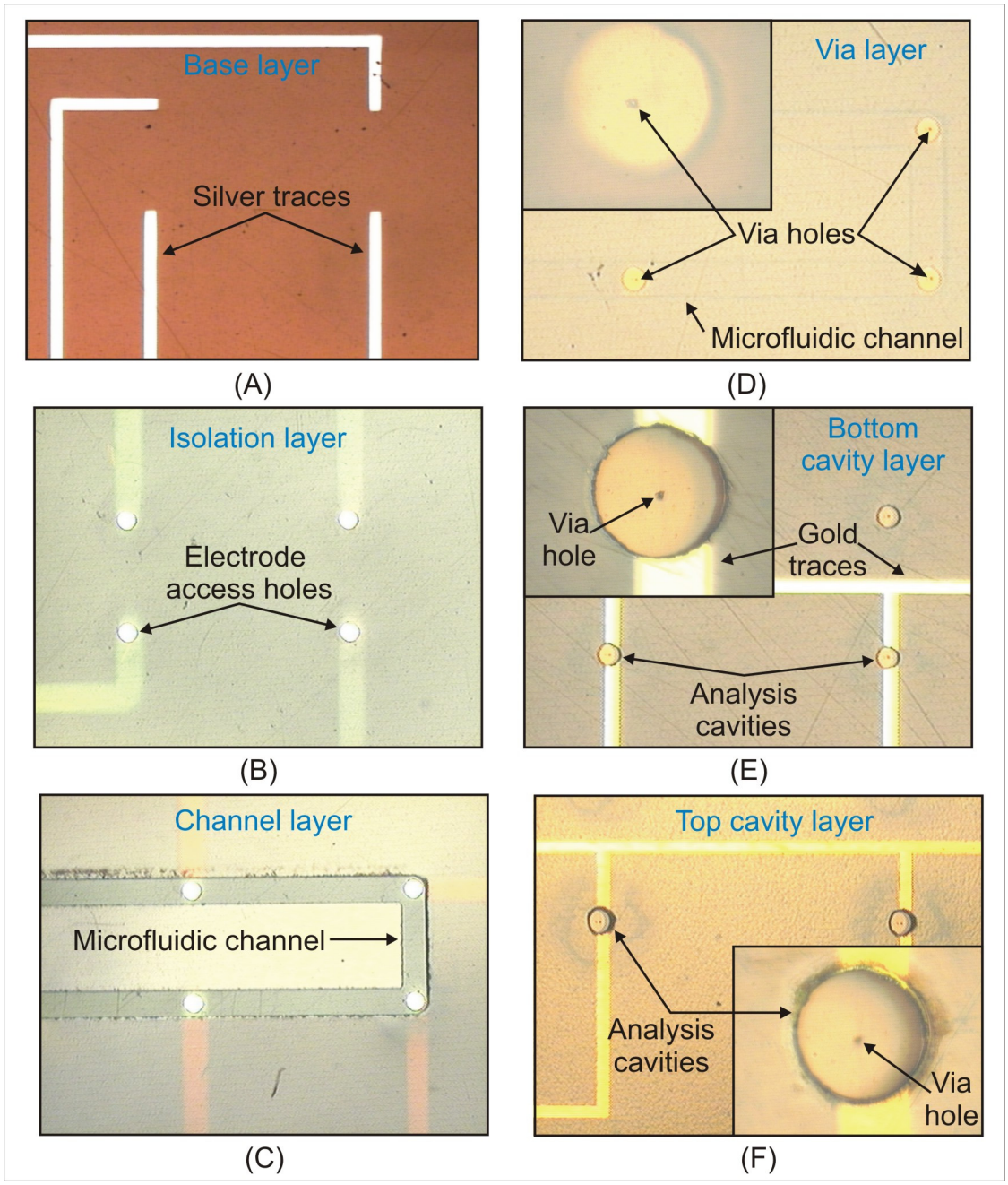

Figure 57: These images show the alignment achieved when stacking each of the layers of the microfluidic system on top of one another prior to heat staking when using the small-diameter alignment features. No additional alignment by hand is made. (A) The base layer alone. (B) Plus isolation layer. (C) Plus channel layer. (D) Plus via layer. (E) Plus bottom cavity layer. (F) Plus Top cavity layer. Insets show position of via hole within the analysis cavity.

its conductivity after heat staking. This problem was rectified by adding a Pt layer between the Cr and Ag.

5.1.5 Packaging

Figure 59 shows pictures of microfluidic systems packaged with the different SLA parts and with the electrical wires bonded to the contact pads. Careful application of the epoxy had to take place so that no leaks formed around the containment well or between the well and the inlet and outlet ports and so that the inlet and outlet ports and the cavities were not blocked. After the packaged devices had set aside for 24 hours, leaks were detected by placing fluid into the containment well and by sending it through the channels. By monitoring this process through a microscope, the locations of the leaks were determined. If a leak was found, the microfluidic system was emptied of all fluid and allowed to dry. The leaks were then covered with additional epoxy. This process was repeated until all leaks had been sealed.

5.2 Microchannel Stability Results and Discussion

During heat staking, due to the properties of Kapton® EKJ, as was discussed in Chapter 3, the polyimide adhesive film on either side of this material bonds to its neighboring material. In some of the microfluidic systems, Kapton® E and EKJ were alternated from layer to layer and Kapton® E was used for the top and bottom layers. In other systems, Kapton® E was only used for the top and bottom layers while Kapton® EKJ was used for all the interior layers. During fluidic testing of all the systems, it was found that those with Kapton® E as an interior layer were more susceptible to delaminating and forming leaks at some of the locations where fluid came into contact with the Kapton® E and EKJ boundaries. In contrast, those systems with Kapton® EKJ for all the interior layers did not delaminate nor form leaks during fluidic testing. Therefore, only those systems with Kapton® EKJ for all the interior layers were used for the more rigorous test on the microchannel that measured the pressure at the inlet vs. the applied flow rate.

For this test, only the single-channel versions of the microfluidic system (versions one, two, and three) were used. On average, the channel in these versions is 50.8 μm deep,

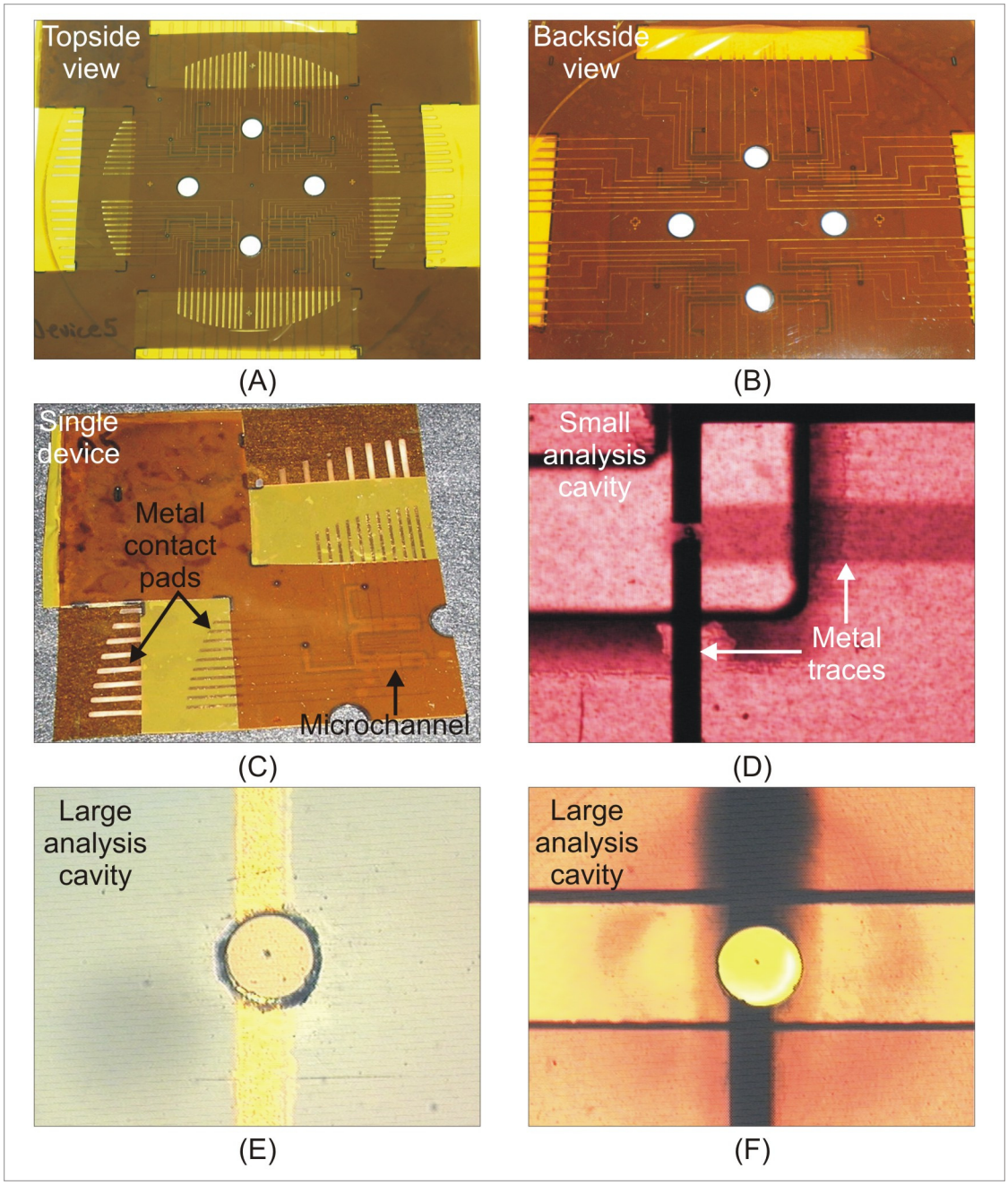

Figure 58: (A) A topside view shows four microfluidic systems (one in each quadrant) that have been aligned and heat staked at the same time. The gold metal traces and contact pads can easily be seen. (B) A backside view of the same systems highlights the silver metal traces. (C) In this single microfluidic system, the metal contact pads, microfluidic channel, inlet / outlet ports, and even one of the small alignment holes can be seen. (D) This closeup of a single small-diameter analysis cavity shows that the heat staking process did not damage the laser ablated features or the metal traces. (E) Using topside lighting, the alignment of the large-diameter analysis cavity and the via hole post-bonding is verified. (F) With backside lighting, the alignment of the fluidic channel and cavity electrodes and the microfluidic channel to the large-diameter analysis cavities is also verified.

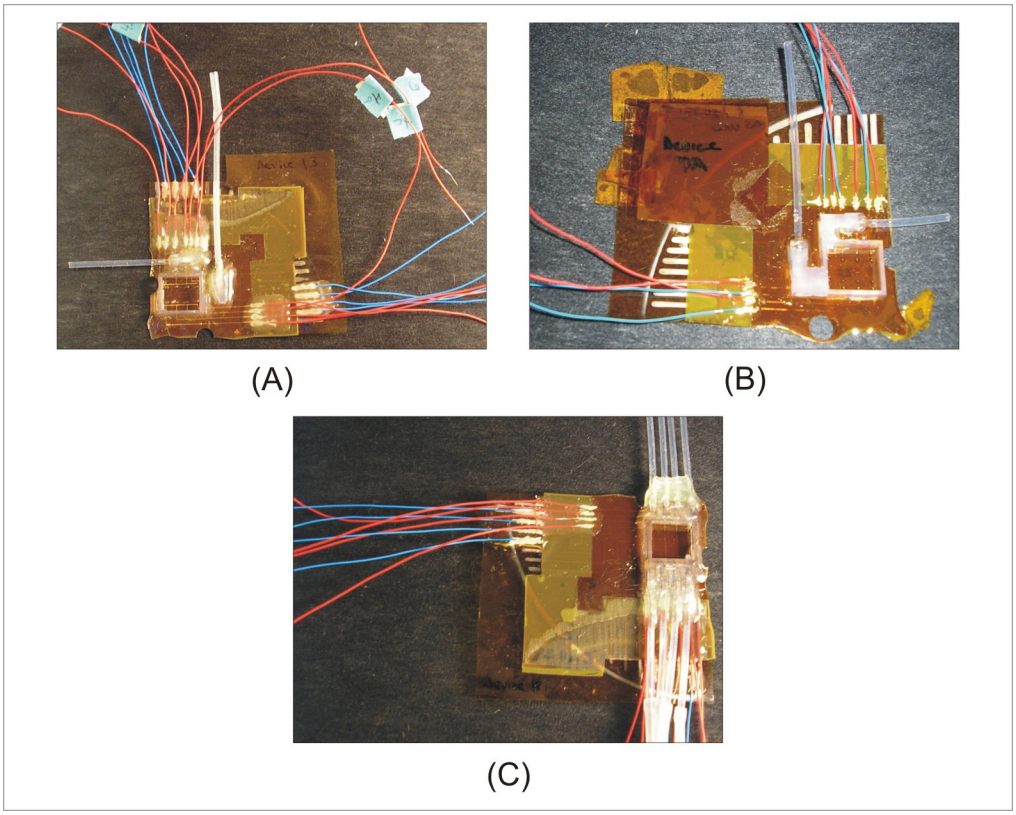

Figure 59: As part of the packaging process, the containment well is attached and wires are electrically connected to the contact pads. (A) and (B) show microfluidic systems with containment wells that provide access to a single microfluidic channel and ports for attaching tubing to the inlet and outlet. (C) This microfluidic system is packaged with a containment well that provides access to four independent microfluidic channels.

496.3 μm wide, and 63.4 mm in length, resulting in a volume of 1.60 mm^3. Flow rates from 0.1 $\frac{ml}{hr}$ to 5.5 $\frac{ml}{hr}$ (1.53 $\frac{mm^3}{sec}$) were used for this analysis. These values correspond to the flow rates that are used during normal operation of the system. The experimentally obtained microchannel inlet pressure vs. flow rate is shown in Figure 60. As was discussed in Section 2.2.1 as part of the structural stability analysis, the linear increase in pressure as flow rate increases is expected due to the theories involved in fluid dynamics. The theoretical results that were determined in Section 2.2.1 along with the experimental results are shown in Figure 61. Since the linear nature of the experimental results does not change along the flow rates of interest, it can be inferred that the microfluidic channel does not fail. If a leak had formed in the channel, the pressure would have deviated from the linear response at the higher pressures. The experimental data fits with the theoretical values within an error of 5.4% (standard deviation of 11.4%) over the entire data range and within 2.1% (standard deviation of 3.2%) from 0.5 $\frac{mL}{hr}$ to 5.5 $\frac{mL}{hr}$. The larger error at the lower flow rates can be attributed to the precision of the pressure transducer. The transducer is rated for pressures from 0 to 100 psi, and below 0.5 $\frac{mL}{hr}$, the measured pressure is around 0.1 psi. This data along with the visual verification that no leaks were seen during testing confirms that the bond between the Kapton® layers is sufficient for the applications in this project.

Another value to be considered when analyzing the bond quality of the Kapton® is the peel strength. Peel strength indicates how much pressure is required to peel apart two bonded surfaces by peeling one of the surfaces away from the other at either 90° or 180° angles and is given in units of force per unit width of the material. Kapton® KJ bonded to other types of Kapton® has a peel strength of 6 pounds per inch (pli) [35]. The pressure exerted on the microchannel wall correlates to using pressure to peel apart the layers that form the microchannel. If the total length of the perimeter of the cross-section of the microchannel is considered as the unit width of material (approximately 1100 μm), then this corresponds to needing 138 psi of applied pressure before overcoming the peel strength of 6 pli. From the theoretical calculations and experimental results already presented, the maximum pressure applied to the microchannel is 2.06 psi for a flow rate of 5.5 $\frac{mL}{hr}$. To achieve 138 psi at the inlet of the channel, using the theory explained in Section 2.2.1, a

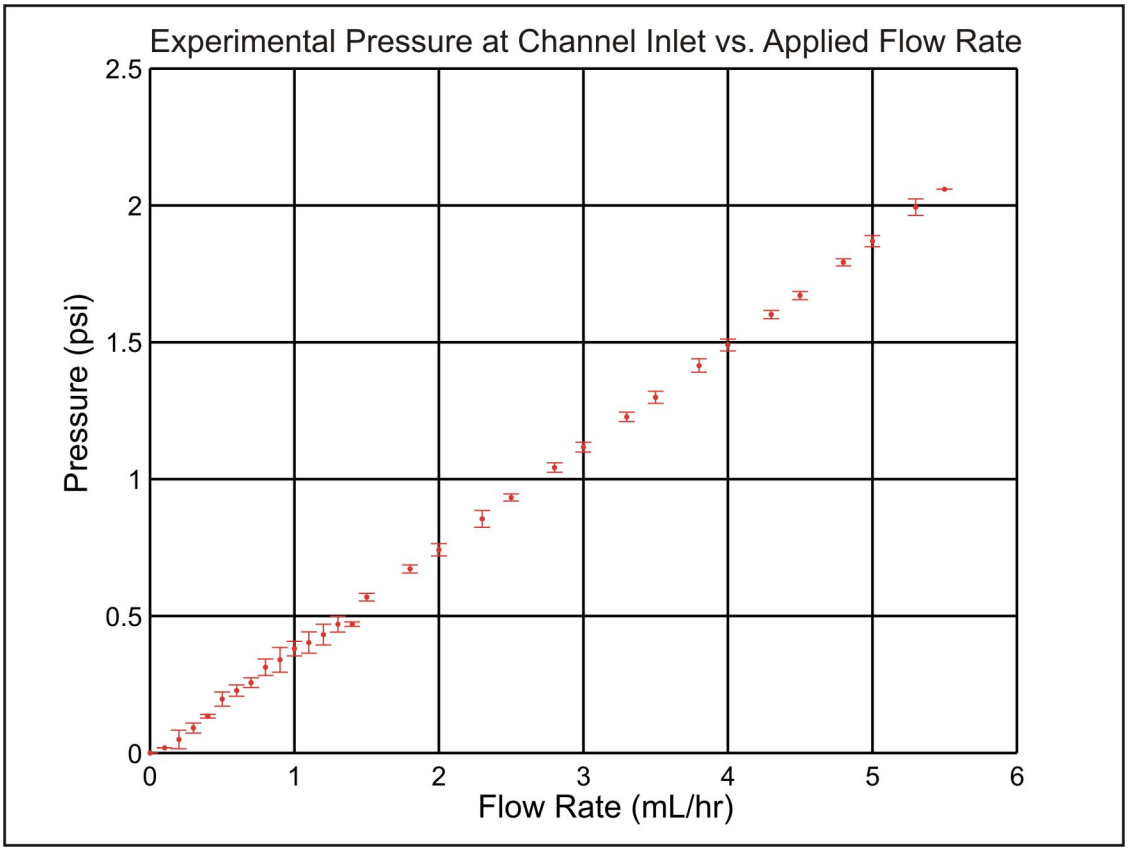

Figure 60: The data collected from the experimental analysis measuring the pressure at the inlet of the microfluidic channel due to an applied flow rate shows a linear increase in pressure for increasing flow rates. The data does not drop off at higher flow rates, thus indicating that the bond between the layers of Kapton® is sufficient at these pressures and therefore at these flow rates.

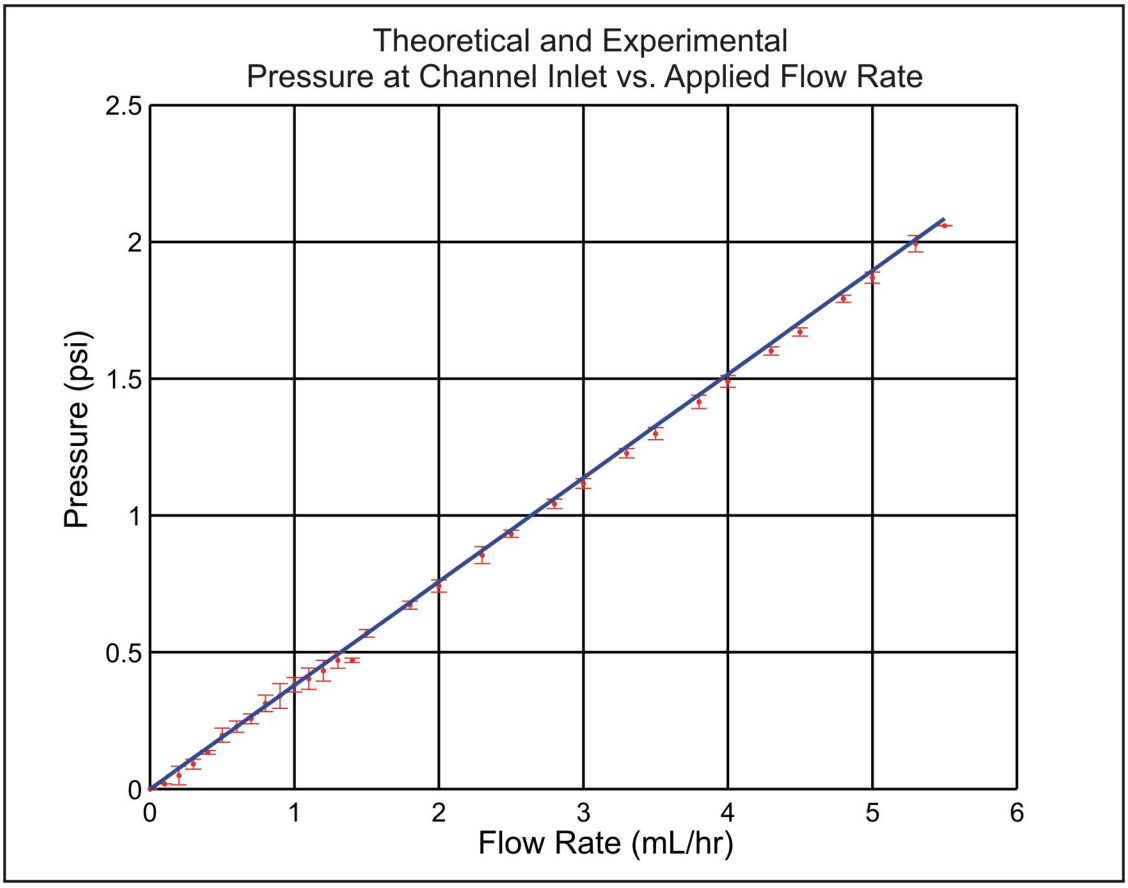

Figure 61: From the analysis of the pressure at the inlet of the microfluidic channel, the experimental data fits with the theoretical data within an error of 5.4%. Above a flow rate of 0.5 $\frac{mL}{hr}$, this error is only 2.1%.

volumetric flow rate of 95.6 $\frac{mL}{hr}$ would have to be applied. This is much greater than any flow rate expected to be used in the microfluidic system.

5.3 Data Collection Results and Discussion

5.3.1 Impedance Spectroscopy Data

As was discussed in Section 4.2.1, impedance spectroscopy measurements were collected on air, DI water, PBS, two types of dissociated cells (686LN and 686LN-M4e), and tissue samples using all eight cavities on three of the developed microfluidic systems (devices A, B, and C). After analyzing all the collected data, it was determined that not all the cavities in all three devices were functional. This could be seen by comparing the data collected for air, DI water, and PBS for a particular cavity. If no change in the data occurred between these three analytes, then it was assumed that that cavity was not functioning properly. This is due to open circuits in the metal leads between the cavities and the contact pads. Among the eight cavities on all three devices, four on device A, one on device B and two on device C were not functional. For each device, all the data for a particular analyte collected from all the functional cavities was averaged together. Additionally, for both of the cell types and the tissue samples, the data collected from all the passages was also averaged together. For instance, the data presented for the 686LN-M4e cell type for Device A is the average of 28 impedance spectroscopy measurements: seven passages and four functional cavities. The results from these measurements were compiled into Bode plots presenting the magnitude and phase data over the frequency range of 40 Hz to 10 MHz.

Figure 62 shows the average impedance spectroscopy data for all the analytes from Device A. First, it can be seen that for both the magnitude and phase responses, air and DI water have clearly distinguishable signatures from each other and from PBS and the biological analytes. At low frequencies, the impedance of air maintains a greater magnitude than for DI water, PBS, and the biologically analytes. This is expected due to the poor conductance of air. DI water also has a high resistivity, which explains why it has a greater magnitude response than for PBS and the biological analytes. However, DI water is not a perfect insulator, and therefore, it has a lower magnitude response than air. At higher

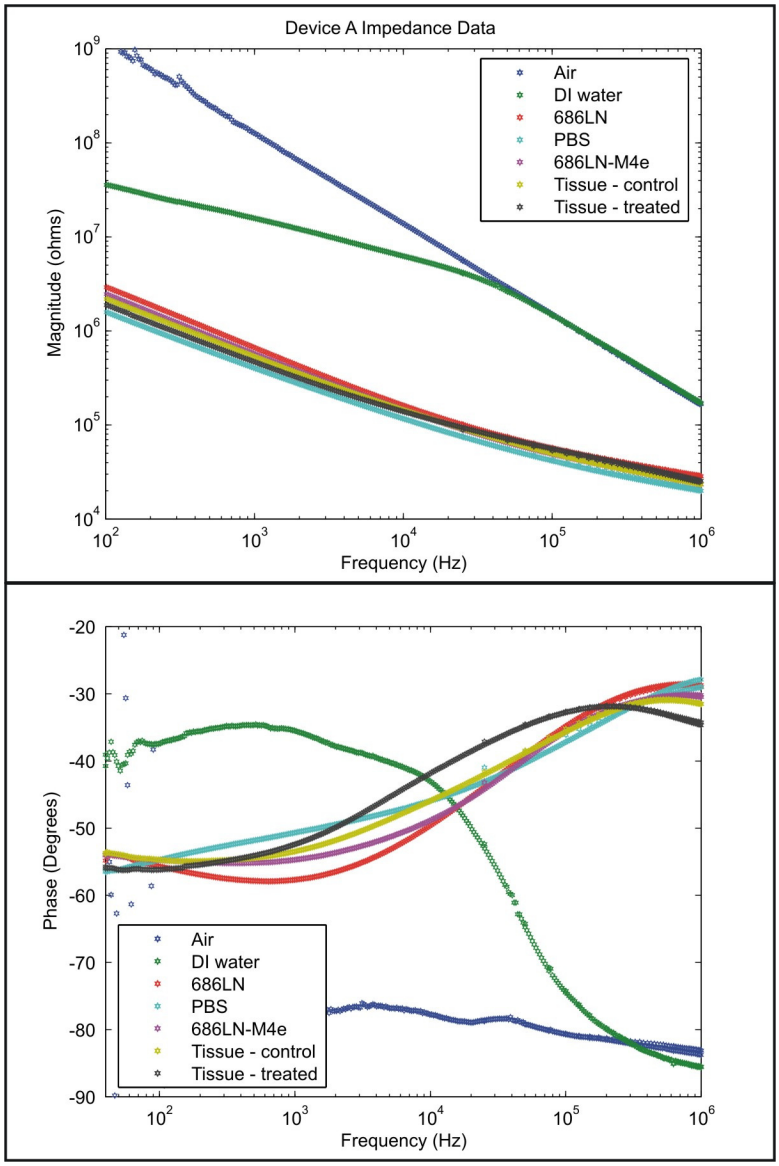

Figure 62: The impedance data (magnitude and phase) for Device A for all analytes.

frequencies, greater than approximately 30 KHz, the magnitude responses of the impedance for air and DI water come together. This is attributed to the parasitics of the device having a greater influence over the signal at higher frequencies than any material between the electrodes in the cavity. As for the phase responses, air maintains a phase close to -90° over the entire frequency spectrum. This corresponds to the phase of a capacitor, which is exactly what would be expected with only air between the two electrodes in the cavity (the parallel resistance of air is so high that it is essentially an open circuit). The phase for DI water starts to shift at around 10 KHz. Again, this is expected since the cavity with DI water can be modeled as a parallel resistor and capacitor, which produces this type of phase shift. The phase responses for PBS and the biological analytes seem to begin to drop off at a high frequency, around 1 MHz and greater. As compared to DI water, the shift at a higher frequency can be explained as the overall resistance of the material in the cavity is lower than that for DI water, which for a parallel RC circuit would produce a shift at a higher frequency. As for PBS and the biological analytes, their magnitude and phase responses are quite similar, however slight differences can be detected. The averages of the magnitude responses for the cells and tissue samples are all slightly higher than for PBS (Figure 63). For the phase responses, while the values are all close along the frequency spectrum, the signatures of the phase responses differ. At lower frequencies, PBS maintains a steady increase whereas the cells and tissue samples remain constant or even decrease slightly at around 1 kHz before beginning to climb. Also, at the higher frequencies, the cells and tissue samples drop to a slightly lower phase than does PBS. These results only show a very small difference between the 686LN and 686LN-M4e cell lines (Figure 64). At low frequencies between 100 Hz and 10 kHz, the 686LN cells exhibit a drop in phase whereas the 686LN-M4e cells remained steady. For the tissue samples, there is no significant difference between the control sample and the treated sample in the signatures of either the magnitude or phase responses (Figure 65).

The average impedance spectroscopy data for all the analytes in Device B are shown in Figure 66. First, as compared to the results from Device A, these results are quite different. However, at closer inspection, similar trends between the two data sets do appear. Although

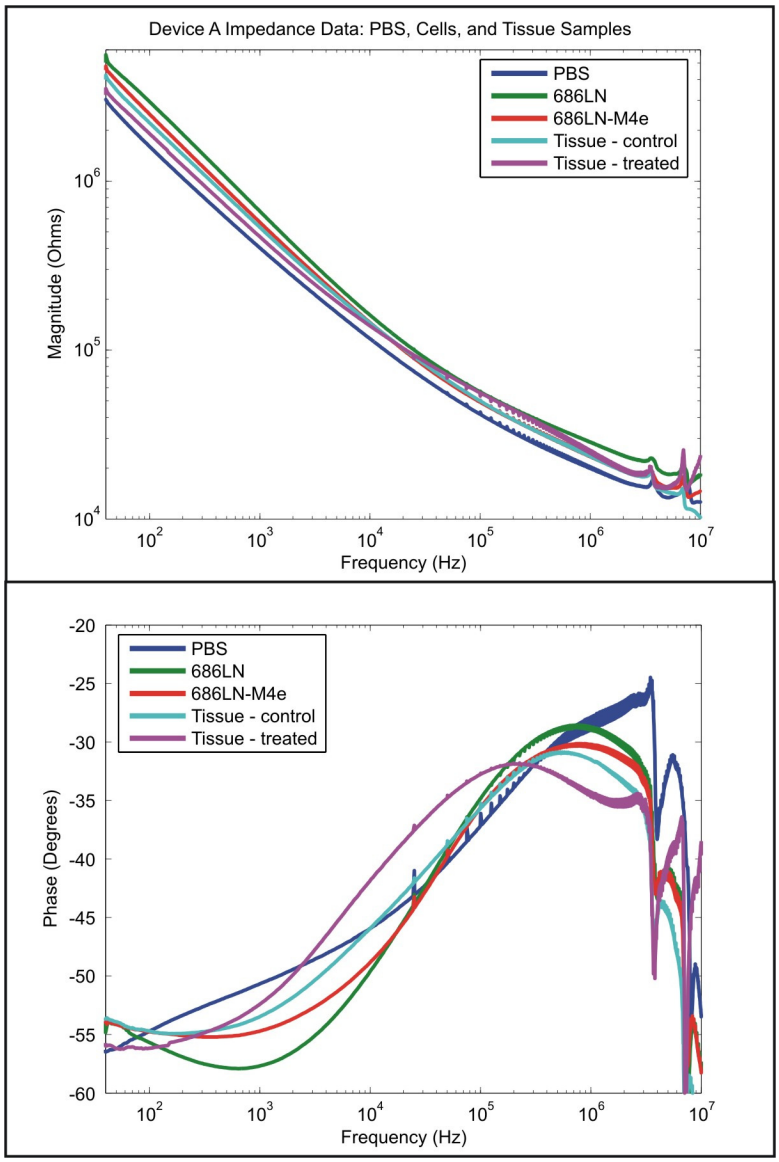

Figure 63: The phase data for Device A shows differences in the signatures between PBS and the biological samples.

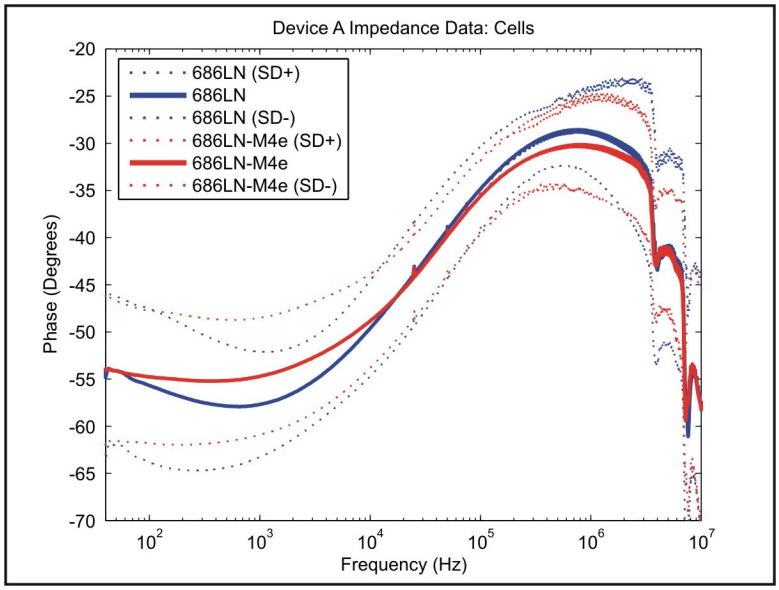

Figure 64: The phase data for Device A shows that a small difference in the signatures between the two cell types analyzed exists at low frequencies. The dotted lines indicate the standard deviation of the data.

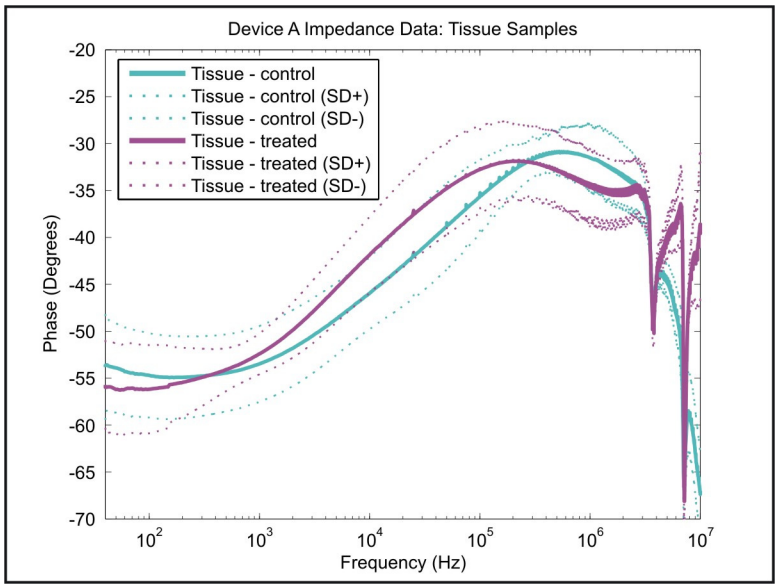

Figure 65: The phase data for Device A shows no significant difference in the signatures of the control and treated tissue samples. The dotted lines indicate the standard deviation of the data.

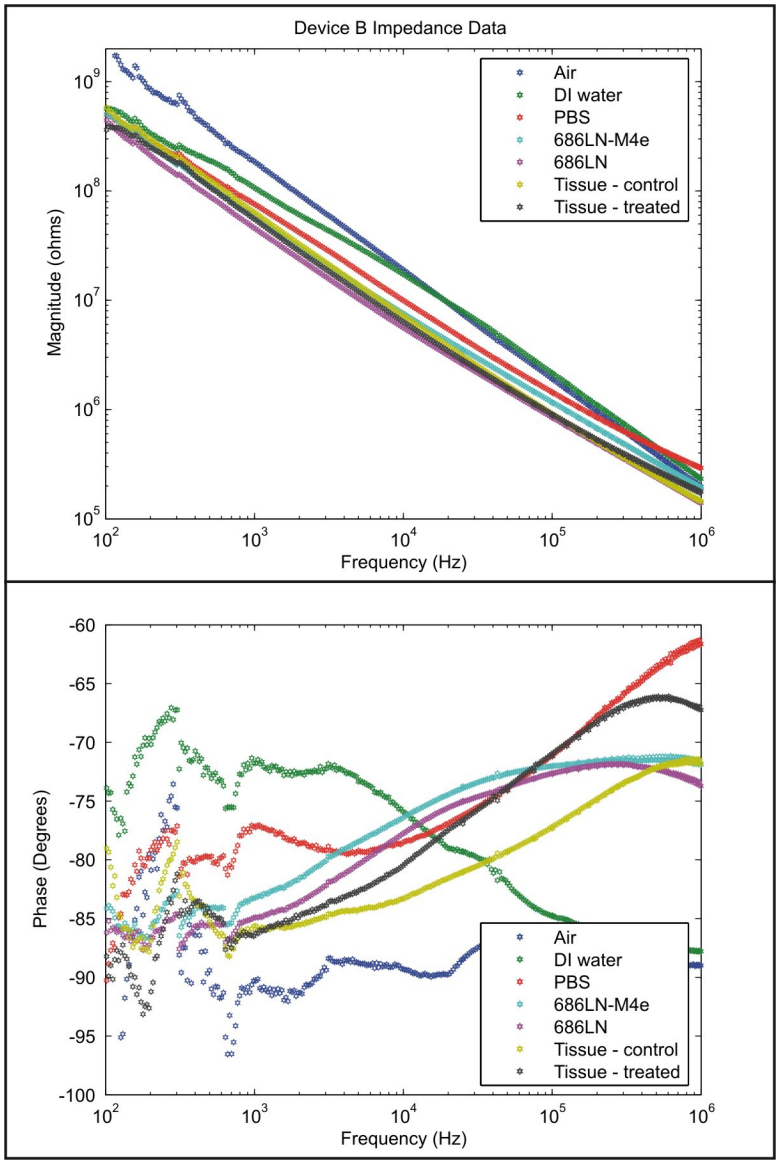

Figure 66: The impedance data (magnitude and phase) for Device B for all analytes.

all the magnitude responses are clustered at a high magnitude (similar to the magnitude for only air in Device A), the relative differences between air, DI water, and the other materials are still there. At low frequencies, the magnitude for DI water is lower than that for air and is still slightly higher than the other analytes. As the frequency increases, as was the case in Device A, the magnitude for DI water merges with that for air. One difference in the magnitude responses between Device A and Device B is for PBS and the biological analytes. In Device A, the magnitude response for PBS was slightly lower than that for the cells and tissue samples. However, in Device B, PBS maintains a slightly higher magnitude response than what was found for both cell types and the tissue samples. The phase responses for all the analytes in Device B are also clustered together at lower phase values, but as was the case for the magnitude responses, trends among the different analytes are similar to those from Device A. Again, air maintains a steady phase close to $-90°$ over the entire frequency spectrum. In addition, the phase response for DI water begins higher and shifts at around 10 kHz. As with Device A, the phase responses for PBS and the biological analytes are all close along the frequency spectrum, however the signatures of those responses again differ (Figure 67). At low frequencies, the phase response of PBS is slightly higher than for the other analytes, and it remains steady with a small drop starting at around 1 kHz before continuing to increase at around 5 kHz. The phase responses for the cells and tissue samples also remain steady at low frequencies but increase starting at around 1 kHz, and they are steady again at around 50 kHz. At higher frequencies, greater than approximately 500 kHz, the phase response for PBS remains higher than those for the cells and tissue samples. As for the two cell lines, these results do not clearly show any difference between the 686LN and 686LN-M4e cell lines (Figure 68). For the tissue samples, the treated tissue appears to have a greater change in its phase response than does the control tissue sample starting at around 10 kHz (Figure 69); however, given the standard deviation from the data sets of both samples, their signatures are similar enough that it cannot be definitively said that they are distinguishable.

Figure 70 shows the average impedance spectroscopy data for all the analytes from Device C. These results match much more closely to Device A than did Device B. The

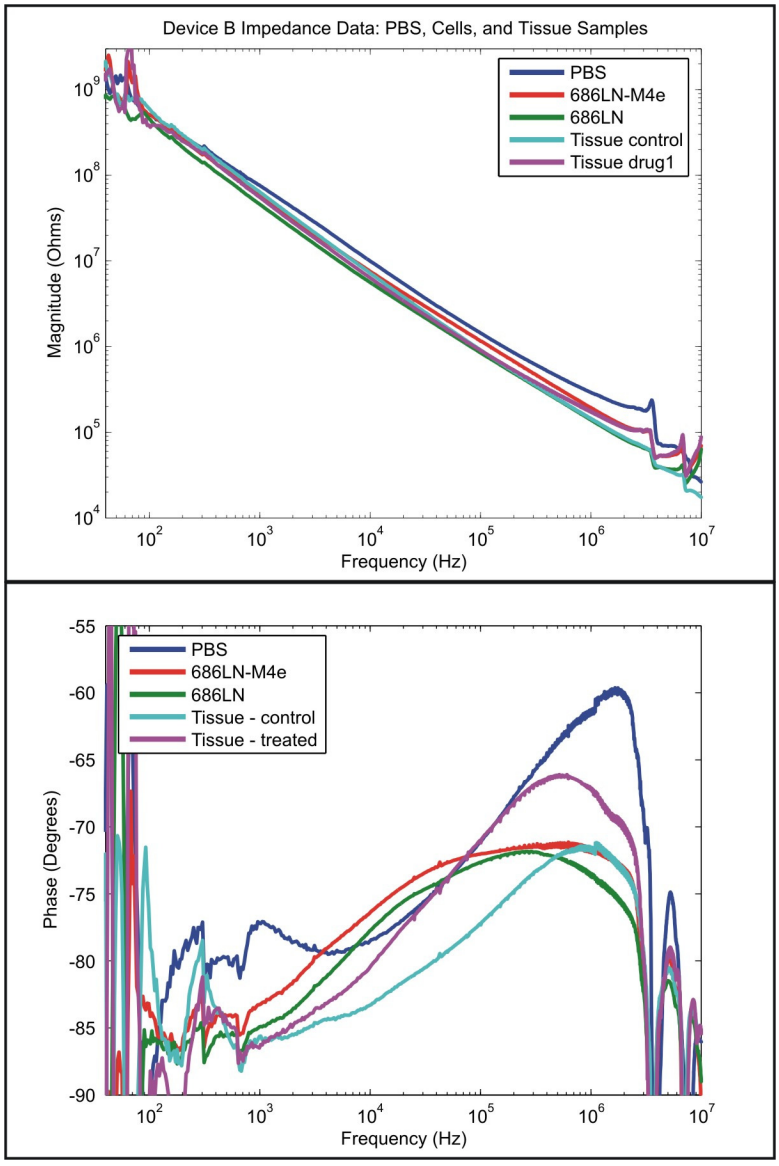

Figure 67: The phase data for Device B shows differences in the signatures between PBS and the biological samples.

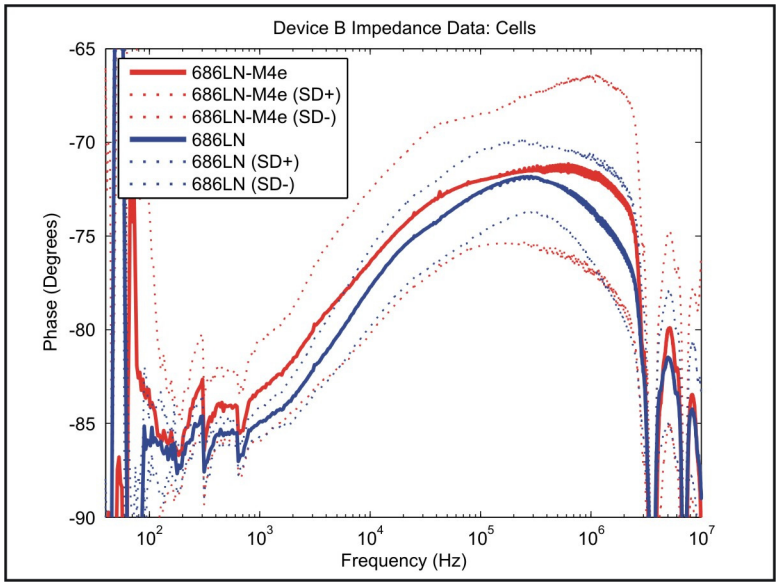

Figure 68: The phase data for Device B does not clearly show any difference between the two cell types analyzed. The dotted lines indicate the standard deviation of the data.

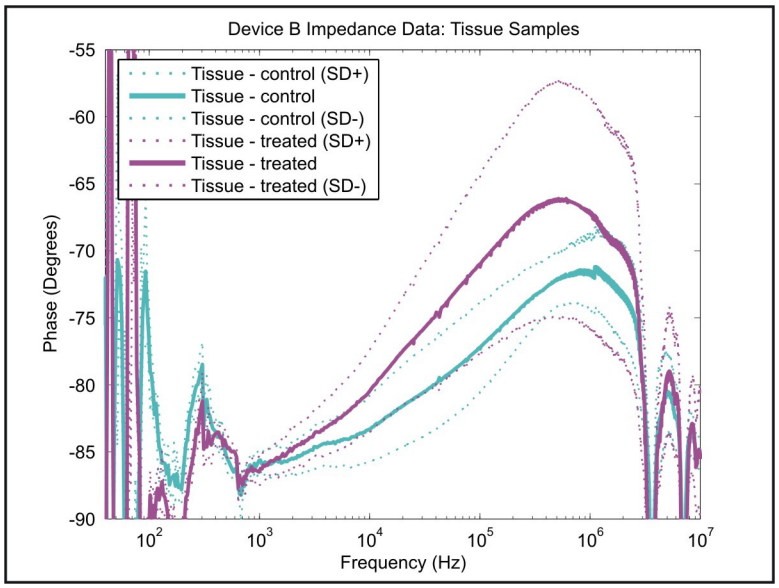

Figure 69: The phase data for Device B shows a possible difference in the signatures between the control and treated tissue samples. However, within the standard deviation, a significant difference is not distinguishable. The dotted lines indicate the standard deviation of the data.

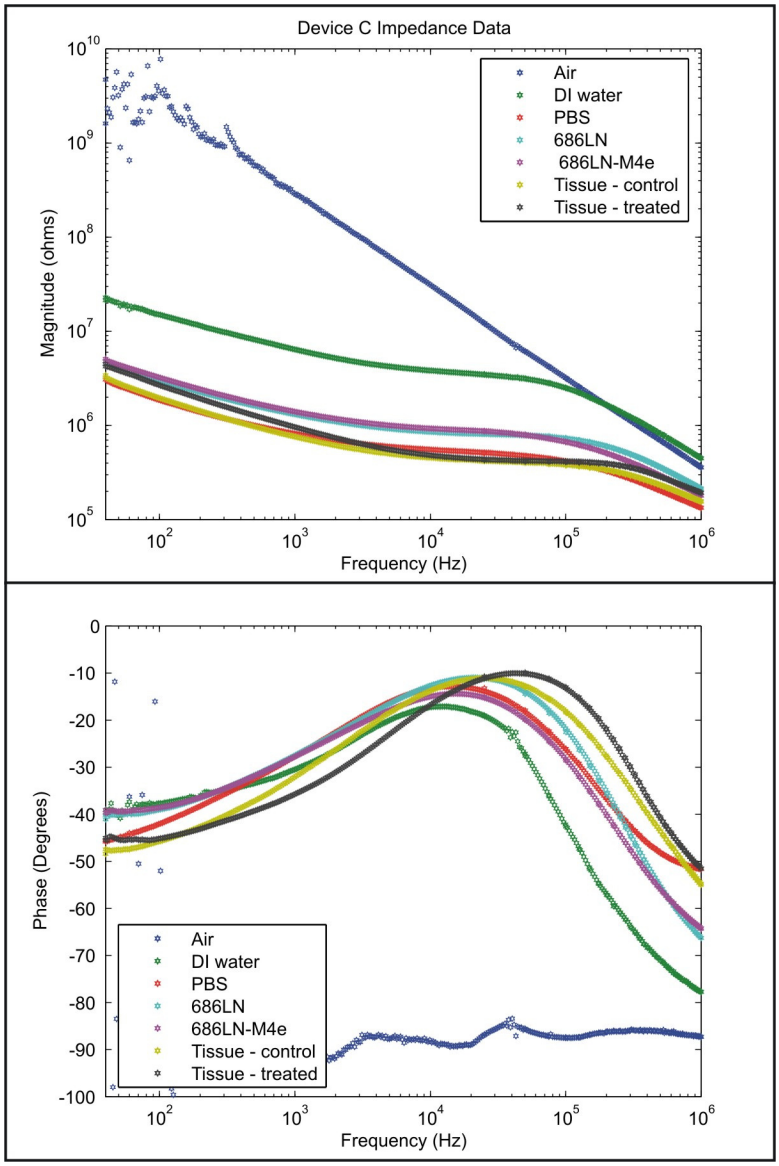

Figure 70: The impedance data (magnitude and phase) for Device C for all analytes.

magnitude responses for all the analytes do follow the same trends that were seen in Device A: the magnitude of air remains high; DI water is between air and the other analytes before merging with air at higher frequencies; and PBS has a slightly lower magnitude response than the cells and tissue samples. However, the phase responses between Devices A and C do differ. Air still maintains a steady phase close to -90° over the entire frequency spectrum. Yet, the phase response for DI water is now close to that for PBS and the biological analytes. This increase in frequency where the phase shift takes place for DI water can be explained by different device parasitics between the two devices. Nevertheless, the behavior of the phase responses for PBS and the biological analytes still varies as it did for Device A (Figure 71). At lower frequencies, PBS maintains a steady increase whereas the cells and tissue samples exhibit a constant phase before beginning to climb at around 100 Hz. Also, at the higher frequencies, the cells and tissue samples drop to lower phase values than does PBS, which starts to steady off at around 300 kHz. As was the case with Device B, this device does not clearly show any difference between the 668LN and 686LN-M4e cell lines (Figure 72) or between the control and treated tissue samples (Figure 73).

For all three devices, by considering the characteristic impedance spectra for both the magnitude and phase responses, the presence of air, DI water, PBS, or one of the biological analytes in the analysis cavity can be determined. However, these results do not show significant differences between the different cell types or between the control and treated tissue samples, except partially with Device A. This area of detection can possibly be improved by using smaller analysis cavities and by using a more precise manner of dispensing the biological sample into the cavity. Although the volume dispensed for each test remained constant (1.2 μL), the number of cells in each sample and the density of cells in the cavity was was not controlled. The tissue samples provided a more uniform sample to be placed in the cavity, but again, how tightly filled the cavity was with the tissue sample was not controlled. In addition, these were the only cell lines used in the testing of the microfluidic systems, and it is possible that other cell lines would produce different results.

The differences between the devices are attributed to variations occurring during fabrication. Since the three devices were manufactured at different times, and since certain parts

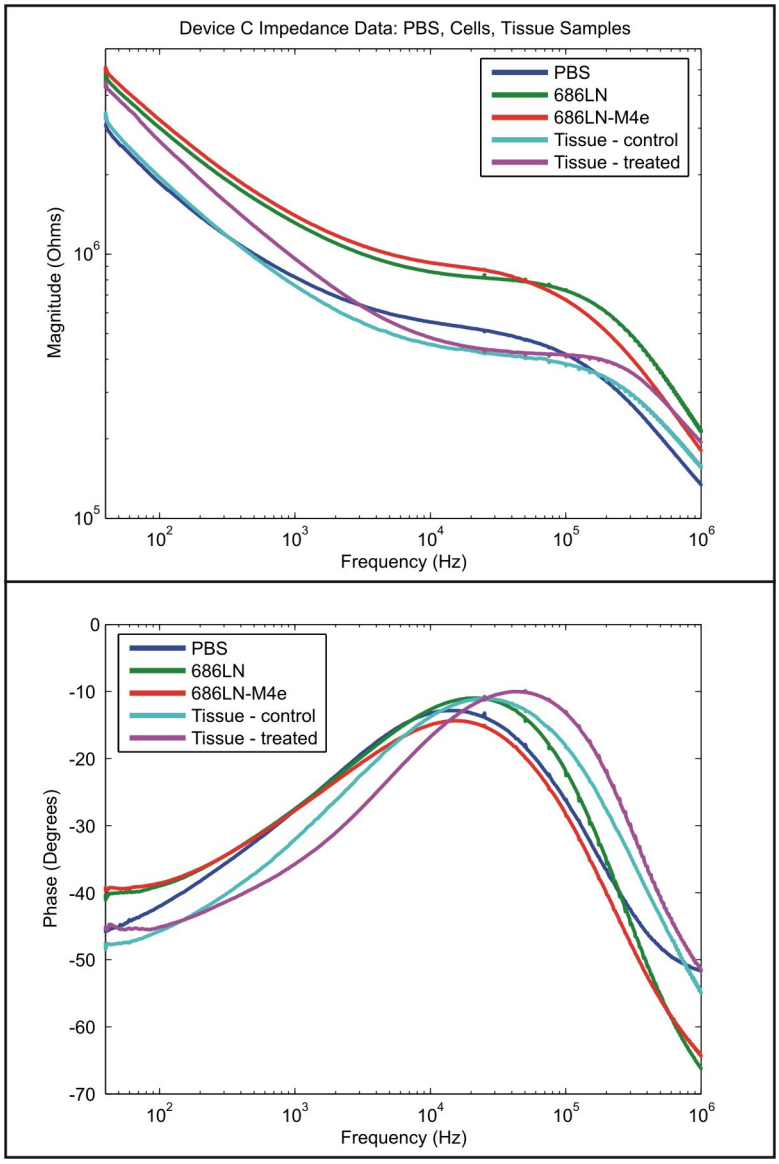

Figure 71: The phase data for Device C shows differences in the signatures between PBS and the biological samples.

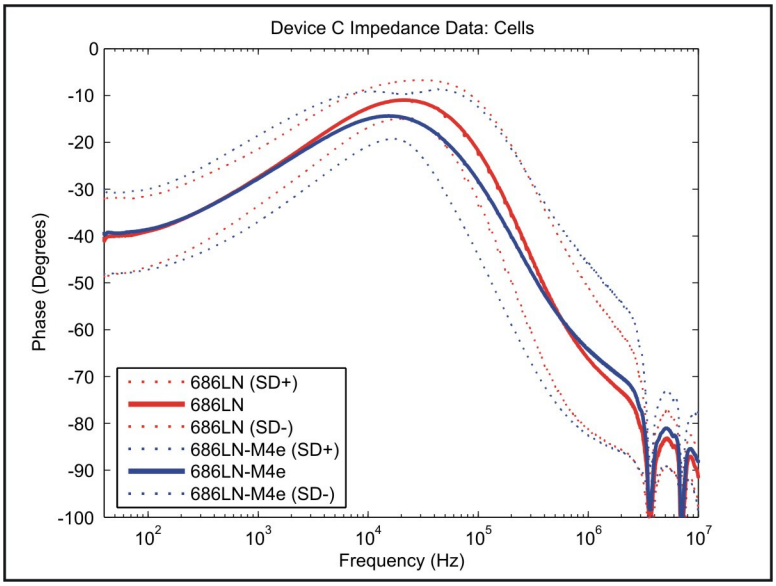

Figure 72: The phase data for Device C does not clearly show any difference between the two cell types analyzed. The dotted lines indicate the standard deviation of the data.

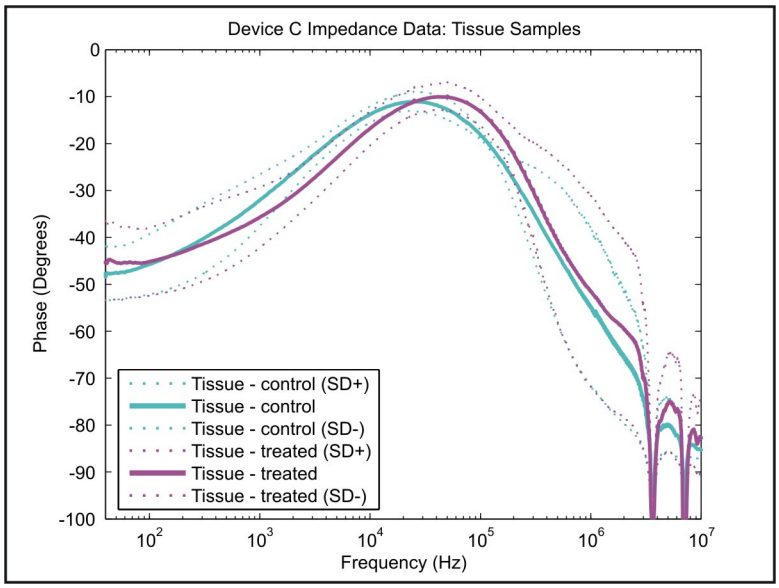

Figure 73: The phase data for Device C shows no significant difference in the signatures of the control and treated tissue samples. The dotted lines indicate the standard deviation of the data.

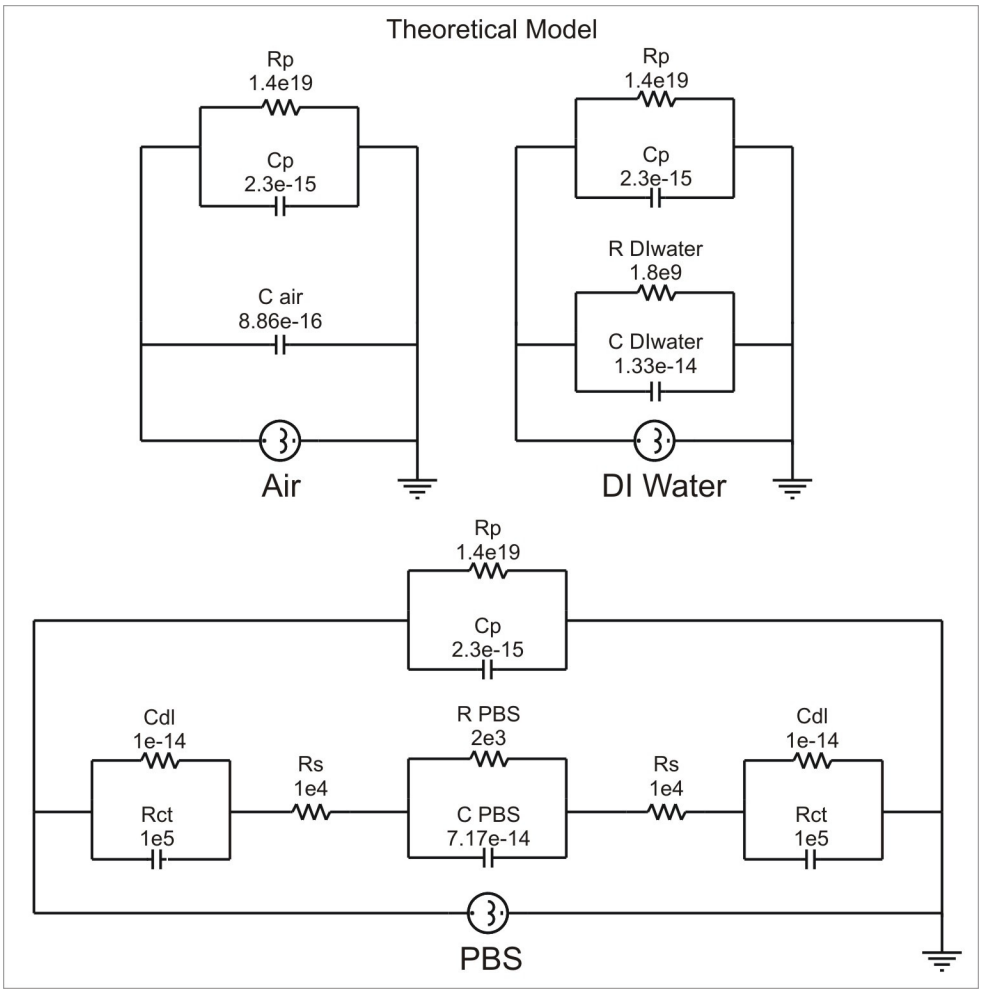

Figure 74: Re-displayed from Chapter 2: The circuit models for the microfluidic system with air, DI water, and PBS inside the analysis cavities.

of the fabrication process require adjustments to be made by hand, differences in the three devices are not unexpected. The possible differences between devices include: the position of the metal leads with respect to the analysis cavity; the presence of air pockets between Kapton® layers from heat staking; and the quality of the metal leads from evaporation or sputtering and the metal interconnects between the contact pad and electrical wire. Nevertheless, the results presented here do show that these devices have the ability to repeatedly characterize and differentiate certain analytes.

In addition to analyzing the results from each device, the results were compared to the electrical model discussed in Chapter 2, for which the circuit diagram and magnitude and phase responses are shown again here in Figures 74 and 75. As has already been

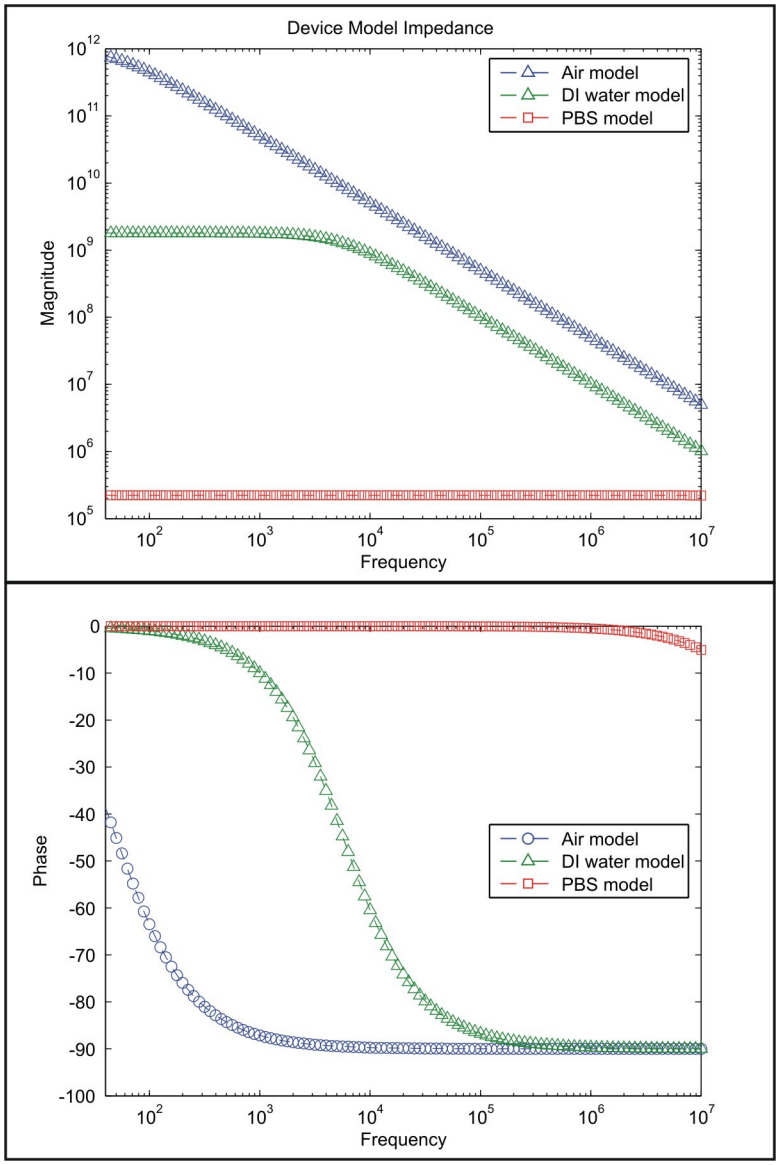

Figure 75: Re-displayed from Chapter 2: The impedance data (magnitude and phase) for the theoretical circuit model for air, DI water, and PBS in the analysis cavity over a frequency range of 40 Hz to 10 MHz.

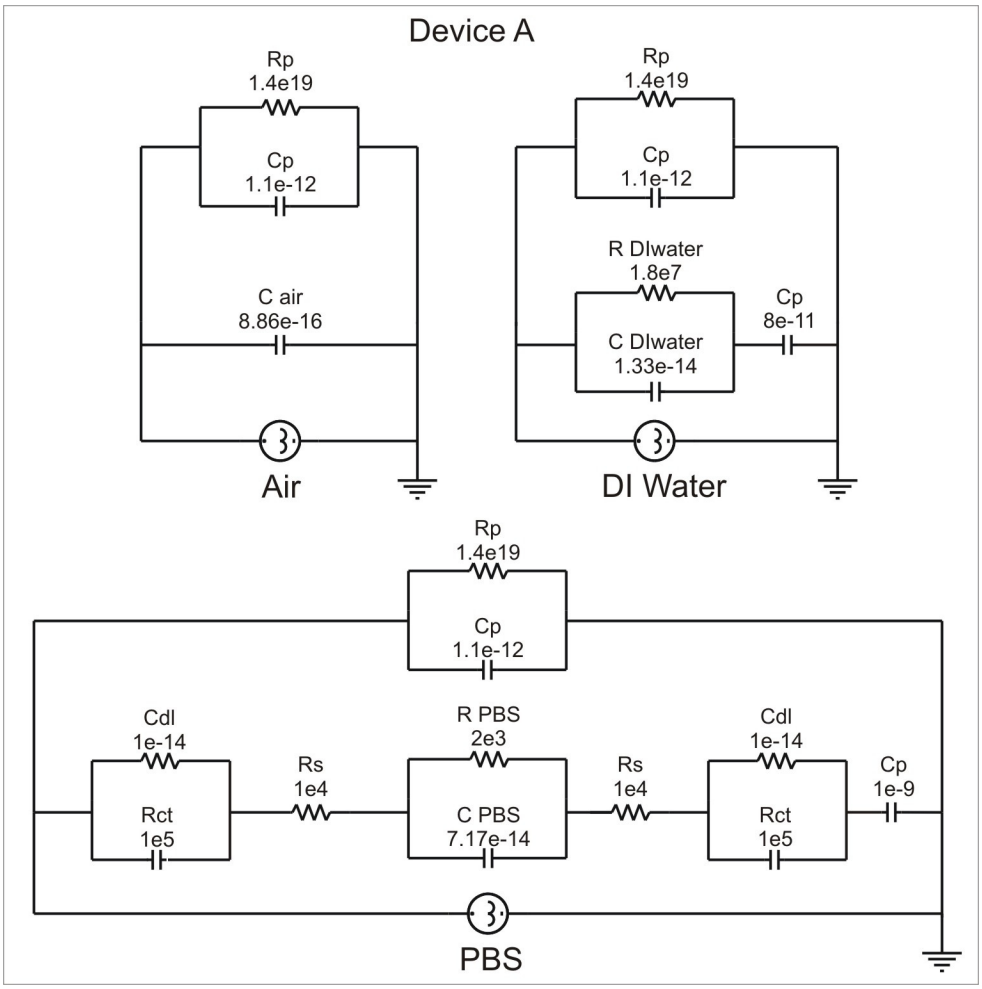

Figure 76: Adjusted circuit model for Device A for air, DI water, and PBS.

discussed, similar trends are seen in the magnitude and phase responses for each analyte from the three devices. The overall magnitude decreases from air to DI water to PBS, and the phase shifts to higher frequencies as the analytes become more conductive as was expected from Chapter 2. However, the values of the data do not match from device to device or from each device to the electrical model. To account for the differences between devices, the portion of the circuit model shown in Figure 74 relating to the device parasitics and the electrode polarizations has been altered for each device. New circuit models and corresponding magnitude and phase plots for each device are shown in Figures 76, 77, 78, 79, 80, and 81.

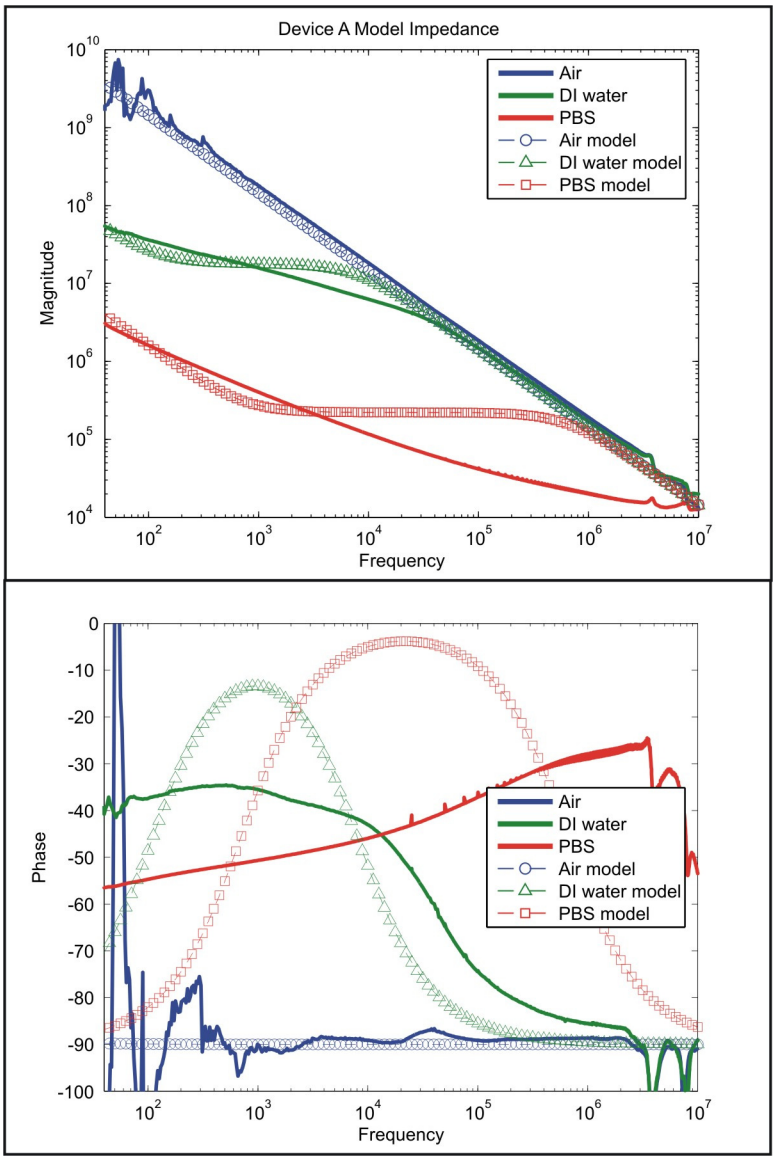

Figure 77: Experimental and model impedance data for Device A for air, DI water, and PBS.

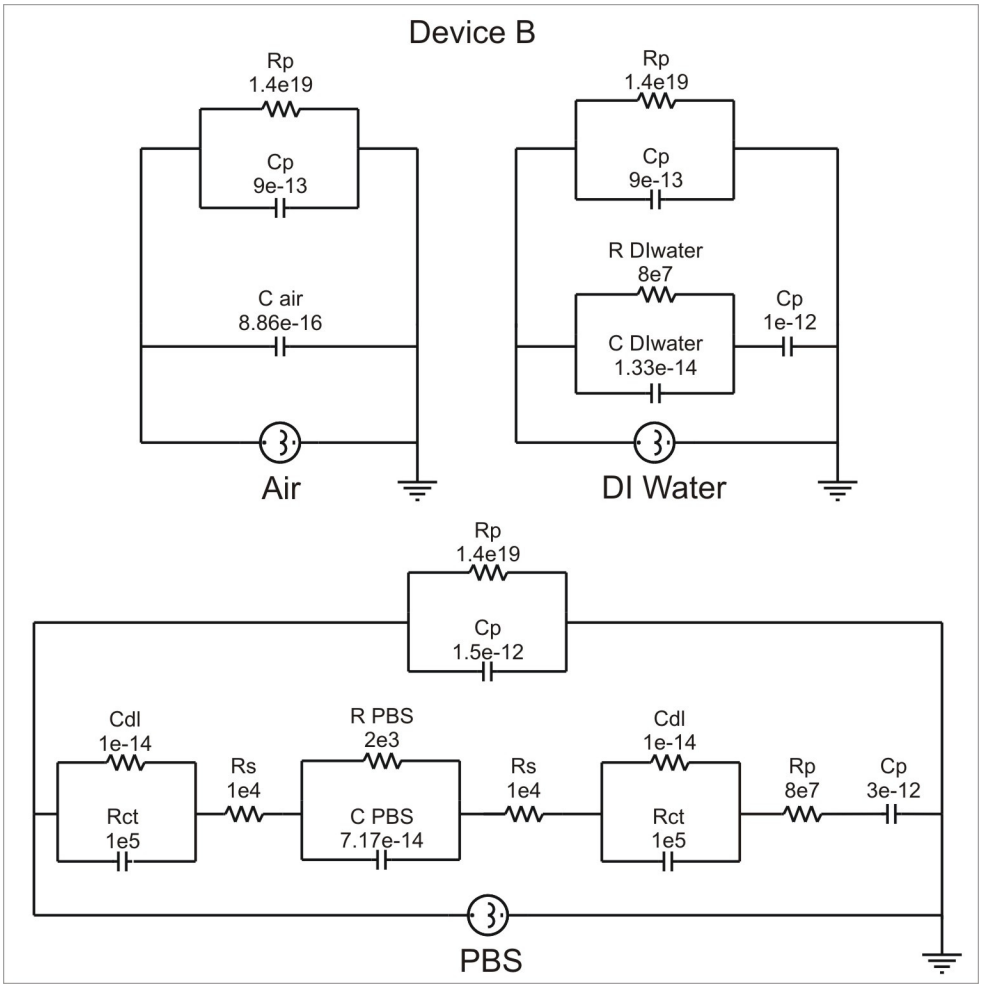

Figure 78: Adjusted circuit model for Device B for air, DI water, and PBS.

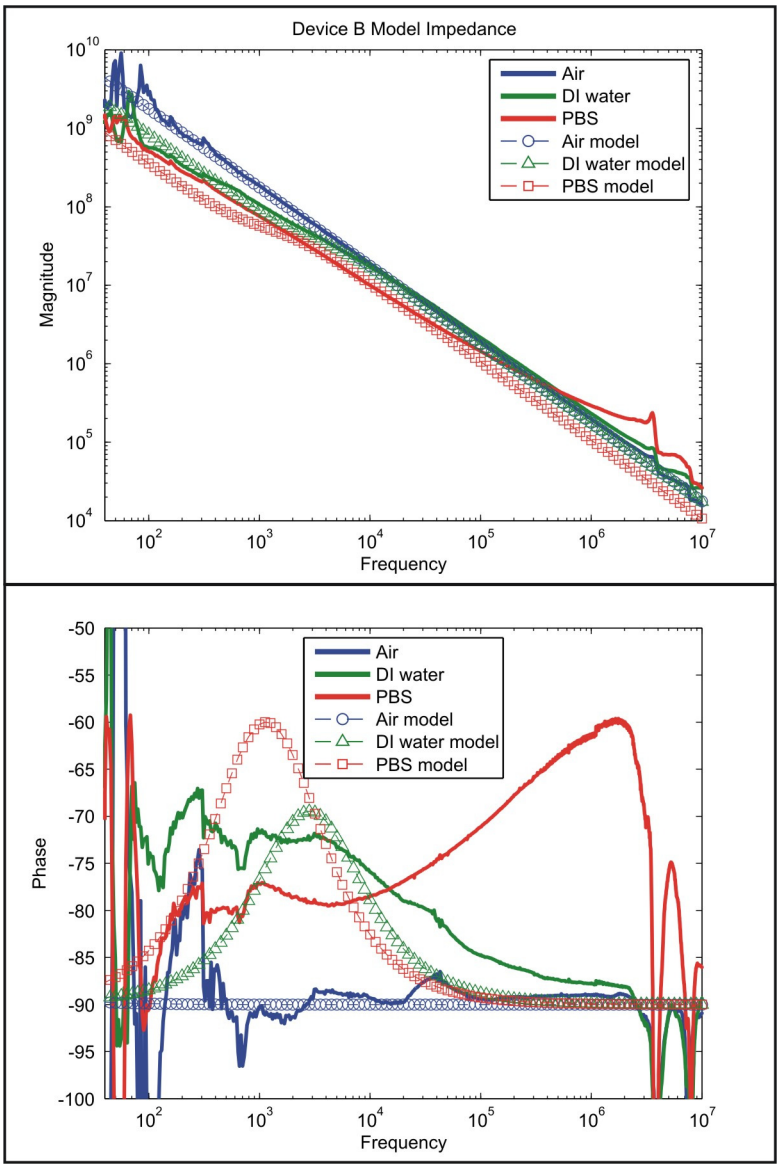

Figure 79: Experimental and model impedance data for Device B for air, DI water, and PBS.

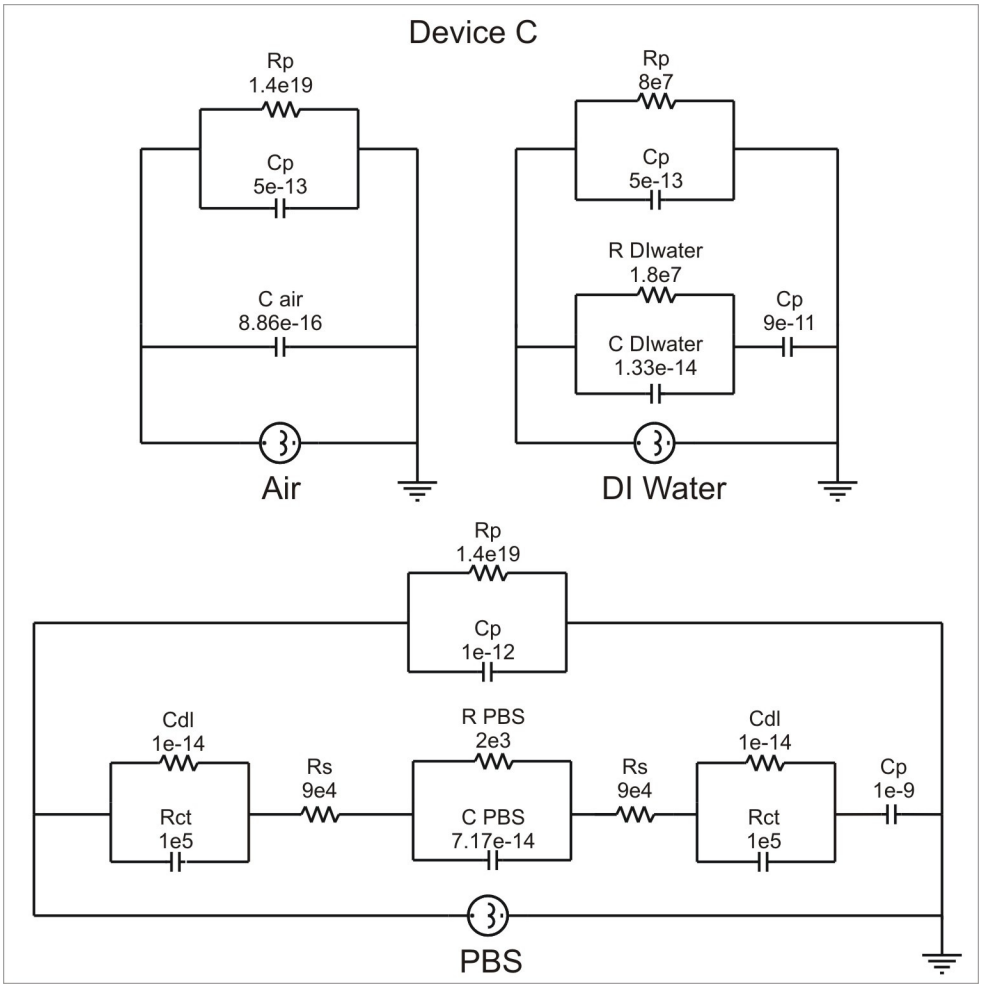

Figure 80: Adjusted circuit model for Device C for air, DI water, and PBS.

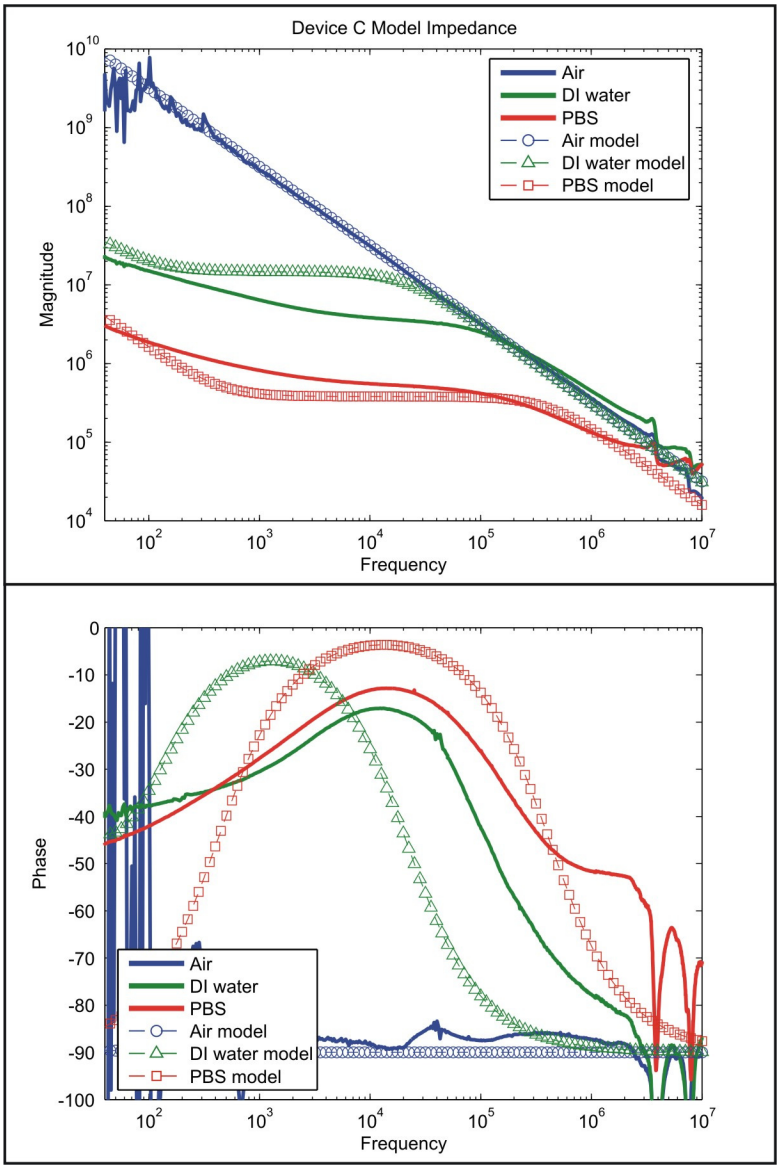

Figure 81: Experimental and model impedance data for Device C for air, DI water, and PBS.

For Device A (Figures 76 and 77), additional parasitics were included as a series capacitance to the analysis cavity for both the DI water and PBS circuits (8×10^{-11} F and 1×10^{-9} F respectively), and the original parasitic capacitance for all three models was increased from 2.3×10^{-15} F to 1.1×10^{-12} F. The value of the resistance for the DI water itself also had to be altered. It was decreased from 1.8×10^{9} Ω to 1.8×10^{7} Ω. This could be due to impurities in the DI water causing the sample to be slightly more conductive than ideal DI water.

As with Device A, Device B (Figures 78 and 79) also required additional capacitors in series to the analysis cavity for both the DI water and PBS circuits (1×10^{-12} F and 3×10^{-12} F respectively). The value of the resistance for the DI water was also decreased to 8×10^{7} Ω, and an additional series resistance to account for the unexpectedly high values in the magnitude response was added in the PBS circuit. The original parallel capacitance parasitic for all three models was again increased from 2.3×10^{-15} F to 9×10^{-13} F for air and DI water and to 1.5×10^{-12} F for PBS.

The adjustments to the circuit for Device C (Figures 80 and 81) included an additional series capacitance for both the DI water and PBS circuits (9×10^{-11} F and 1×10^{-9} F respectively) and a decrease in the resistance for DI water from 1.8×10^{9} Ω to 1.8×10^{7} Ω. The original parasitics were also changed for all three circuit models. For air and DI water, the parasitic capacitance was increased from 2.3×10^{-15} F to 5×10^{-13} F; for DI water, the parasitic resistance was decreased to 8×10^{7} Ω; and for PBS, the parasitic capacitance was increased to 1×10^{-12} F. Device C also required an increase in the series resistance of the polarization circuits from 1×10^{4} Ω to 9×10^{4} Ω.

Circuit models relating to a cluster of cells and a tissue sample placed in the analysis cavity were also developed based on the experimental results obtained with Device C. The circuit model with cells is shown in Figure 82 with the corresponding magnitude and phase plots shown in Figure 83. Since the dissociated cells are suspended in a PBS solution, this model is derived from the model of just PBS in the analysis cavity for Device C (Figure 80). For this model, there are two parallel RC circuits representing the material inside the cavity. The first is for the cluster of cells, and the second is a pathway for leakage current that

may pass through the carrier solution (PBS). The R and C values for the leakage pathway originated from values for PBS in the cavity and were then modified to account for the fact that PBS is only present in a fraction of the cavity when a cluster of cells is present. These values and those for the resistance and capacitance of a cluster of cells were adjusted until the model matched as closely as possible to the experimental data, which resulted in: $R_{leak} = 2 \times 10^8$ Ω, $C_{leak} = 7.17 \times 10^{-15}$ F, $R_{cells} = 5 \times 10^5$ Ω, and $C_{cells} = 1 \times 10^{-12}$ F. The electrode polarization circuits were retained in this model since the electrodes were still in contact with PBS because the cells were not tightly packed in the cavity. The magnitude and phase plots in Figure 83 compare the model and experimental data for both cells and PBS in the analysis cavity. For both the experimental and model data the magnitude response for the cells is greater than that for the PBS alone, which is characteristic of the greater resistance in the analysis cavity caused by the cluster of cells. The phase response from the model with the cells leads that for the PBS due to a greater capacitance caused by the cluster of cells.

The circuit model with a tissue sample in the analysis cavity is shown in Figure 84, and the corresponding magnitude and phase plots are shown in Figure 85. As was the case for the circuit model with a cluster of cells in the analysis cavity, the model with a tissue sample in the cavity also stems from the PBS model in Figure 80. Since there is less carrier solution in the cavity with a tissue sample as opposed to with a cluster of cells, the leakage pathway is less conductive for this model. Another difference between the model for a cluster of cells and the one with a tissue sample is that the electrode polarization is less resistive since a tissue sample can be fit more tightly into the cavity than can the cells. These issues were considered, and the individual parameters were adjusted until the model matched as closely as possible to the experimental data, which resulted in: $R_{leak} = 2 \times 10^{10}$ Ω, $C_{leak} = 7.17 \times 10^{-17}$ F, $R_{cells} = 3 \times 10^5$ Ω, $C_{cells} = 7.17 \times 10^{-11}$ F, and R_s for each polarization circuit = 100 Ω. The magnitude and phase plots in Figure 85 compare the model and experimental data for both a tissue sample and PBS in the analysis cavity. The magnitude response for both the experimental and model data show similar trends for the tissue samples and PBS. The phase response for the model data does show additional effects

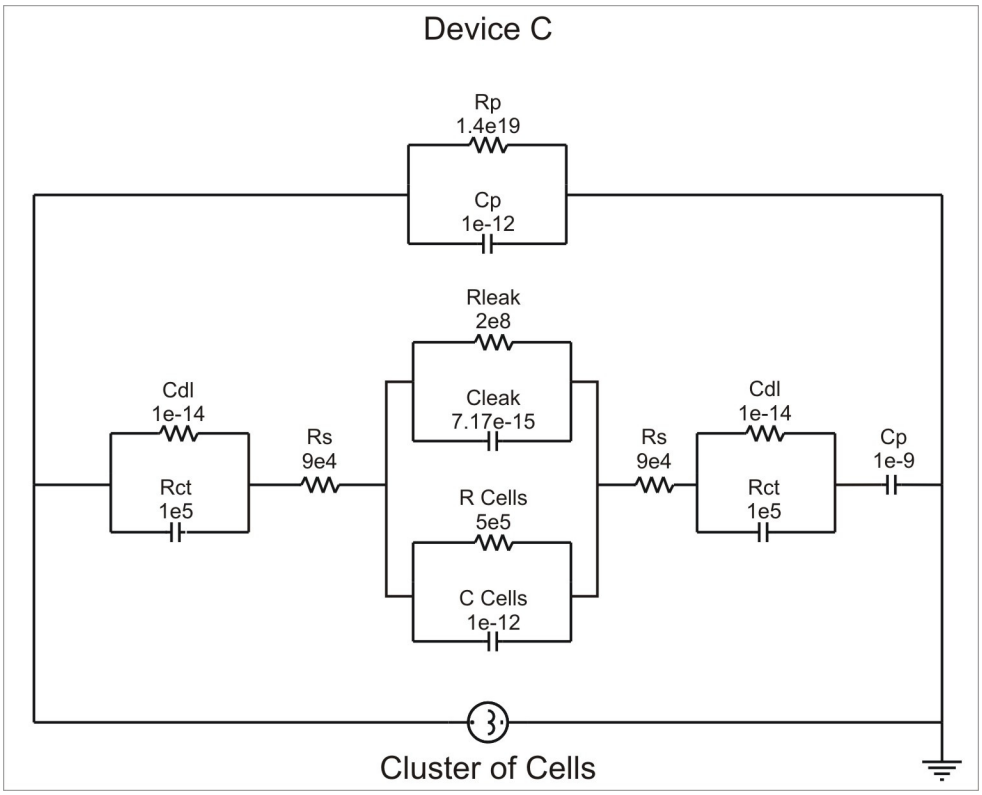

Figure 82: Adjusted circuit model for Device C for a cluster of cells inside the analysis cavity.

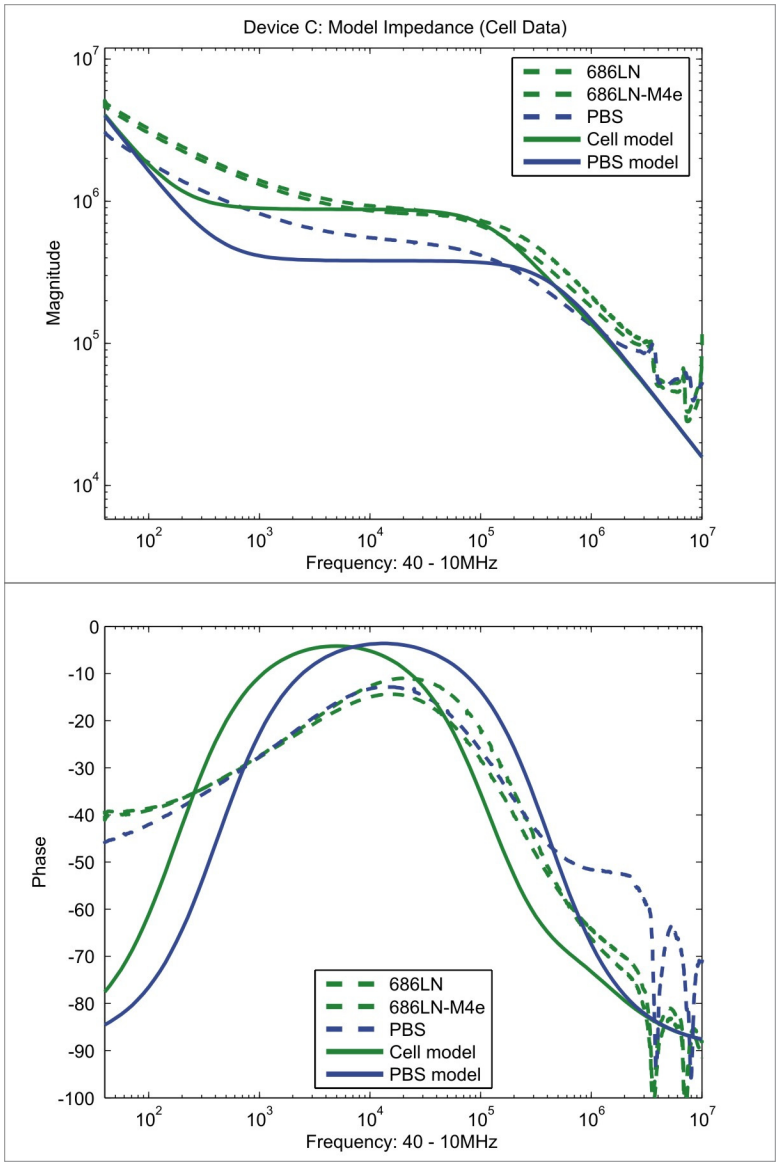

Figure 83: Experimental and model impedance data for Device C for PBS and a cluster of cells inside the analysis cavity.

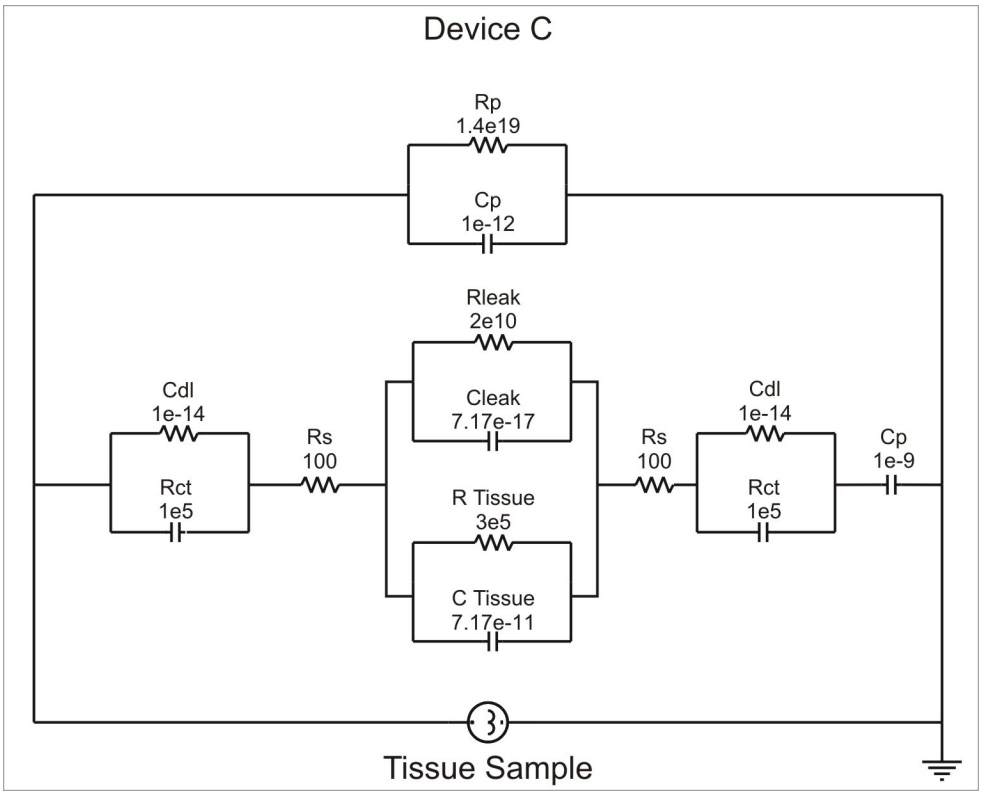

Figure 84: Adjusted circuit model for Device C for a tissue sample inside the analysis cavity.

not found in the experimental data. However, both the experimental and model responses show a slight lag from PBS to the tissue samples at higher frequencies.

Although the circuit models for all three devices correspond to the collected data plots much more closely than the original circuit model from Section 2.2.2, discrepancies (especially in the phase responses) still exist. A more sophisticated circuit model is necessary to address this. Still, with the simplified circuit models, it is apparent how differences between devices (possibly caused during fabrication) can affect the impedance spectroscopy results. However, even with the differences in device parasitics, the same trends in impedance responses for the various analytes were still apparent from device to device. This is an indication that regardless of the varying device parasitics, this microfluidic system can provide a means for the characterization and differentiation of various analytes through impedance spectroscopy.

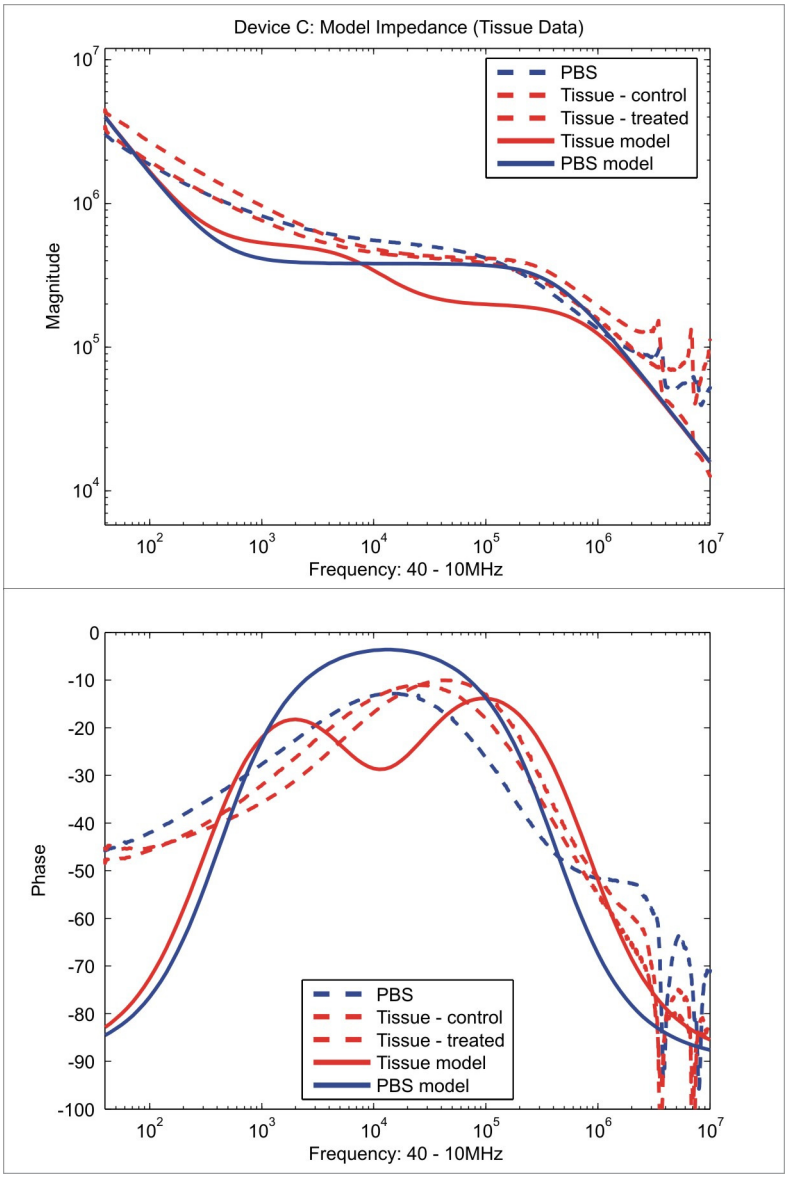

Figure 85: Experimental and model impedance data for Device C for PBS and a tissue sample inside the analysis cavity.

5.3.2 Giga-seal Testing

Giga-seal testing was performed with fluorescently-labeled 1 μm and 10 μm diameter polystyrene microbeads and dissociated cells using four of the developed microfluidic systems (D, E, F, and G) as was described in Section 4.2.2.

Preliminary testing was performed with microfluidic systems from the third design version discussed in Section 2.1.3 (Figure 13): eight, large-diameter (240 μm) analysis cavities, large and small alignment features, and a single fluidic channel controlling all eight cavities. The testing showed that a single fluidic channel provided too little control over any particular analysis cavity. Since the electrodes for only one cavity are connected to the digital multimeter at one time, trying to monitor all the cavities for possible signals was not an option. Placing beads or cells in only one cavity at a time was a possible solution, but with all the other via holes open to the same fluidic channel, controlling only that specific cavity was still a problem.

To address this lack of control over individual cavities, the fourth design version of the microfluidic system was developed (Figure 14): eight, large-diameter (240 μm) analysis cavities, large and small alignment features, but with four separate fluidic channels each with access to only two analysis cavities. Giga-seal testing proved to be much more feasible with this approach.

Before testing with the dissociated cells, the fluorescently labeled microbeads were used to test the ability of using negative pressure through the via hole to control and capture a particle. With the solution of 1 μm diameter blue fluorescently-labeled beads, video was captured showing the flow of beads into and out of the via hole corresponding to negative and positive pressure formed in the microfluidic channel, which verified the ability to control particles in the analysis cavity. The ability to capture a particle onto the via hole was verified with the 10 μm diameter red fluorescently-labeled beads. Again, video was recorded showing the movement of the beads towards and away from the via hole in response to negative and positive pressure.

With the fluidic functionality of the system verified, achieving the giga-seal with both the 10 μm diameter beads and dissociated 686LN-M4e cells was attempted. Figure 86 shows

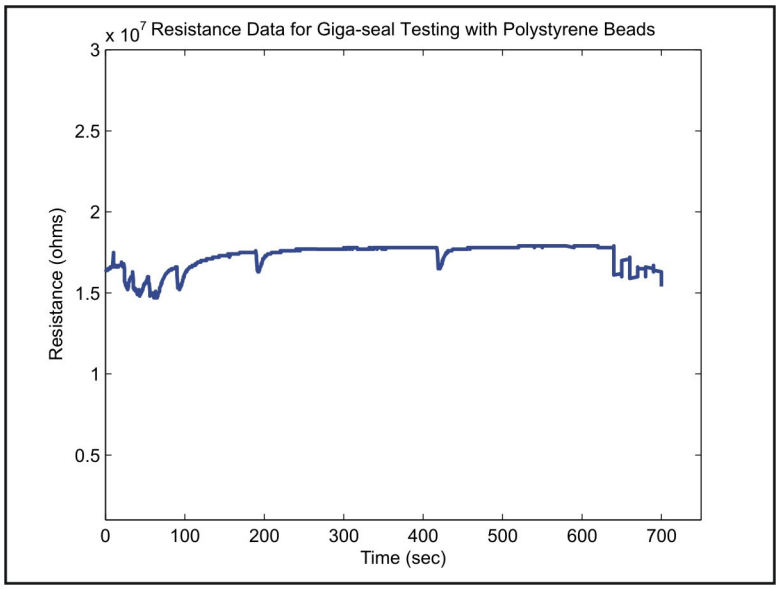

Figure 86: The resistance data collected during giga-seal tests with polystyrene beads in the analysis cavities showed an average resistance with no beads on the via hole of 17.5 MΩ. There is also no significant increase in the resistance throughout the test during which the bead was pulled against the cavity multiple times using negative pressure inside the microfluidic channel.

a sample of the data recorded during trapping and releasing the polystyrene beads onto the via hole. The data shows no significant increase in resistance throughout the test during which the bead was pulled against the cavity multiple times for periods of at least 5 seconds or more. This test was repeated for beads in four analysis cavities, all with similar results.

As shown in Figure 86, the average resistance between the fluidic channel electrode and one of the cavity electrodes when the via hole is open and the channel and analysis cavity are filled with PBS is 17.5 MΩ. A theoretical analysis calculating this resistance results in an open-via hole resistance of 1.6 MΩ. The difference between the theoretical and experimental open-via hole resistances is attributed to differences between the designed dimensions and the actual dimensions of the microfluidic system. The theoretical calculation used the following design parameters:

$\rho_{PBS} = 0.2\ \Omega\cdot\text{m}$,

analysis cavity diameter $= 240\ \mu\text{m}$,

analysis cavity depth $= 101.6\ \mu\text{m}$,

cavity electrode cross-sectional area $= 30\ \mu\text{m}^2$,

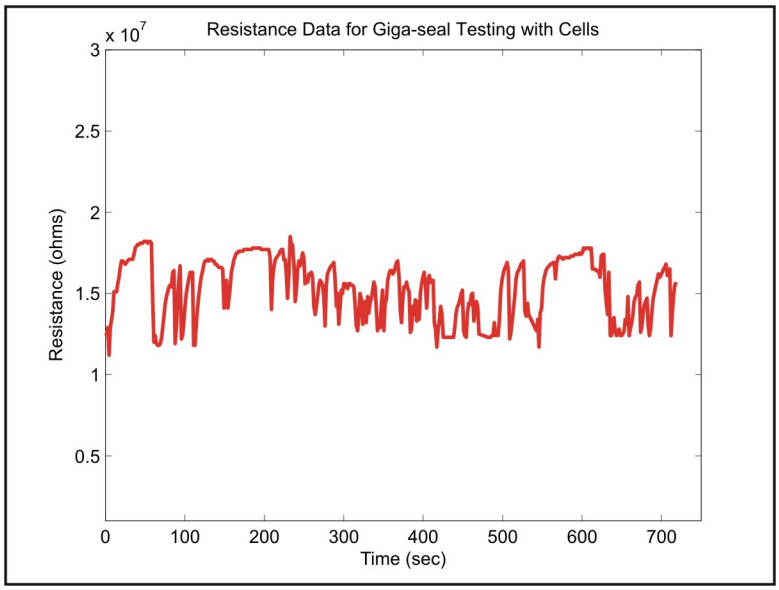

Figure 87: The resistance data collected during giga-seal tests with dissociated 686LN-M4e cells in the analysis cavities showed an average resistance with no cells on the via hole of 15.3 MΩ. There is also no significant increase in the resistance throughout the test during which a cell was pulled against the cavity multiple times using negative pressure inside the microfluidic channel.

via hole minimum diameter = 4 μm,

via hole depth = 50.8 μm,

fluidic channel depth = 50.8 μm,

fluidic channel electrode width = 100 μm.

The giga-seal testing was continued with the dissociated cells. Again, movement of the cells towards and away from the via hole in response to negative and positive pressure was detected and recorded. Figure 87 shows resistance measurements collected during this test. The average resistance when the via hole was open is 15.3 MΩ. Again, the difference between the theoretical and experimental open-via hole resistances is attributed to differences between the designed dimensions and the actual dimensions. As with the polystyrene beads, no significant increase in resistance throughout the test was measured indicating that a giga-seal was never formed. Testing with the cells in 16 analysis cavities over all four devices all produced similar results.

Since the ability of positioning the beads and cells onto the via hole has been verified, the lack of forming a giga-seal can possibly be attributed to surface and edge qualities of

the via holes themselves. If the surface or edge of the via hole is too rough, a good seal between the bead or cell and the hole might not be possible. Additionally, the shape and size of the hole can also possibly contribute to poor sealing. In the conventional patch-clamp technique, the micropipette is fire polished down to only a few microns in diameter.

To investigate the possible issue of the surface and edge quality of the via holes, scanning electron micrographs (SEM's) and optical profilometry readings were taken of the holes. Figure 88 shows SEM's of the via holes in one of the microfluidic systems. The holes are not perfectly circular, but rather are on average 3.6 μm to 4.5 μm from side to side. The edges of the holes do not seem to be rough, but this is difficult to discern in the SEM. The optical profilometry reading of the via hole in Figure 89 shows that there is a raised edge around the hole. However, this raised edge is fairly uniform around the via hole and only reaches heights of approximately 80 nm to 120 nm from the surface. Both the raised edge around the hole and the shape of the hole are due to the laser ablation process, and together could contribute to a giga-seal not forming.

The surface of polymers can be affected by an oxygen plasma treatment, which is sometimes used to help with adhesion of cells to these surfaces. Therefore, to see if the surface and edge of the via hole could be smoothed out, an oxygen plasma treatment was used. Three test samples of Kapton® were made each with an array of via holes laser ablated using the same parameters given in Section 5.1.2. The first sample was treated in an oxygen plasma with the following parameters: 45 sccm of O_2, 50 mT, 50 W, and 60 seconds. The second sample was treated with the same parameters as the first except with a higher power: 150 W. The third sample was left un-treated as a control. Figure 90 shows SEM's from all three samples. It can be seen from these images that both oxygen plasma treatments did not help to smooth out the surface, but rather increased the surface roughness.

Although the topography of the via hole currently limits the ability to perform patch-clamp analysis with this microfluidic system, the results have demonstrated that the system can be used to control the movement and placement of a bead or a single cell in response to negative and positive pressure through a via hole.

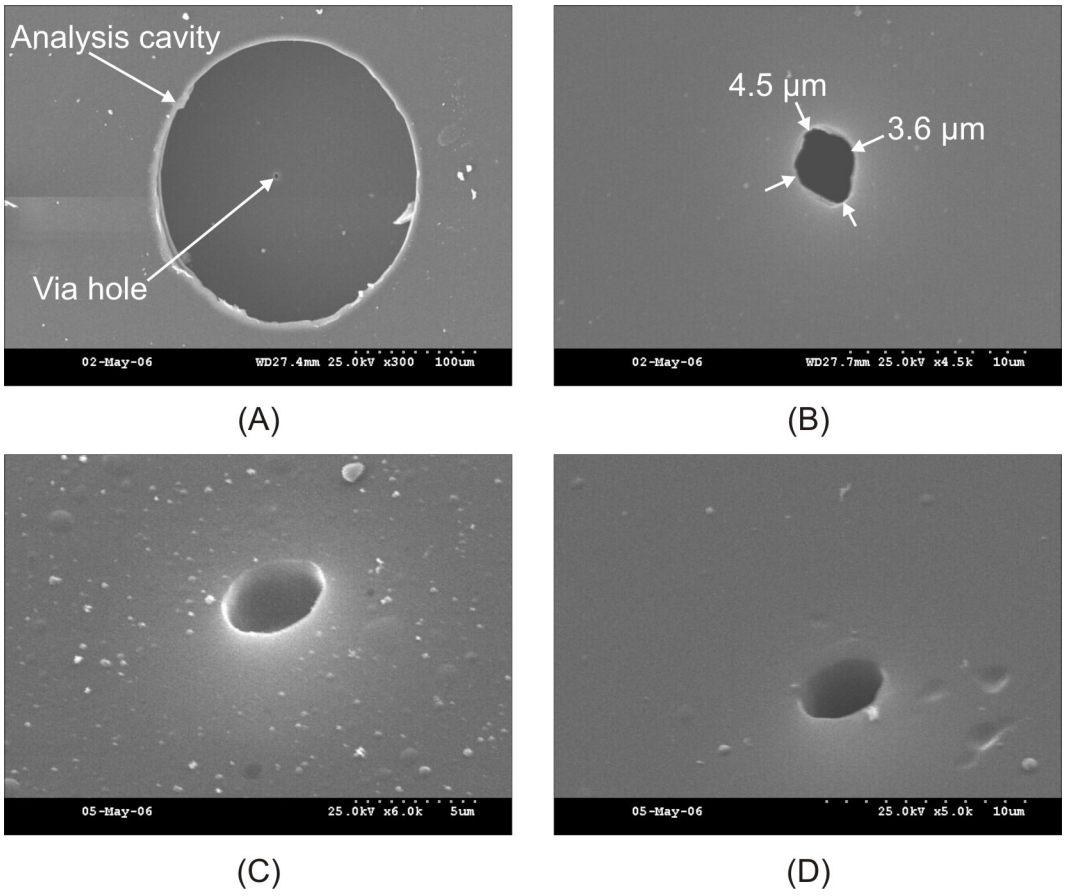

Figure 88: (A) The small via hole can be seen in the center of the 240 μm diameter analysis cavity. (B) The via holes are not perfectly circular, but rather are on average 3.6 μm to 4.5 μm from side to side. (C) and (D) With an angled view of different via holes, the edge quality seems smooth, but this is difficult to determine in the SEM.

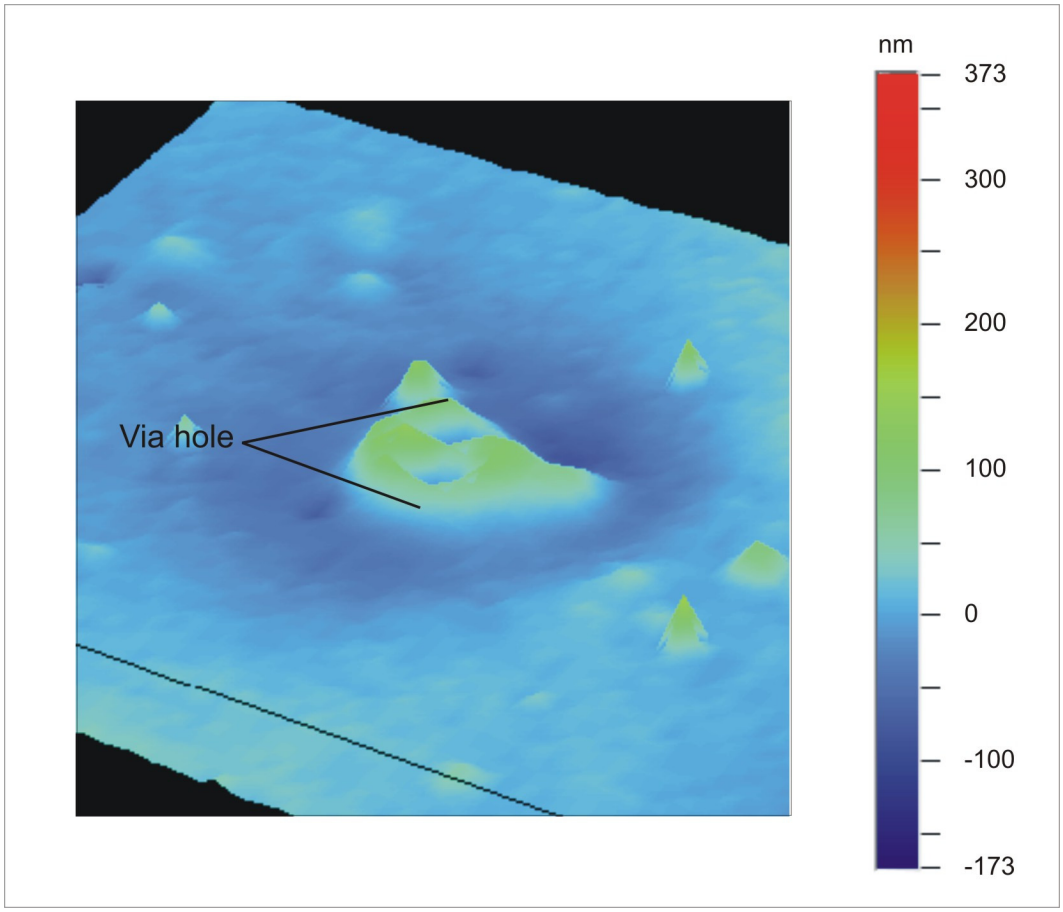

Figure 89: The optical profilometry reading of the via hole shows there is a raised edge around the hole approximately 80 to 120 nm above the rest of the Kapton® surface.

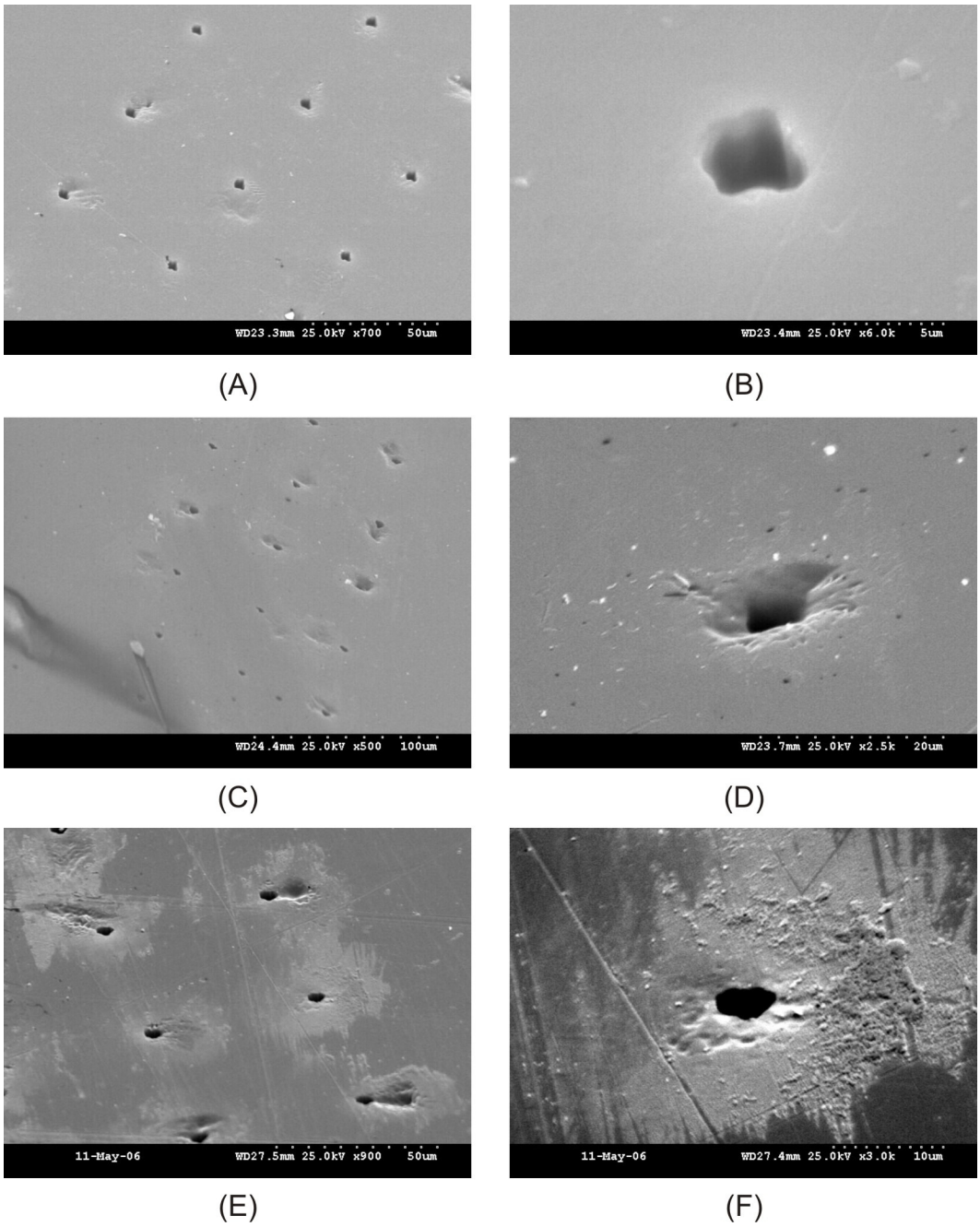

Figure 90: (A) An array of via holes and a single via hole (B) that have not been treated with an oxygen plasma appear to have a fairly smooth surface. (C) and (D) An oxygen plasma treatment of 45 sccm of O_2, 50 mT, 50 W, and 60 seconds has caused some changes to the surface to occur around the via holes. The changes are more of a pitting of the surface rather than smoothing the surface. (E) and (F) An oxygen plasma treatment of O_2, 50 mT, 150 W, and 60 seconds has increased the roughness along the surface.

CHAPTER VI

CONCLUSION AND FUTURE WORK

The objective of this research project was to design, fabricate, and test a flexible, multi-layer microfluidic system using non-standard materials and techniques with the goal of demonstrating a less expensive - to both build and use - whole-cell analysis system. Towards this end, the fabrication techniques of laser ablation, microstenciling, and heat staking were analyzed and combined to realize a multi-layer microfluidic system with integrated electrical functionality made with the polyimide substrate, Kapton®. This fabrication process requires less infrastructure than for typical MEMS processing and allows for a faster design to prototype cycle. As has been described in the preceding chapters, fluidic channels, metal traces, and features from a few millimeters in diameter down to a few microns in diameter are possible with these techniques; therefore, this non-standard process can be adapted for numerous applications to develop a variety of low-cost microfluidic systems. Furthermore, the structural and biological testing performed with the developed microfluidic systems have shown them to be able to withstand reasonable amounts of mechanical loading and to repeatedly measure electrical signals that can possibly be used for identification and characterization of biological samples.

6.1 Summary of Fabrication

Kapton® (types E and EKJ) has been found to be the ideal material to use for the multi-layer, microfluidic system: it is flexible yet durable, biocompatible, stable over a wide temperature range, transparent, and lends itself well to laser ablation and heat staking. The option of using either an excimer laser or a CO_2 laser allows for flexibility in the design of the system. An excimer laser can produce a wide range of feature sizes (as large as 4.7625 mm in diameter to as small as 4 μm in diameter) with smooth edges. However, if feature sizes are not important but speed is, the CO_2 laser can aid in quickly producing

prototypes. Additionally, since the laser ablated designs are only determined by a CAD drawing, a fast design to prototype cycle is promoted with the use of either laser over standard photolithographic processes that would require new masks to be made for any new design. During this research project, this quick design turnaround is evident in the four different design versions discussed in Chapter 2. Microstenciling also reduces fabrication time. Once a microstencil has been made, it can be used repeatedly to pattern metal traces in a single processing step. The microstencils used to pattern the fluidic channel electrodes and cavity electrodes have been used over 10 and 15 times respectively in the development of over 20 microfluidic systems. Also, over their lifetimes, the quality of the features has remained constant. Heat staking is a quick method for bonding the individual layers of Kapton® together, and the 240 μm diameter fiber optic strands provide the ability to align these layers to within 6 μm.

6.2 Summary of Structural and Biological Testing

Positive results were obtained from the theoretical and experimental structural analysis studying the maximum pressure at the inlet to the microfluidic channel due to an applied flow rate. The data showed the channel behaved as expected over the flow rates of interest (up to 5.5 $\frac{mL}{hr}$). Along with visual inspection, this confirmed that the bonding between layers was adequate and no leaks would form during operation. The impedance spectroscopy results from all three devices showed similar trends from device to device in the responses for all the analytes investigated: air, DI water, PBS, 686LN and 686LN-M4e dissociated cells, and treated and non-treated tissue samples. Although the results do not show any statistically significant differences between the different types of dissociated cells or between the different tissue samples, the different signatures in the responses between the biological samples and the non-biological samples shows a positive ability of the system in being able to differentiate and characterize various samples. Furthermore, as compared to a theoretical electrical model, the devices performed as expected within reasonable adjustments being made to the parasitics in the model. The giga-seal testing was not successful in obtaining a giga-seal between a cell and the via hole, which is necessary for patch-clamp analysis.

However, from these tests, the ability to control the movement and position of cells using negative pressure inside the fluidic channel was confirmed. This is beneficial for other types of biological applications that would requiring mechanical control over cells.

6.3 Future Work

The accomplishments of this project provide a solid foundation on which to continue the development of this microfluidic system in the future. Although the results from the biological testing have proven device functionality, they do show that there is a degree of non-uniformity among the multiple microfluidic systems. As part of a future phase of this project, more systems should be fabricated to isolate variability in the development process and to determine the baseline responses for the biological analyses. Additionally, the part of the process limiting the feature sizes is the inability to accurately align the microstencil to the laser ablated Kapton® sheet. To address this issue in the future, a process or a mechanical device that would enable accurate and repeatable alignment needs to be developed. Finally, the cause of the inability to form a giga-seal between the via hole and cell should be investigated if patch-clamping remains a target application of this microfluidic system. This could involve a series of experiments looking first at variables that can be changed during laser ablation and second at surface treatments that can smooth a surface (as opposed to an oxygen plasma that roughened the surface).

As for future biological studies, the impedance spectroscopy analysis can be used to study other types of cancerous cells or to look at cells affected by diseases other than cancer. If the ability to create a giga-seal is achieved, then patch-clamp analysis can be performed. Also, since this fabrication process can be adapted for numerous applications to develop a variety of low-cost microfluidic systems, future projects could include new designs of the system features for entirely different biological applications such as cell sorting.

APPENDIX A

MAINTENANCE AND PREPARATION OF DISSOCIATED CELLS AND TISSUE SAMPLES

The dissociated cells and tissue samples were derived from squamous cell carcinoma of the head and neck (SCCHN) and were obtained from the laboratories of Dr. Georgia Chen and Dr. Doug Shin at Emory University in Atlanta, Georgia. The two types of dissociated cells used are 686LN and 686LN-M4e, which were collected from human tumors at different stages of cancer: 686LN is from an early stage tumor and 686LN-M4e is from a late stage or metastasized tumor. The tissue samples are from sections of tumors grown in mice from human cancer cells and surgically removed as part of a research project at Emory University.

The dissociated cells were brought to the Georgia Institute of Technology at passage two and placed in an incubator (Forma Series II Water Jacketed CO2 Incubator, Thermo Electron Corporation, Waltham, MA) in Dr. Bruno Frazier's laboratory. The cells were maintained in 25 mL canted-neck tissue culture flasks (VWR, West Chester, PA) with 7 mL of cell growth media: 500 mL DMEM/F-12 50/50, 1x with L-glutamine (Cellgro Cell Culture Media, Mediatech, Inc., Herndon, VA), 10% heat inactivated fetal bovine serum (FBS, Hyclone, Logan, UT), and 1x penicillin-streptomycin (Mediatech, Inc.). Cell passage was performed every four days in a Class II A/B3 biological safety cabinet (Thermo Electron Corporation).

To release the cells, the old media was siphoned off and the adhered cells were rinsed with 5 mL of phosphate buffered saline (Cellgro PBS 1x without Ca or Mg, Mediatech, Inc.), which was then also removed. Trypsin (1.5 mL, 0.5%, Cellgro Trypsin EDTA, Mediatech, Inc.) was then added, and the flask was placed back in the incubator for approximately 5 minutes for the cells to release. If at this point a cell passage was performed, half of the cell / trypsin solution was removed either as waste or then placed in another culture flask

to split the cells. For each flask, 7 mL of cell culture media was added.

Some of the original cells were cryopreserved at passage two for use at a later time. The cryopreservation media was comprised of 10% DMSO (dimethyl sulfoxide, Sigma-Aldrich, St. Louis, MO), 10% FBS, and 80% cell culture media. First, the cells were released from the culture flask using the same procedure mentioned above. Then, 5 mL of the culture media was added to the cell / trypsin solution. The cells were then transferred to a centrifuge tube (VWR) and centrifuged (Centrific Centrifuge, Fisher Scientific International, Hampton, NH) at 1500 RPM for 5 minutes. The excess media was removed, and 1 mL of the cryopreservation media was added, and the solution was then placed into a 1 mL cryopreservation vial (VWR). The vial was then placed at $-80°$C for 24 hours and then transferred to the liquid nitrogen. When bringing the cells out of cryopreservation, the vial was taken from the liquid nitrogen and placed in a 37^{circ}C bath. Once the solution was thawed, the cells were divided amongst three culture flasks with 7 mL each of the cell culture media.

When the cells were to be used for testing, first they were released using the same procedure mentioned above. Then, 1.5 mL of the cell culture media was added, and the cells were transferred to a centrifuge tube. They were centrifuged at 1500 RPM for 15 minutes. The excess media was removed, and 5 mL of D-PBS (Cellgro DPBS 1x without Ca or Mg, Mediatech, Inc.) was added. At this point, the cells were ready to be used.

Unlike dissociated cells, tissue samples cannot be maintained for long periods of time without placing them in cryopreservation. Therefore, data is collected on fresh tissue samples within 24 hours of receiving them from Emory University or on frozen samples within a few hours of thawing. Once the section of tissue was removed from the rest of the tumor, the sample was placed in a centrifuge tube with 5 mL of cell culture media with 4x penicillin-streptomycin. This sample was then placed on ice for transfer to the laboratories at the Georgia Institute of Technology. The sample was then used immediately or placed in a refrigerator for no longer than 12 hours before using it for tests. The frozen tissue samples were thawed on ice for one to two minutes, after which they were placed in a centrifuge tube and transferred in the same manner as the fresh tissue samples. The frozen samples

were used immediately upon arrival at the Georgia Institute of Technology.

APPENDIX B

LABVIEW PROGRAM: IMPEDANCE SPECTROSCOPY DATA COLLECTION

To automatically collect the impedance spectroscopy data for an analyte in the analysis cavity, a LabView program (Figures 91, 92 and 93) was developed. The program sends user specified commands to the impedance analyzer (frequency range, number of data points, and averaging of the data points) and then reads in the data once the measurements have been performed. A linear sweep and a logarithmic sweep within the specified frequency range are performed, and both the magnitude and phase responses are recorded.

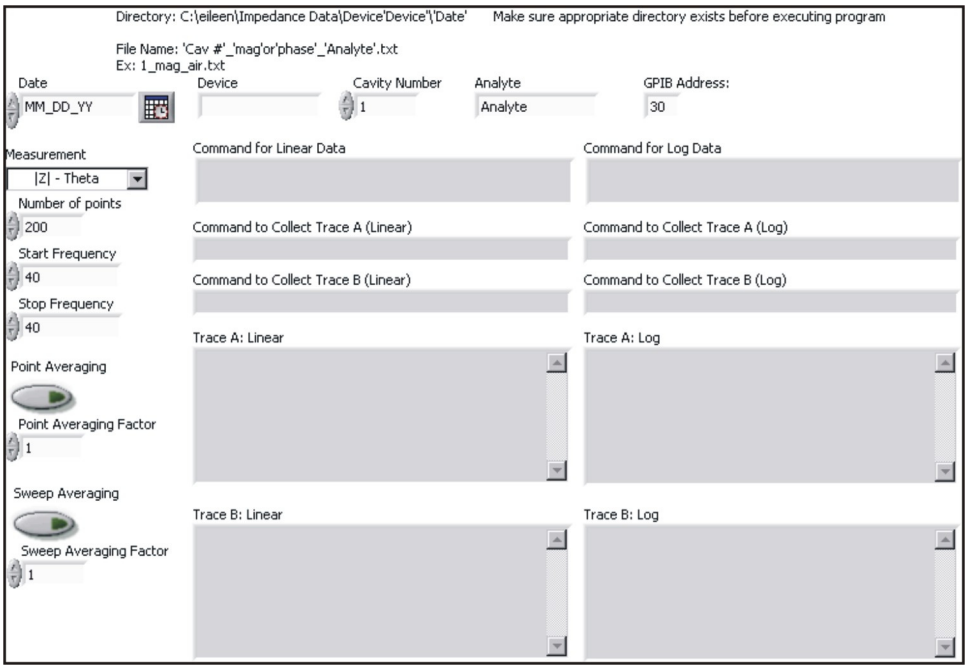

Figure 91: In the front panel of the LabView program, the date, device and analysis cavity under investigation, and type of analyte are all recorded.

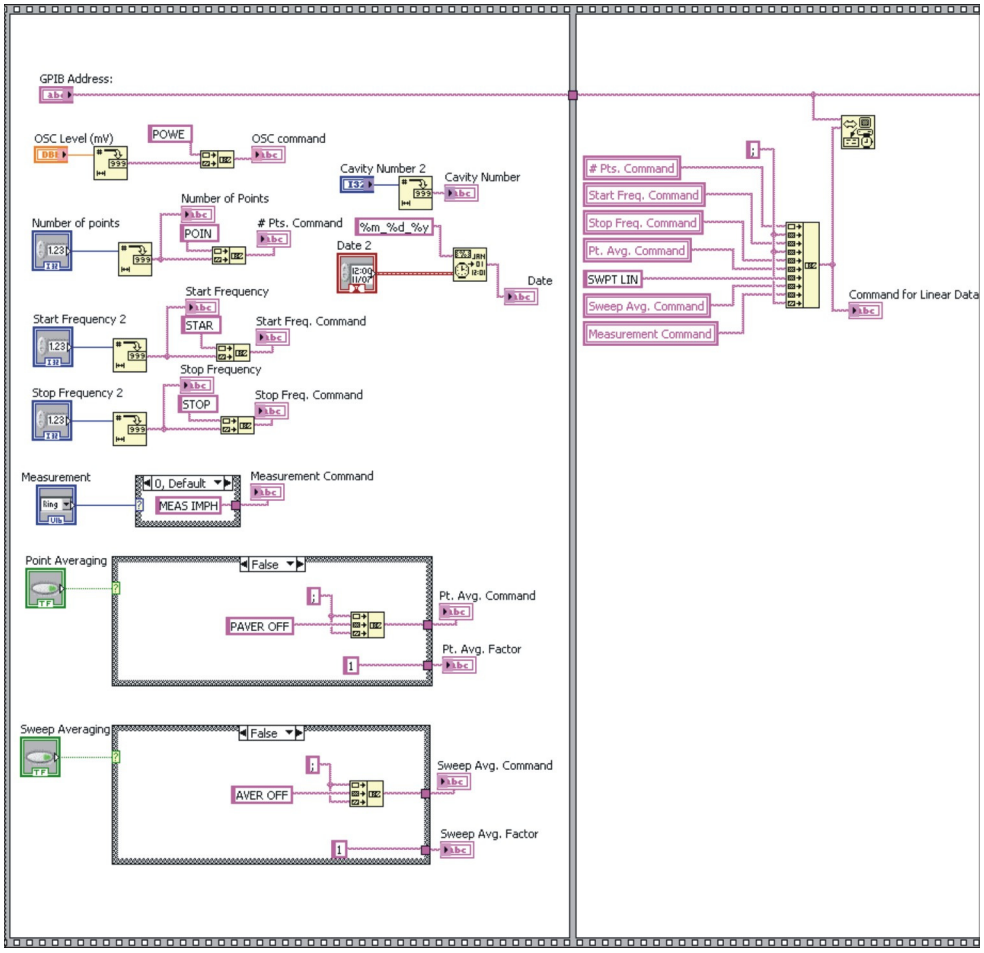

Figure 92: The first portion of the block diagram of the LabView program used for impedance spectroscopy analysis sets up the commands to send to the impedance analyzer.

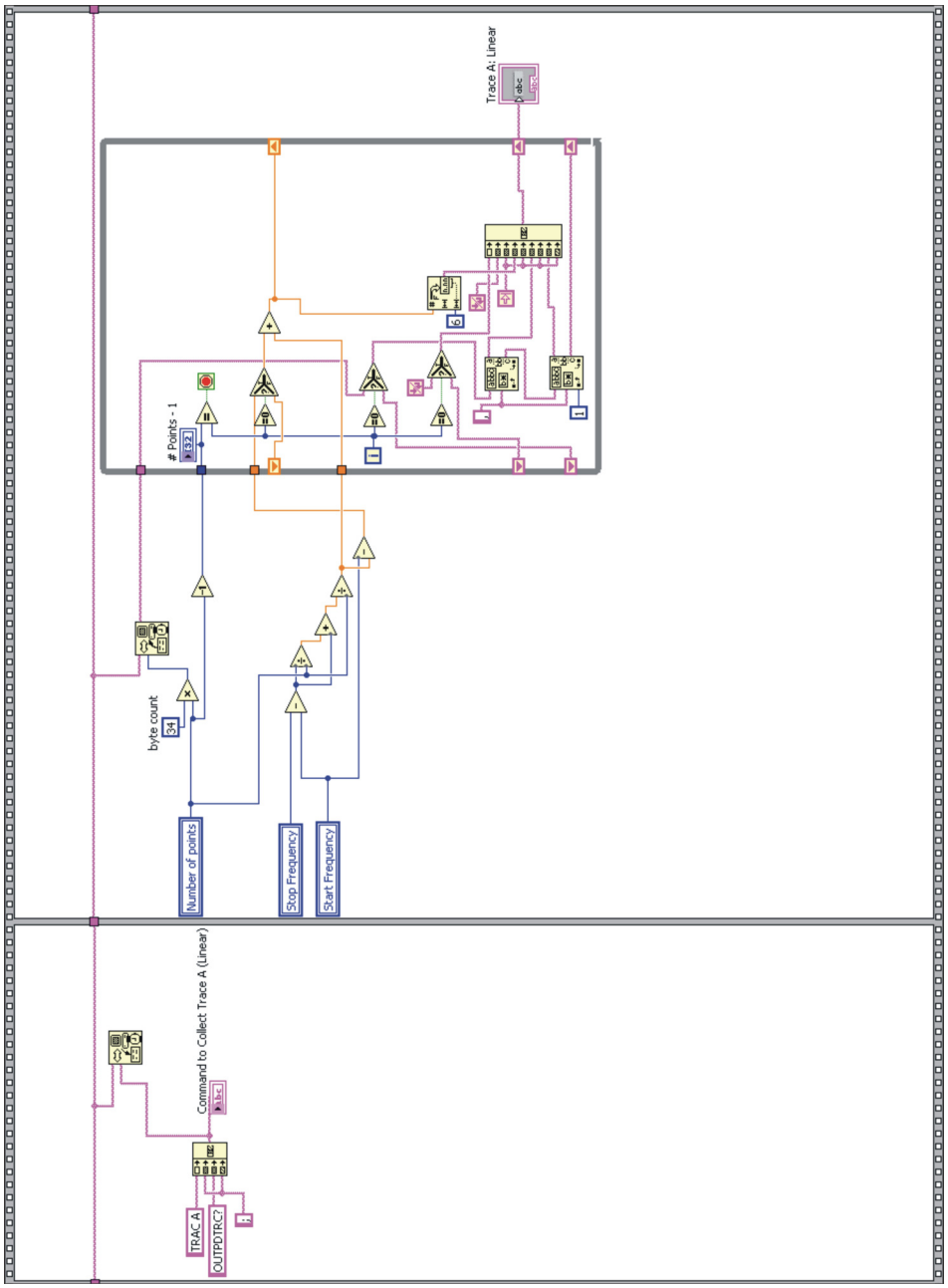

Figure 93: This portion of the block diagram of the LabView program used for impedance spectroscopy analysis reads in the data collected by the impedance analyzer. These blocks are repeated for collecting the magnitude and phase data for both the linear and logarithmic sweeps.

APPENDIX C

LABVIEW PROGRAM: GIGA-SEAL DATA COLLECTION

To obtain the resistance measurement (i.e. giga-seal) between the fluidic channel electrode and the cavity electrode, a LabView program (Figures 94 and 95) was developed to collect the resistance as measured by a digital multimeter in a continuous fashion. This enabled real-time observations to be made on the resistance while applying a negative pressure in the fluidic channel and while watching the resulting actions through a microscope.

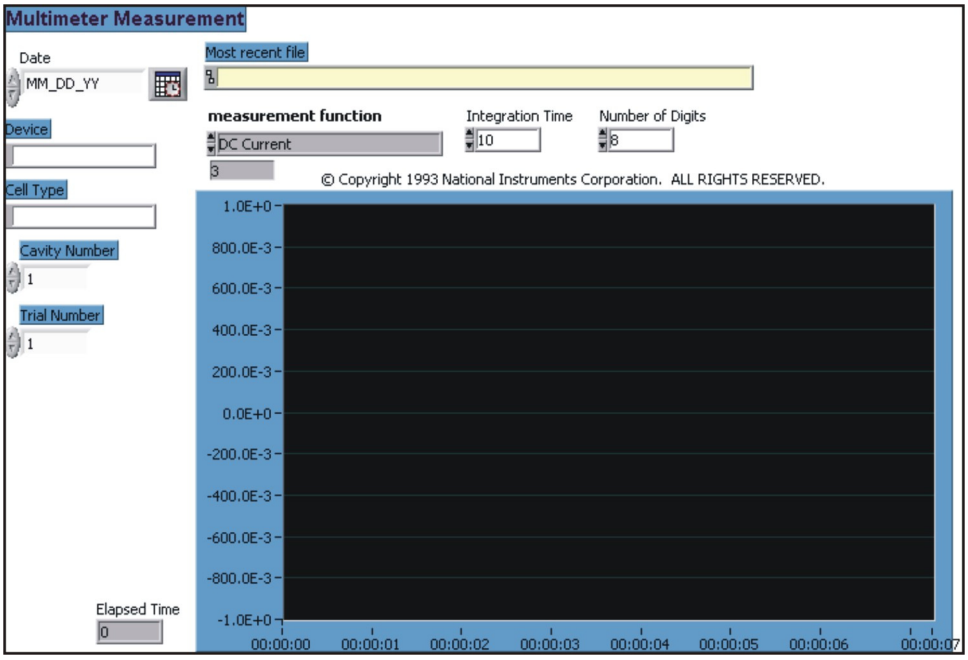

Figure 94: In the front panel of the LabView program, the date, device and analysis cavity under investigation, and type of cell used for testing are all recorded. When running the program, a continuous view of the measured impedance is shown.

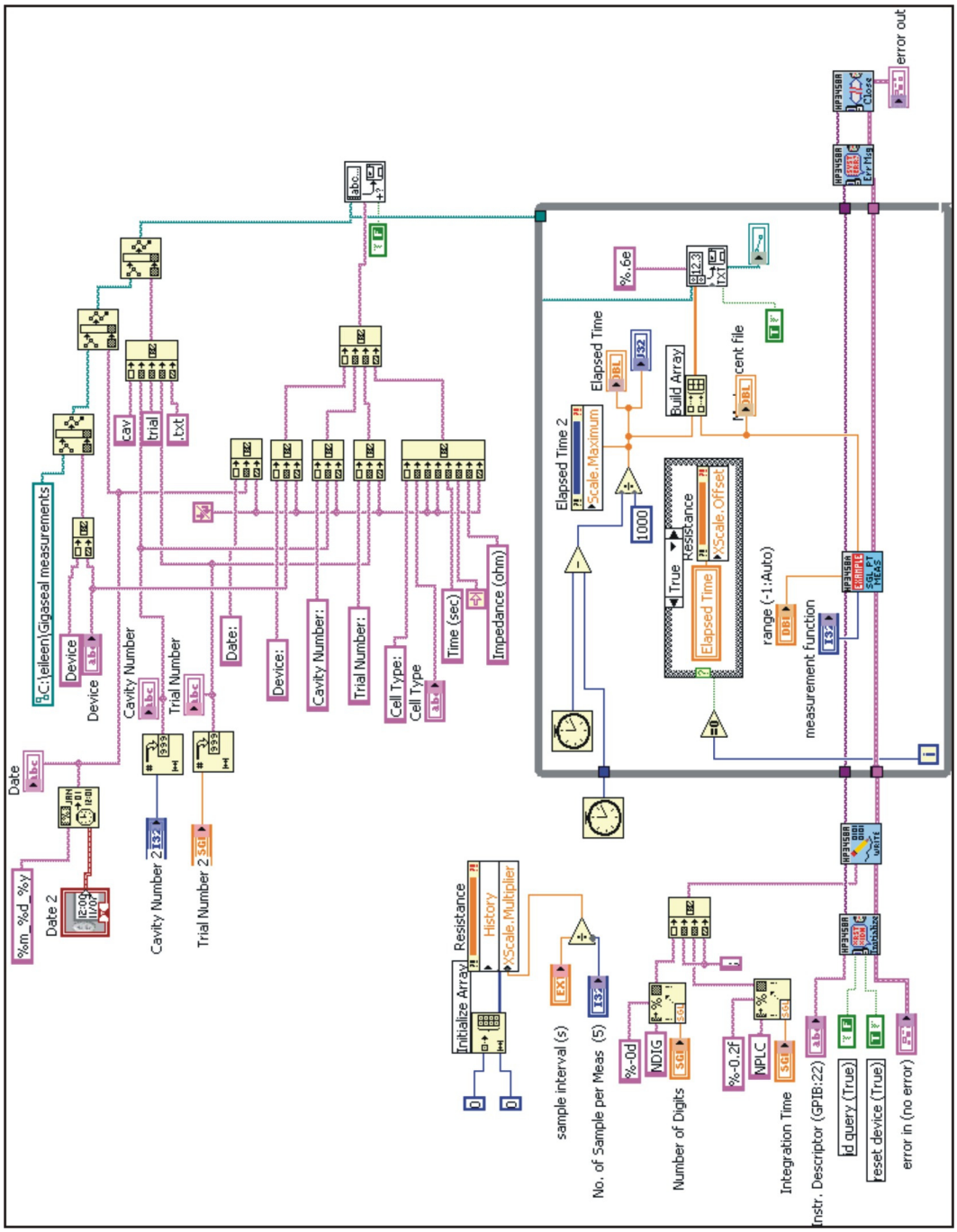

Figure 95: Block diagram of LabView program used for giga-seal testing.

REFERENCES

[1] Adams, C., Mathieson, K., Gunning, D., Cunningham, W., Rahman, M., Morrison, J. D., and Prydderch, M. L., "Development of flexible arrays for in vivo neuronal recording and stimulation," *Nuclear Instruments & Methods in Physics Research Section a-Accelerators Spectrometers Detectors and Associated Equipment*, vol. 546, no. 1-2, pp. 154–159, 2005.

[2] Aidley, D. J. and Stanfield, P. R., *Ion Channels: Molecules in Action*. Cambridge: Cambridge University Press, 1996.

[3] Andersson, H. and van den Berg, A., "Microfluidic devices for cellomics: a review," *Sensors and Actuators B-Chemical*, vol. 92, no. 3, pp. 315–325, 2003.

[4] Ashcroft, F. M., *Ion Channels and Disease: Channelopathies*. San Diego: Academic Press, 2000.

[5] Asmild, M., Oswald, N., Krzywkowski, K. M., Friis, S., Jacobsen, R. B., Reuter, D., Taboryski, R., Kutchinsky, J., Vestergaard, R. K., Schroder, R. L., Sorensen, C. B., Bech, M., Korsgaard, M. P. G., and Willumsen, N. J., "Upscaling and automation of electrophysiology: Toward high throughput screening in ion channel drug discovery," *Receptors & Channels*, vol. 9, no. 1, pp. 49–58, 2003.

[6] Ayliffe, H. E., Frazier, A. B., and Rabbitt, R. D., "Electric impedance spectroscopy using microchannels with integrated metal electrodes," *Journal of Microelectromechanical Systems*, vol. 8, no. 1, pp. 50–57, 1999.

[7] Baker, L. E., "Applications of the impedance technique to the respiratory system," *Ieee Engineering in Medicine and Biology Magazine*, vol. 8, no. 1, pp. 50–52, 1989.

[8] Bard, A. J. and Faulkner, L. R., *Electrochemical Methods: Fundamentals and Applications*. New York: John Wiley & Sons, Inc., 2nd ed., 2001.

[9] Bonincontro, A. and Mariutti, G., "Influence of hyperthermia, ph and culturing conditions on the electrical parameters of chinese-hamster v79 cells," *Physics in Medicine and Biology*, vol. 33, no. 5, pp. 557–568, 1988.

[10] Brannon, J., "Excimer laser ablation and etching - making a mark in many applications," *Ieee Circuits & Devices*, vol. 13, no. 2, pp. 11–18, 1997.

[11] Brown, B. H., Barber, D. C., Morice, A. H., and Leathard, A. D., "Cardiac and respiratory-related electrical-impedance changes in the human thorax," *Ieee Transactions on Biomedical Engineering*, vol. 41, no. 8, pp. 729–734, 1994.

[12] Buerk, D. G., *Biosensors: Theory and Applications*. Lancaster: Technomic Publishing Company, Inc., 1993.

[13] Cambell, S. A., *The Science and Engineering of Microelectronic Fabrication*. New York: Oxford University Press, 2nd ed., 2001.

[14] Campbell, A. M. and Land, D. V., "Dielectric-properties of female human breast-tissue measured invitro at 3.2 ghz," *Physics in Medicine and Biology*, vol. 37, no. 1, pp. 193–210, 1992.

[15] Carlson, R. H., Gabel, C. V., Chan, S. S., Austin, R. H., Brody, J. P., and Winkelman, J. W., "Self-sorting of white blood cells in a lattice," *Physical Review Letters*, vol. 79, no. 11, pp. 2149–2152, 1997.

[16] Chandrasekaran, S., Brazzle, J. D., and Frazier, A. B., "Surface micromachined metallic microneedles," *Journal of Microelectromechanical Systems*, vol. 12, no. 3, pp. 281–288, 2003.

[17] Chang, B. Y. and Park, S. M., "Integrated description of electrode/electrolyte interfaces based on equivalent circuits and its verification using impedance measurements," *Anal. Chem.*, 2005.

[18] Chang, S. P., Lee, J. B., and Allen, M. G., "Robust capacitive pressure sensor array," *Sensors and Actuators a-Physical*, vol. 101, no. 1-2, pp. 231–238, 2002.

[19] Chaudhary, S. S., Mishra, R. K., Swarup, A., and Thomas, J. M., "Dielectric-properties of normal and malignant human-breast tissues at radiowave and microwave-frequencies," *Indian Journal of Biochemistry & Biophysics*, vol. 21, no. 1, pp. 76–79, 1984.

[20] Chen, C., "beta-amyloid increases dendritic ca2+ influx by inhibiting the a-type k+ current in hippocampal ca1 pyramidal neurons," *Biochemical and Biophysical Research Communications*, vol. 338, no. 4, pp. 1913–1919, 2005.

[21] Chen, J. K., Wise, K. D., Hetke, J. F., and Bledsoe, S. C., "A multichannel neural probe for selective chemical delivery at the cellular level," *Ieee Transactions on Biomedical Engineering*, vol. 44, no. 8, pp. 760–769, 1997.

[22] Cheung, K., Kubow, T., and Lee, L. P., "Individually addressable planar patch clamp array," in *2nd Annual International IEEE-EMB Special Topic Conference on Microtechnologies in Medicine & Biology*, (Masison, WI), pp. 71–75, 2002.

[23] Chumlea, W. C. and Guo, S. S., "Bioelectrical-impedance and body-composition - present status and future-directions," *Nutrition Reviews*, vol. 52, no. 4, pp. 123–131, 1994.

[24] Conn, H. J., *Biological Stains*. Baltimore: The Williams and Wilkins Company, 9 ed., 1977.

[25] Cooper, E. C. and Jan, L. Y., "Ion channel genes and human neurological disease: Recent progress, prospects, and challenges," *Proceedings of the National Academy of Sciences of the United States of America*, vol. 96, no. 9, pp. 4759–4766, 1999.

[26] Cosofret, V. V., Erdosy, M., Johnson, T. A., Bellinger, D. A., Buck, R. P., Ash, R. B., and Neuman, M. R., "Electroanalytical and surface characterization of

encapsulated implantable membrane planar microsensors," *Analytica Chimica Acta*, vol. 314, no. 1-2, pp. 1–11, 1995.

[27] Coulter, W., "Means for counting particles suspended in a fluid," October 20, 1953 1953.

[28] Crafer, R. C., Oakley, P. J., Adams, M. J., Williams, C., and Gower, M. C. in *Laser Processing in Manufacturing* (Crafer, R. C. and Oakley, P. J., eds.), London: Chapman & Hall, 1993.

[29] Dario, P., Carrozza, M. C., Benvenuto, A., and Menciassi, A., "Micro-systems in biomedical applications," *Journal of Micromechanics and Microengineering*, vol. 10, no. 2, pp. 235–244, 2000.

[30] Davey, C. L., Davey, H. M., and Kell, D. B., "On the dielectric-properties of cell-suspensions at high-volume fractions," *Bioelectrochemistry and Bioenergetics*, vol. 28, no. 1-2, pp. 319–340, 1992.

[31] Davis, S. P., Martanto, W., Allen, M. G., and Prausnitz, M. R., "Hollow metal microneedles for insulin delivery to diabetic rats," *Ieee Transactions on Biomedical Engineering*, vol. 52, no. 5, pp. 909–915, 2005.

[32] Deng, J. D., Schoenbach, K. H., Buescher, E. S., Hair, P. S., Fox, P. M., and Beebe, S. J., "The effects of intense submicrosecond electrical pulses on cells," *Biophysical Journal*, vol. 84, no. 4, pp. 2709–2714, 2003.

[33] DePaola, N., Phelps, J. E., Florez, L., Keese, C. R., Minnear, F. L., Giaever, I., and Vincent, P., "Electrical impedance of cultured endothelium under fluid flow," *Annals of Biomedical Engineering*, vol. 29, no. 8, pp. 648–656, 2001.

[34] Duffy, D. C., McDonald, J. C., Schueller, O. J. A., and Whitesides, G. M., "Rapid prototyping of microfluidic systems in poly(dimethylsiloxane)," *Analytical Chemistry*, vol. 70, no. 23, pp. 4974–4984, 1998.

[35] DuPont, "Kapton ekj: Self-adhering polyimide composite film," Tech. Rep. H-38494, 1993.

[36] DuPont, "Dupont kapton e: High modulus polyimide film," Tech. Rep. H-97928, 2003.

[37] Durack, G. and Robinson, J. P., *Emerging Tools for Single-Cell Analysis: Advances in Optical Measurement Technologies*. New York: John Wiley and Sons, Inc., 2000.

[38] Edwards, T. L., Gale, B. K., and Frazier, A. B., "A microfabricated thermal field-flow fractionation system," *Analytical Chemistry*, vol. 74, no. 6, pp. 1211–1216, 2002.

[39] Endert, H., Patzel, R., and Basting, D., "Excimer laser: A new tool for precision micromachining," *Optical and Quantum Electronics*, vol. 27, no. 12, pp. 1319–1335, 1995.

[40] Fertig, N., Blick, R. H., and Behrends, J. C., "Whole cell patch clamp recording performed on a planar glass chip," *Biophysical Journal*, vol. 82, no. 6, pp. 3056–3062, 2002.

[41] Fertig, N., Meyer, C., Blick, R. H., Trautmann, C., and Behrends, J. C., "Microstructured glass chip for ion-channel electrophysiology," *Physical Review E*, vol. 6404, no. 4, 2001.

[42] Foster, K. R. and Schwan, H. P., "Dielectric-properties of tissues and biological-materials - a critical-review," *Critical Reviews in Biomedical Engineering*, vol. 17, no. 1, pp. 25–104, 1989.

[43] Fox, R. W. and McDonald, A. T., *Introduction to Fluid Mechanics*. New York: John Wiley & Sons, Inc., 5th ed., 1998.

[44] Gale, J. E. and Ashmore, J. F., "The outer hair cell motor in membrane patches," *Pflugers Archiv-European Journal of Physiology*, vol. 434, no. 3, pp. 267–271, 1997.

[45] Gawad, S., Henschkel, M., Leung-Ki, Y., Iuzzolino, R., Schild, L., Lerch, P., and Renaud, P., "Fabrication of a microfluidic cell analyzer in a microchannel using impedance spectroscopy," in *1st Annual International Conference on Microtechnologies in Medicine and Biology*, pp. 297–301, 2000.

[46] Gawad, S., Schild, L., and Renaud, P., "Micromachined impedance spectroscopy flow cytometer for cell analysis and particle sizing," *Lab on a Chip*, vol. 1, no. 1, pp. 76–82, 2001.

[47] Geddes, L. A. and Baker, L. E., *Principles of Applied Biomedical Instrumentation*. New York: John Wiley & Sons Inc., 3rd ed., 1989.

[48] Gheorghiu, E. and Asami, K., "Monitoring cell cycle by impedance spectroscopy: experimental and theoretical aspects," *Bioelectrochemistry and Bioenergetics*, vol. 45, no. 2, pp. 139–143, 1998.

[49] Giaever, I. and Keese, C. R., "A morphological biosensor for mammalian-cells," *Nature*, vol. 366, no. 6455, pp. 591–592, 1993.

[50] Gibb, A. J., "Patch-clamp recording," in *Ion Channels: A Practical Approach* (Ashley, R. H., ed.), pp. 1–42, Oxford: Oxford University Press, 1995.

[51] Gielen, F. L. H., Wallingadejonge, W., and Boon, K. L., "Electrical-conductivity of skeletal-muscle tissue - experimental results from different muscles invivo," *Medical & Biological Engineering & Computing*, vol. 22, no. 6, pp. 569–577, 1984.

[52] Giordano, B. C., Ferrance, J., Swedberg, S., Huhmer, A. F. R., and Landers, J. P., "Polymerase chain reaction in polymeric microchips: Dna amplification in less than 240 seconds," *Analytical Biochemistry*, vol. 291, no. 1, pp. 124–132, 2001.

[53] Giovangrandi, L., Gilchrist, K. H., Whittington, R. H., and Kovacs, G. T. A., "Low-cost microelectrode array with integrated heater for extracellular recording of cardiomyocyte cultures using commercial flexible printed circuit technology," *Sensors and Actuators B-Chemical*, vol. 113, no. 1, pp. 545–554, 2006.

[54] Gomez, R., Bashir, R., and Bhunia, A. K., "Microscale electronic detection of bacterial metabolism," *Sensors and Actuators B-Chemical*, vol. 86, no. 2-3, pp. 198–208, 2002.

[55] Gomez, R., Bashir, R., Sarikaya, A., Ladisch, M. R., Sturgis, J., Robinson, J. P., Geng, T., Bhunia, A. K., Apple, H. L., and Wereley, S., "Microfluidic biochip for impedance spectroscopy of biological species," *Biomedical Microdevices*, vol. 3, no. 3, pp. 201–209, 2001.

[56] Graff, M., Mohanty, S. K., Moss, E., and Frazier, A. B., "Microstenciling: A generic technology for microscale patterning of vapor deposited materials," *Journal of Microelectromechanical Systems*, vol. 13, no. 6, pp. 956–962, 2004.

[57] Gronlund, J. U., Jalonen, J., Korhonen, I., Rolfe, P., and Valimaki, I. A. T., "Multivariate autoregressive modeling combined with transcephalic electrical-impedance - method to relate neonatal systemic circulation and respiration to cerebral-circulation," *Medical & Biological Engineering & Computing*, vol. 33, no. 3, pp. 458–463, 1995.

[58] Han, A., Moss, E., and Frazier, A. B., "Whole cell electrical impedance spectroscopy for studying ion channel activity," in *The 13th International Conference on Solid-State Sensors, Actuators and Microsystems (Transducers 2005)*, (Seoul, Korea), pp. 1704–1707, 2005.

[59] Han, A., Moss, E., Rabbitt, R. D., Engisch, K. L., and Frazier, A. B., "A single cell multi-analysis system for electrophysiological studies," in *The 12th International Conference on Solid-State Sensors, Actuators and Microsystems (Transducers 2003)*, (Boston, MA), pp. 674–677, 2003.

[60] Han, A. R., Wang, O., Graff, M., Mohanty, S. K., Edwards, T. L., Han, K. H., and Frazier, A. B., "Multi-layer plastic/glass microfluidic systems containing electrical and mechanical functionality," *Lab on a Chip*, vol. 3, no. 3, pp. 150–157, 2003.

[61] Han, A., Cruz-Rivera, L. J., and Frazier, A. B., "Study of breast cancer using whole cell impedance spectroscopy," in *The 9th International Conference on Miniaturized Systems for Chemistry and Life Sciences (uTAS 2005)*, (Boston, MA), pp. 364–366, 2005.

[62] Han, K. H. and Frazier, A. B., "Diamagnetic capture mode magnetophoretic microseparator for blood cells," *Journal of Microelectromechanical Systems*, vol. 14, no. 6, pp. 1422–1431, 2005.

[63] Hart, F. X. and Dunfee, W. R., "In-vivo measurement of the low-frequency dielectric spectra of frog skeletal-muscle," *Physics in Medicine and Biology*, vol. 38, no. 8, pp. 1099–1112, 1993.

[64] Haugland, R. P. and Minta, A., "Design and application of indicator dyes," in *Noninvasive Techniques in Cell Biology* (Foskett, J. K. and Grinstein, S., eds.), New York: John Wiley and Sons, Inc., 1990.

[65] Hayt, W. H. and Kemmerly, J. E., *Engineering Circuit Analysis*. New York: McGraw-Hill, Inc., 1993.

[66] Hillebrandt, H., Wiegand, G., Tanaka, M., and Sackmann, E., "High electric resistance polymer/lipid composite films on indium-tin-oxide electrodes," *Langmuir*, vol. 15, no. 24, pp. 8451–8459, 1999.

[67] Hoffman, R. A. and Swartzendruber, D. E., "Electrical-impedance analysis of single murine teratocarcinoma cells," *Experimental Cell Research*, vol. 122, no. 2, pp. 426–429, 1979.

[68] http://www.phschool.com/atschool/, "Ph@school: Science explorer: Life science: Student chapter1," 2005. Accessed May 2006.

[69] Huang, Y., Joo, S., Duhon, M., Heller, M., Wallace, B., and Xu, X., "Dielectrophoretic cell separation and gene expression profiling on microelectronic chip arrays," *Analytical Chemistry*, vol. 74, no. 14, pp. 3362–3371, 2002.

[70] Jensen, M. F., Noerholm, M., Christensen, L. H., and Geschke, O., "Microstructure fabrication with a co2 laser system: characterization and fabrication of cavities produced by raster scanning of the laser beam," *Lab on a Chip*, vol. 3, no. 4, pp. 302–307, 2003.

[71] Jo, B. H., Van Lerberghe, L. M., Motsegood, K. M., and Beebe, D. J., "Three-dimensional micro-channel fabrication in polydimethylsiloxane (pdms) elastomer," *Journal of Microelectromechanical Systems*, vol. 9, no. 1, pp. 76–81, 2000.

[72] Jossinet, J., Lobel, A., Michoudet, C., and Schmitt, M., "Quantitative technique for bio-electrical spectroscopy," *Journal of Biomedical Engineering*, vol. 7, no. 4, pp. 289–294, 1985.

[73] Jurkat-Rott, K. and Lehmann-Hom, F., "The patch clamp technique in ion channel research," *Current Pharmaceutical Biotechnology*, vol. 5, no. 4, pp. 387–395, 2004.

[74] Kancharla, V. V. and Chen, S. C., "Fabrication of biodegradable polymeric micro-devices using laser micromachining," *Biomedical Microdevices*, vol. 4, no. 2, pp. 105–109, 2002.

[75] Klemic, K. G., Klemic, J. F., Reed, M. A., and Sigworth, F. J., "Micromolded pdms planar electrode allows patch clamp electrical recordings from cells," *Biosensors & Bioelectronics*, vol. 17, no. 6-7, pp. 597–604, 2002.

[76] Kos, L. and Garcia, R. J., "Biological assays," in *Molecular Biology Techniques and Applications* (Moore, J. and Zouridakis, G., eds.), CRC Press, LLC, 2004.

[77] Kovacs, G. T. A., *Micromachined Transducers Sourcebook*. McGraw-Hill, 1998.

[78] K'Owino, I. O. and Sadik, O. A., "Impedance spectroscopy: A powerful tool for rapid biomolecular screening and cell culture monitoring," *Electroanalysis*, vol. 17, no. 23, pp. 2101–2113, 2005.

[79] Kutter, J. P., Mogensen, K. B., Klank, H., Geschke, O., and Jorgensen, A. M. in *Microsystem Engineering of Lab-on-a-Chip Devices* (Geschke, O., Klank, H., and Tellemann, P., eds.), Weinheim: WILEY-VCH Verlag GmbH & Co. KGaA, 2004.

[80] Laermer, F., Schilp, A., Funk, K., and Offenberg, M., "Bosch deep silicon etching: improving uniformity and etch rate for advanced mems applications," in *Twelfth IEEE international conference on micro electro mechanical systems, 1999*, (Orlando, FL), pp. 211–216, 1999.

[81] Lehnert, T., Gijs, M. A. M., Netzer, R., and Bischoff, U., "Realization of hollow sio2 micronozzles for electrical measurements on living cells," *Applied Physics Letters*, vol. 81, no. 26, pp. 5063–5065, 2002.

[82] Lehnert, T., Netzer, R., Bischoff, U., and Gijs, M. A. M., "Sio2 nozzle array-based patch-clamp microsystem," in *Micro Total Analysis Systems, 2002*, (Nara, Japan), 2002.

[83] Li, C. Y., Sauser, F. E., Azizkhan, R. G., Ahn, C. H., and Papautsky, I., "Polymer flip-chip bonding of pressure sensors on a flexible kapton film for neonatal catheters," *Journal of Micromechanics and Microengineering*, vol. 15, no. 9, pp. 1729–1735, 2005.

[84] Li, P. C. H. and Harrison, D. J., "Transport, manipulation, and reaction of biological cells on-chip using electrokinetic effects," *Analytical Chemistry*, vol. 69, no. 8, pp. 1564–1568, 1997.

[85] Liang, G. H., Moore, E. J., Ulfendahl, M., Rydqvist, B., and Jarlebark, L., "An m-like potassium current in the guinea pig cochlea," *Orl-Journal for Oto-Rhino-Laryngology and Its Related Specialties*, vol. 67, no. 2, pp. 75–82, 2005.

[86] Lin, Y. C., Jen, C. M., Huang, M. Y., Wu, C. Y., and Lin, X. Z., "Electroporation microchips for continuous gene transfection," *Sensors and Actuators B-Chemical*, vol. 79, no. 2-3, pp. 137–143, 2001.

[87] Lingwood, B. E., Coghlan, J. P., Ward, L. C., Charles, B. G., and Colditz, P. B., "Measurement of extracellular fluid volume in the neonate using multiple frequency bio-impedance analysis," *Physiological Measurement*, vol. 21, no. 2, pp. 251–262, 2000.

[88] Lucas, P. T., Meadows, L. S., Nicholls, J., and Ragsdale, D. S., "An epilepsy mutation in the beta 1 subunit of the voltage-gated sodium channel results in reduced channel sensitivity to phenytoin," *Epilepsy Research*, vol. 64, no. 3, pp. 77–84, 2005.

[89] Lukaski, H. C., Bolonchuk, W. W., Hall, C. B., and Siders, W. A., "Validation of tetrapolar bioelectrical impedance method to assess human-body composition," *Journal of Applied Physiology*, vol. 60, no. 4, pp. 1327–1332, 1986.

[90] Malkin, R. A. and Pendley, B. D., "Construction of a very high-density extracellular electrode array," *American Journal of Physiology-Heart and Circulatory Physiology*, vol. 279, no. 1, pp. H437–H442, 2000.

[91] Manz, A., Graber, N., and Widmer, H. M., "Miniaturized total chemical-analysis systems - a novel concept for chemical sensing," *Sensors and Actuators B-Chemical*, vol. 1, no. 1-6, pp. 244–248, 1990.

[92] Masters, B. R., *Confocal Microscopy and Multiphoton Excitation Microscopy: The Genesis of Live Cell Imaging*. Bellingham: The International Society for Optical Engineering, 2006.

[93] Matthews, B. and Judy, J. W., "Characterization of a micromachined planar patch clamp for cellular electrophysiology," in *First International IEEE EMBS Conference on Neural Engineering, 2003*, pp. 648–651, 2003.

[94] McCarty, N. A. and Zhang, Z. R., "Identification of a region of strong discrimination in the pore of cftr," *American Journal of Physiology-Lung Cellular and Molecular Physiology*, vol. 281, no. 4, pp. L852–L867, 2001.

[95] McClain, M. A., Culbertson, C. T., Jacobson, S. C., and Ramsey, J. M., "Flow cytometry of escherichia coli on nucrifluidic devices," *Analytical Chemistry*, vol. 73, no. 21, pp. 5334–5338, 2001.

[96] Medoro, G., Manaresi, N., Leonardi, A., Altomare, L., Tartagni, M., and Guerrieri, R., "A lab-on-a-chip for cell detection and manipulation," *Sensors Journal, IEEE*, vol. 3, no. 3, pp. 317–325, 2003.

[97] Metz, S., Oppliger, F., Holzer, R., Buisson, B., Bertrand, D., and Renaud, P., "Fabrication and test of implantable thin-film electrodes for stimulation and recording of biological signals," in *1st annual international conference on microtechnologies in medicine and biology*, (Lyon), pp. 619–623, 2000.

[98] Mirtaheri, P., Grimnes, S., and Martinsen, O. G., "Electrode polarization impedance in weak nacl aqueous solutions," *Ieee Transactions on Biomedical Engineering*, vol. 52, no. 12, pp. 2093–2099, 2005.

[99] Mohanty, S. K., Graff, M., Ravula, K., Han, A., and Frazier, A. B., "A micro stenciling process for wafer scale metallization of plastic substrates," in *Micro Total Analysis Systems 2001*, (Monterey, CA), pp. 387–388, 2001.

[100] Morucci, J. P. and Rigaud, B., "Bioelectrical impedance techniques in medicine .3. impedance imaging - third section: Medical applications," *Critical Reviews in Biomedical Engineering*, vol. 24, no. 4-6, pp. 655–677, 1996.

[101] Munson, B. R., Young, D. F., and Okiishi, T. H., *Fundamentals of Fluid Mechanics*. New York: John Wiley & Sons, Inc., 3rd ed., 1998.

[102] Najafi, K., "Integrated sensors in biological environments," *Sensors and Actuators B-Chemical*, vol. 1, no. 1-6, pp. 453–459, 1990.

[103] Nakamura, T., Yamamoto, Y., Yamamoto, T., and Tsuji, H., "Fundamental characteristics of human limb electrical-impedance for biodynamic analysis," *Medical & Biological Engineering & Computing*, vol. 30, no. 5, pp. 465–472, 1992.

[104] Nie, A. F. and Meng, Z. Q., "Sulfur dioxide derivative modulation of potassium channels in rat ventricular myocytes," *Archives of Biochemistry and Biophysics*, vol. 442, no. 2, pp. 187–195, 2005.

[105] Nomura, I., Kato, N., Kita, T., and Takechi, H., "Mechanism of impairment of long-term potentiation by amyloid beta is independent of nmda receptors or voltage-dependent calcium channels in hippocampal ca1 pyramidal neurons," *Neuroscience Letters*, vol. 391, no. 1-2, pp. 1–6, 2005.

[106] Nopp, P., Rapp, E., Pfutzner, H., Nakesch, H., and Ruhsam, C., "Dielectric-properties of lung-tissue as a function of air content," *Physics in Medicine and Biology*, vol. 38, no. 6, pp. 699–716, 1993.

[107] Ozaki, N., Ogawa, R., Sugihara, H., Emoto, F., Tanabe, M., Konishi, S., and Oka, H., "Electrophysiological high throughput drug screening system," in *Micro Total Analysis Systems, 2002*, (Nara, Japan), 2002.

[108] Pandey, S. and White, M. H., "An integrated planar patch-clamp system," in *2001 International Semiconductor Device Research Symposium*, (Washington, DC), pp. 170–173, 2001.

[109] Patterson, R., "Body-fluid determinations using multiple impedance measurements," *Ieee Engineering in Medicine and Biology Magazine*, vol. 8, no. 1, pp. 16–18, 1989.

[110] Peloso, R., Tuma, D. T., and Jain, R. K., "Dielectric-properties of solid tumors during normothermia and hyperthermia," *Ieee Transactions on Biomedical Engineering*, vol. 31, no. 11, pp. 725–728, 1984.

[111] Peng, C., Bai, X., Tokranova, N., Xiaojun, F., Castracane, J., and Gillis, K. D., "A novel microfabricated device measures a large fraction of hormone release from individual-cells with high time resolution," in *2nd Annual International IEEE-EMB Special Topic Conference on Microtechnologies in Medicine & Biology*, pp. 481–484, 2002.

[112] Penney, B. C., "Theory and cardiac applications of electrical-impedance measurements," *Crc Critical Reviews in Biomedical Engineering*, vol. 13, no. 3, pp. 227–281, 1986.

[113] Pethig, R. and Kell, D. B., "The passive electrical-properties of biological-systems - their significance in physiology, biophysics and biotechnology," *Physics in Medicine and Biology*, vol. 32, no. 8, pp. 933–970, 1987.

[114] Plonsey, R. and Barr, R. C., *Bioelectricity: A Quantitative Approach*. New York: Kluwer Academic / Plenum Publishers, 2nd ed., 2000.

[115] Poenie, M. and Chen, C.-S., "New fluorescent probes for cell biology," in *Optical Microscopy: Emerging Methods and Applications* (Herman, B. and Lemasters, J. J., eds.), San Diego: Academic Press, Inc., 1993.

[116] Ramadoss, R., Lee, S., Lee, Y. C., Bright, V. M., and Gupta, K. C., "Fabrication, assembly, and testing of rf mems capacitive switches using flexible printed circuit

technology," *Ieee Transactions on Advanced Packaging*, vol. 26, no. 3, pp. 248–254, 2003.

[117] Reyes, D. R., Iossifidis, D., Auroux, P. A., and Manz, A., "Micro total analysis systems. 1. introduction, theory, and technology," *Analytical Chemistry*, vol. 74, no. 12, pp. 2623–2636, 2002.

[118] Richardson, R. R., Miller, J. A., and Reichert, W. M., "Polyimides as biomaterials - preliminary biocompatibility testing," *Biomaterials*, vol. 14, no. 8, pp. 627–635, 1993.

[119] Rigaud, B., Hamzaoui, L., Frikha, M. R., Chauveau, N., and Morucci, J. P., "In-vitro tissue characterization and modeling using electrical-impedance measurements in the 100 hz-10 mhz frequency-range," *Physiological Measurement*, vol. 16, pp. A15–A28, 1995.

[120] Rigaud, B. and Morucci, J. P., "Bioelectrical impedance techniques in medicine .3. impedance imaging - first section: General concepts and hardware," *Critical Reviews in Biomedical Engineering*, vol. 24, no. 4-6, pp. 467–597, 1996.

[121] Rigaud, B., Morucci, J. P., and Chauveau, N., "Bioelectrical impedance techniques in medicine .1. bioimpedance measurement - second section: Impedance spectrometry," *Critical Reviews in Biomedical Engineering*, vol. 24, no. 4-6, pp. 257–351, 1996.

[122] Rogers, J. A., Sheppard, R. J., Grant, E. H., Bleehen, N. M., and Honess, D. J., "The dielectric-properties of normal and tumor mouse-tissue between 50 mhz and 10 ghz," *British Journal of Radiology*, vol. 56, no. 665, pp. 335–338, 1983.

[123] Rousche, P. J., Pellinen, D. S., Pivin, D. P., Williams, J. C., Vetter, R. J., and Kipke, D. R., "Flexible polyimide-based intracortical electrode arrays with bioactive capability," *Ieee Transactions on Biomedical Engineering*, vol. 48, no. 3, pp. 361–371, 2001.

[124] Sandison, M., Curtis, A. S. G., and Wilkinson, C. D. W., "Effective extracellular recording from vertebrate neurons in culture using a new type of microelectrode array," *Journal of Neuroscience Methods*, vol. 114, no. 1, pp. 63–71, 2002.

[125] Schepps, J. L. and Foster, K. R., "The uhf and microwave dielectric-properties of normal and tumor-tissues - variation in dielectric-properties with tissue water-content," *Physics in Medicine and Biology*, vol. 25, no. 6, pp. 1149–1159, 1980.

[126] Schmidt, C., Mayer, M., and Vogel, H., "A chip-based biosensor for the functional analysis of single ion channels," *Angewandte Chemie-International Edition*, vol. 39, no. 17, pp. 3137–3140, 2000.

[127] Schoning, M. J., Gluck, O., Thust, M., Ali, M., Pahlavanpour, B., Uzgirls, E. E., Gui, J. Y., and Laird, C. K., "Composition measurement," in *The Measurement, Instrumentation and Sensors Handbook* (Webster, J. G., ed.), CRC Press LLC, 1999.

[128] Schroeder, K., Neagle, B., Trezise, D. J., and Worley, J., "Ionworks (tm) ht: A new high-throughput electrophysiology measurement platform," *Journal of Biomolecular Screening*, vol. 8, no. 1, pp. 50–64, 2003.

[129] Schwan, H. P., "Dielectric properties of cells and tissues," in *Interactions Between Electromagnetic Fields and Cells* (Chiabrera, A., Nicolini, C., and Schwan, H. P., eds.), pp. 75–97, 1985.

[130] Schwan, H. P., "The practical success of impedance techniques from an historical perspective," in *Electrical Bioimpedance Methods: Applications to Medicine and Biotechnology*, vol. 873 of *Annals of the New York Academy of Sciences*, pp. 1–12, 1999.

[131] Schwan, H. P. and Foster, K. R., "Rf-field interactions with biological systems: Electrical properties and biophysical mechanisms," *Proceedings of the IEEE*, vol. 68, no. 1, pp. 104–113, 1980.

[132] Shieh, C.-C., Coghlan, M., Sullivan, J. P., and Gopalakrishnan, M., "Potassium channels: Molecular defects, diseases, and therapeutic opportunities," *Pharmacol Rev*, vol. 52, no. 4, pp. 557–594, 2000.

[133] Smith, S. R. and Foster, K. R., "Dielectric-properties of low-water-content tissues," *Physics in Medicine and Biology*, vol. 30, no. 9, pp. 965–973, 1985.

[134] Smith, S. R., Foster, K. R., and Wolf, G. L., "Dielectric-properties of vx-2 carcinoma versus normal liver-tissue," *Ieee Transactions on Biomedical Engineering*, vol. 33, no. 5, pp. 522–524, 1986.

[135] Snyder, K. V., Kriegstein, A. M., and Sachs, F., "A convenient electrode holder for glass pipettes to stabilize electrode potentials," *Pflugers Archiv-European Journal of Physiology*, vol. 438, no. 3, pp. 405–411, 1999.

[136] Stoy, R. D., Foster, K. R., and Schwan, H. P., "Dielectric-properties of mammalian-tissues from 0.1 to 100 mhz - a summary of recent data," *Physics in Medicine and Biology*, vol. 27, no. 4, pp. 501–513, 1982.

[137] Stuchly, M. A. and Stuchly, S. S., "Permittivity of mammalian-tissues invivo and invitro - advances in experimental-techniques and recent results," *International Journal of Electronics*, vol. 56, no. 4, pp. 443–456, 1984.

[138] Su, Y. C. and Lin, L. W., "A water-powered micro drug delivery system," *Journal of Microelectromechanical Systems*, vol. 13, no. 1, pp. 75–82, 2004.

[139] Surowiec, A. J., Stuchly, S. S., Barr, J. R., and Swarup, A., "Dielectric-properties of breast-carcinoma and the surrounding tissues," *Ieee Transactions on Biomedical Engineering*, vol. 35, no. 4, pp. 257–263, 1988.

[140] Suselbeck, T., Thielecke, H., Kochlin, J., Cho, S. B., Weinschenk, I., Metz, J., Borggrefe, M., and Haase, K. K., "Intravascular electric impedance spectroscopy of atherosclerotic lesions using a new impedance catheter system," *Basic Research in Cardiology*, vol. 100, no. 5, pp. 446–452, 2005.

[141] Takahashi, H., Ejiri, T., Nakao, M., Nakamura, N., Kaga, K., and Herve, T., "Microelectrode array on folding polyimide ribbon for epidural mapping of functional evoked potentials," *Ieee Transactions on Biomedical Engineering*, vol. 50, no. 4, pp. 510–516, 2003.

[142] Tanabe, M., Makinodan, J., Suzuki, K., Hosokawa, Y., Konishi, S., Ozaki, N., and Oka, H., "Development of micro channel array with detecting electrodes for electrophysiological biomedical sensor," in *The Sixteenth Annual International Conference on Micro Electro Mechanical Systems, 2003*, (Kyoto), pp. 407–410, 2003.

[143] Thinschmidt, J. S., Frazier, C. J., King, M. A., Meyer, E. M., and Papke, R. L., "Medial septal/diagonal band cells express multiple functional nicotinic receptor subtypes that are correlated with firing frequency," *Neuroscience Letters*, vol. 389, no. 3, pp. 163–168, 2005.

[144] Valentinuzzi, M. E., "Bioelectrical impedance techniques in medicine .1. bioimpedance measurement - first section: General concepts," *Critical Reviews in Biomedical Engineering*, vol. 24, no. 4-6, pp. 223–255, 1996.

[145] Valentinuzzi, M. E., Morucci, J. P., and Felice, C. J., "Bioelectrical impedance techniques in medicine .2. monitoring of physiological events by impedance," *Critical Reviews in Biomedical Engineering*, vol. 24, no. 4-6, pp. 353–466, 1996.

[146] Verpoorte, E. and De Rooij, N. F., "Microfluidics meets mems," *Proceedings of the Ieee*, vol. 91, no. 6, pp. 930–953, 2003.

[147] Wagner, J., Geddes, L. A., Foster, K., and Farag, A., "Monitoring heart and respiratory activity by impedance change using neck electrodes," *Medical & Biological Engineering & Computing*, vol. 25, no. 1, pp. 100–102, 1987.

[148] Walker, D. C., Brown, B. H., Hose, D. R., and Smallwood, R. H., "Modelling the electrical impedivity of normal and premalignant cervical tissue," *Electronics Letters*, vol. 36, no. 19, pp. 1603–1604, 2000.

[149] Xu, J., Wang, X. B., Ensign, B., Li, M., Wu, L., Guia, A., and Xu, J. Q., "Ion-channel assay technologies: quo vadis?," *Drug Discovery Today*, vol. 6, no. 24, pp. 1278–1287, 2001.

[150] Yamamoto, Y., Yamamoto, T., and Oberg, P. A., "Impedance plethysmography in human limbs .1. on electrodes and electrode geometry," *Medical & Biological Engineering & Computing*, vol. 29, no. 4, pp. 419–424, 1991.

[151] Yang, C. R., Hsieh, Y. S., Hwang, G. Y., and Lee, Y. D., "Photoablation characteristics of novel polyimides synthesized for high-aspect-ratio excimer laser liga process," *Journal of Micromechanics and Microengineering*, vol. 14, no. 4, pp. 480–489, 2004.

[152] Yi, M. Q. and Bau, H. H., "The kinematics of bend-induced mixing in microconduits," *International Journal of Heat and Fluid Flow*, vol. 24, no. 5, pp. 645–656, 2003.

[153] Yong, H., Ning, C., Borninski, J., and Rubinsky, B., "A novel microfluidic cell-chip for single cell analysis and manipulation," in *The sixteenth annual international conference on micro electro mechanical systems, 2003*, (Kyoto), pp. 403–406, 2003.

[154] Zhang, L. H., Dang, F. Q., and Baba, Y., "Microchip electrophoresis-based separation of dna," *Journal of Pharmaceutical and Biomedical Analysis*, vol. 30, no. 6, pp. 1645–1654, 2003.

[155] Zhao, T. X., "New applications of electrical impedance of human blood," *Journal of Medical Engineering & Technology*, vol. 20, no. 3, pp. 115–120, 1996.

[156] Zheng, E., Shao, S., and Webster, J. G., "Impedance of skeletal-muscle from 1 hz to 1 mhz," *Ieee Transactions on Biomedical Engineering*, vol. 31, no. 6, pp. 477–481, 1984.